

1

DarkSide-20k Technical Design Report

2

The Global Argon Dark Matter Collaboration

3

September 19, 2019

4



12

DarkSide-20k Intermediate Design Report

C. E. Aalseth,¹ S. Abdelhakim,² F. Acerbi,^{3, 4} P. Agnes,⁵ I. F. M. Albuquerque,⁶
 T. Alexander,¹ A. Alici,^{7, 8} A. K. Alton,⁹ P. Amaudruz,¹⁰ F. Ameli,¹¹ P. Antonioli,⁸
 S. Arcelli,^{7, 8} R. Ardito,^{12, 13} I. J. Arnquist,¹ P. Arpaia,^{14, 15} D. M. Asner,¹⁶ A. Asunskis,¹⁷
 M. Ave,⁶ H. O. Back,¹ A. Barrado Olmedo,¹⁸ G. Batignani,^{19, 20} M. G. Bisogni,^{19, 20} V. Bocci,¹¹
 A. Bondar,^{21, 22} G. Bonfini,²³ W. Bonivento,²⁴ B. Bottino,^{25, 26} M. G. Boulay,²⁷ R. Bunker,¹
 S. Bussino,^{28, 29} A. Buzulutskov,^{21, 22} M. Cadeddu,^{30, 24} M. Cadoni,^{30, 24} A. Caminata,²⁶
 N. Canci,^{5, 23} A. Candela,²³ C. Cantini,³¹ M. Caravati,²⁴ M. Cariello,²⁶ M. Carpinelli,^{32, 33}
 A. Castellani,^{12, 13} P. Castello,^{34, 24} S. Catalanotti,^{35, 15} V. Cataudella,^{35, 15} P. Cavalcante,^{36, 23}
 S. Cavuoti,^{35, 15} S. Cebrian,³⁷ B. Celano,¹⁵ R. Cereseto,²⁶ W. Cheng,^{38, 39} A. Chepurnov,⁴⁰
 C. Ciccalò,²⁴ L. Cifarelli,^{7, 8} M. Citterio,¹³ A. G. Cocco,¹⁵ M. Colocci,^{7, 8} L. Consiglio,⁴¹
 F. Cossio,^{38, 39} G. Covone,^{35, 15} P. Crivelli,³¹ I. D'Antone,⁸ M. D'Incecco,²³ D. D'Urso,^{32, 33}
 M. D. Da Rocha Rolo,³⁸ M. Daniel,¹⁸ S. Davini,²⁶ A. De Candia,^{35, 15} S. De Cecco,^{11, 42}
 M. De Deo,²³ A. De Falco,^{24, 30} G. De Filippis,^{35, 15} D. De Gruttola,⁴³ G. De Guido,^{44, 13}
 G. De Rosa,^{35, 15} G. Dellacasa,³⁸ P. Demontis,^{32, 33, 45} S. DePaquale,⁴³ A. V. Derbin,⁴⁶
 A. Devoto,^{30, 24} F. Di Eusanio,^{47, 23} G. Di Pietro,^{23, 13} P. Di Stefano,⁴⁸ C. Dionisi,^{11, 42}
 F. Dordei,²⁴ M. Downing,⁴⁹ F. Edalatfar,¹⁰ A. Empl,⁵ M. Fernandez Diaz,¹⁸ A. Ferri,^{3, 4}
 C. Filip,⁵⁰ G. Fiorillo,^{35, 15} K. Fomenko,⁵¹ A. Franceschi,⁵² D. Franco,⁵³ G. E. Froudakis,⁵⁴
 F. Gabriele,²³ A. Gabrieli,^{32, 33} C. Galbiati,^{47, 41} P. Garcia Abia,¹⁸ D. Gascón Fora,⁵⁵
 A. Gendotti,³¹ C. Ghiano,²³ A. Ghisi,^{12, 13} S. Giagu,^{11, 42} P. Giampa,¹⁰ R. A. Giampaolo,³⁸
 C. Giganti,⁵⁶ M. A. Giorgi,^{20, 19} G. K. Giovanetti,⁴⁷ M. L. Gligan,⁵⁰ A. Gola,^{3, 4} O. Gorchakov,⁵¹
 M. Grab,⁵⁷ R. Graciani Diaz,⁵⁵ F. Granato,⁵⁸ M. Grassi,¹⁹ J. W. Grate,¹ G. Y. Grigoriev,⁵⁹
 A. Grobov,⁵⁹ M. Gromov,⁴⁰ M. Guan,⁶⁰ M. B. B. Guerra,¹⁷ M. Guerzoni,⁸ M. Gulino,^{61, 33}
 R. K. Haaland,⁶² B. R. Hackett,⁶³ A. Hallin,⁶⁴ B. Harrop,⁴⁷ E. W. Hoppe,¹ S. Horikawa,^{41, 23}
 B. Hosseini,²⁴ F. Hubaut,⁶⁵ P. Humble,¹ E. V. Hungerford,⁵ An. Ianni,^{47, 23} V. Ippolito,¹¹
 C. Jillings,^{66, 67} S. Jimenez Cabre,¹⁸ K. Keeter,¹⁷ C. L. Kendziora,⁶⁸ S. Kim,⁵⁸ I. Kochanek,²³
 K. Kondo,⁴¹ G. Kopp,⁴⁷ D. Korablev,⁵¹ G. Korga,^{5, 23} A. Kubankin,⁶⁹ R. Kugathasan,^{38, 39}
 M. Kuss,¹⁹ M. Kuzniak,²⁷ M. La Commara,^{70, 15} M. Lai,^{30, 24} S. Langrock,^{66, 67} M. Lebois,²
 B. Lehnert,⁶⁴ X. Li,⁴⁷ Q. Liqiang,² M. Lissia,²⁴ G. U. Lodi,^{44, 13} G. Longo,^{35, 15} R. Lussana,^{71, 13}
 L. Luzzi,^{72, 13} A. A. Machado,⁷³ I. N. Machulin,^{59, 74} A. Mandarano,^{41, 23} L. Mapelli,⁴⁷
 M. Marcante,^{75, 4, 3} A. Margotti,⁸ S. M. Mari,^{28, 29} M. Mariani,^{72, 13} J. Maricic,⁶³ M. Marinelli,^{25, 26}
 D. Marras,²⁴ A. D. Martinez Rojas,^{38, 39} C. J. Martoff,⁵⁸ M. Mascia,^{76, 24} A. Masoni,²⁴
 A. Mazzi,^{3, 4} A. B. McDonald,⁴⁸ A. Messina,^{11, 42} P. D. Meyers,⁴⁷ T. Miletic,⁶³ R. Milincic,⁶³
 A. Moggi,¹⁹ S. Moioli,^{44, 13} J. Monroe,⁷⁷ M. Morrocchi,¹⁹ T. Mroz,⁵⁷ W. Mu,³¹ V. N. Muratova,⁴⁶
 S. Murphy,³¹ C. Muscas,^{34, 24} P. Musico,²⁶ R. Nania,⁸ T. Napolitano,⁵² A. Navrer Agasson,⁵⁶
 M. Nessi,⁷⁸ I. Nikulin,⁶⁹ A. O. Nozdrina,^{59, 74} N. N. Nurakhov,⁵⁹ A. Oleinik,⁶⁹ V. Oleynikov,^{21, 22}
 M. Orsini,²³ F. Ortica,^{79, 80} L. Pagani,⁸¹ M. Pallavicini,^{25, 26} S. Palmas,^{76, 24} L. Pandola,³³
 E. Pantic,⁸¹ E. Paoloni,^{19, 20} G. Paternoster,^{3, 4} V. Pavletcov,⁴⁰ F. Pazzona,^{32, 33} S. Peeters,⁸²
 P. A. Pegoraro,^{34, 24} K. Pelczar,²³ L. A. Pellegrini,^{44, 13} N. Pelliccia,^{79, 80} F. Perotti,^{12, 13}
 V. Pesudo,¹⁸ E. Picciau,^{30, 24} C. Piemonte,^{3, 4} F. Pietropaolo,⁷⁸ A. Pocar,⁴⁹ T. Pollman,⁸³
 D. Portaluppi,^{71, 13} S. S. Poudel,⁵ P. Pralavorio,⁶⁵ D. Price,⁸⁴ D. A. Pugachev,⁵⁹ B. Radics,³¹
 F. Raffaelli,¹⁹ F. Ragusa,^{85, 13} M. Razeti,²⁴ A. Razeto,²³ V. Regazzoni,^{75, 4, 3} C. Regenfus,³¹
 A. L. Renshaw,⁵ S. Rescia,¹⁶ M. Rescigno,¹¹ F. Retiere,¹⁰ Q. Riffard,⁵³ A. Rivetti,³⁸
 A. Romani,^{79, 80} L. Romero,¹⁸ N. Rossi,^{11, 23} A. Rubbia,³¹ D. Sablone,^{58, 23} P. Sala,⁷⁸
 P. Salatino,^{86, 15} O. Samoylov,⁵¹ E. Sánchez García,¹⁸ S. Sanfilippo,^{29, 28} M. Sant,^{32, 33}
 D. Santone,⁷⁷ R. Santorelli,¹⁸ C. Savarese,⁴⁷ E. Scapparone,⁸ B. Schlitzer,⁸¹ G. Scioli,^{7, 8}
 E. Segreto,⁷³ A. Seifert,¹ D. A. Semenov,⁴⁶ A. Shchagin,⁶⁹ E. Shemyakina,^{21, 22} A. Sheshukov,⁵¹
 S. Siddhanta,²⁴ M. Simeone,^{86, 15} P. N. Singh,⁵ P. Skensved,⁴⁸ M. D. Skorokhvatov,^{59, 74}

- 61 O. Smirnov,⁵¹ G. Sobrero,²⁶ A. Sokolov,^{21,22} A. Sotnikov,⁵¹ R. Stainforth,²⁷ S. Stracka,¹⁹
 62 G. B. Suffritti,^{32,33,45} S. Sulis,^{34,24} Y. Suvorov,^{35,15,59} A.M. Szlc,⁸⁴ R. Tartaglia,²³
 63 G. Testera,²⁶ T. Thorpe,^{41,23} A. Tonazzo,⁵³ A. Tosi,^{71,13} E. V. Unzhakov,⁴⁶ G. Usai,^{24,30}
 64 A. Vacca,^{76,24} E. Vázquez-Jáuregui,⁸⁷ M. Verducci,^{11,42} T. Viant,³¹ S. Viel,²⁷
 65 F. Villa,^{71,13} A. Vishneva,⁵¹ R. B. Vogelaar,³⁶ M. Wada,²⁴ J. Wahl,¹ J. J. Walding,⁷⁷
 66 H. Wang,⁸⁸ Y. Wang,⁸⁸ S. Westerdale,²⁷ R. J. Wheadon,³⁸ R. Williams,¹ J. Wilson,²
 67 Marcin Wojcik,⁵⁷ Mariusz Wojcik,⁸⁹ S. Wu,³¹ X. Xiao,⁸⁸ C. Yang,⁶⁰ Z. Ye,⁵ and G. Zuzel⁵⁷
 68
 69 ¹Pacific Northwest National Laboratory, Richland, WA 99352, USA
 70 ²Institut de Physique Nucléaire d'Orsay, 91406, Orsay, France
 71 ³Fondazione Bruno Kessler, Povo 38123, Italy
 72 ⁴Trento Institute for Fundamental Physics and Applications, Povo 38123, Italy
 73 ⁵Department of Physics, University of Houston, Houston, TX 77204, USA
 74 ⁶Instituto de Física, Universidade de São Paulo, São Paulo 05508-090, Brazil
 75 ⁷Physics Department, Università degli Studi di Bologna, Bologna 40126, Italy
 76 ⁸INFN Bologna, Bologna 40126, Italy
 77 ⁹Physics Department, Augustana University, Sioux Falls, SD 57197, USA
 78 ¹⁰TRIUMF, 4004 Wesbrook Mall, Vancouver, BC V6T 2A3, Canada
 79 ¹¹INFN Sezione di Roma, Roma 00185, Italy
 80 ¹²Civil and Environmental Engineering Department, Politecnico di Milano, Milano 20133, Italy
 81 ¹³INFN Milano, Milano 20133, Italy
 82 ¹⁴Department of Electrical Engineering and Information Technology,
 83 Università degli Studi "Federico II" di Napoli, Napoli 80125, Italy
 84 ¹⁵INFN Napoli, Napoli 80126, Italy
 85 ¹⁶Brookhaven National Laboratory, Upton, NY 11973, USA
 86 ¹⁷School of Natural Sciences, Black Hills State University, Spearfish, SD 57799, USA
 87 ¹⁸CIEMAT, Centro de Investigaciones Energéticas, Medioambientales y Tecnológicas, Madrid 28040, Spain
 88 ¹⁹INFN Pisa, Pisa 56127, Italy
 89 ²⁰Physics Department, Università degli Studi di Pisa, Pisa 56127, Italy
 90 ²¹Budker Institute of Nuclear Physics, Novosibirsk 630090, Russia
 91 ²²Novosibirsk State University, Novosibirsk 630090, Russia
 92 ²³INFN Laboratori Nazionali del Gran Sasso, Assergi (AQ) 67100, Italy
 93 ²⁴INFN Cagliari, Cagliari 09042, Italy
 94 ²⁵Physics Department, Università degli Studi di Genova, Genova 16146, Italy
 95 ²⁶INFN Genova, Genova 16146, Italy
 96 ²⁷Department of Physics, Carleton University, Ottawa, ON K1S 5B6, Canada
 97 ²⁸INFN Roma Tre, Roma 00146, Italy
 98 ²⁹Mathematics and Physics Department, Università degli Studi Roma Tre, Roma 00146, Italy
 99 ³⁰Physics Department, Università degli Studi di Cagliari, Cagliari 09042, Italy
 100 ³¹Institute for Particle Physics, ETH Zürich, Zürich 8093, Switzerland
 101 ³²Chemistry and Pharmacy Department, Università degli Studi di Sassari, Sassari 07100, Italy
 102 ³³INFN Laboratori Nazionali del Sud, Catania 95123, Italy
 103 ³⁴Department of Electrical and Electronic Engineering
 104 Engineering, Università degli Studi, Cagliari 09042, Italy
 105 ³⁵Physics Department, Università degli Studi "Federico II" di Napoli, Napoli 80126, Italy
 106 ³⁶Virginia Tech, Blacksburg, VA 24061, USA
 107 ³⁷Laboratorio de Física Nuclear y Astropartículas, Universidad de Zaragoza, Zaragoza 50009, Spain
 108 ³⁸INFN Torino, Torino 10125, Italy
 109 ³⁹Department of Electronics and Communications, Politecnico di Torino, Torino 10129, Italy
 110 ⁴⁰Skobeltsyn Institute of Nuclear Physics, Lomonosov Moscow State University, Moscow 119234, Russia
 111 ⁴¹Gran Sasso Science Institute, L'Aquila 67100, Italy
 112 ⁴²Physics Department, Sapienza Università di Roma, Roma 00185, Italy
 113 ⁴³INFN Salerno, Salerno 84084, Italy
 114 ⁴⁴Chemistry, Materials and Chemical Engineering Department
 115 "G. Natta", Politecnico di Milano, Milano 20133, Italy
 116 ⁴⁵Interuniversity Consortium for Science and Technology of Materials, Firenze 50121, Italy
 117 ⁴⁶Saint Petersburg Nuclear Physics Institute, Gatchina 188350, Russia
⁴⁷Physics Department, Princeton University, Princeton, NJ 08544, USA

- 118 ⁴⁸*Department of Physics, Engineering Physics and Astronomy,
Queen's University, Kingston, ON K7L 3N6, Canada*
 119
 120 ⁴⁹*Amherst Center for Fundamental Interactions and Physics
Department, University of Massachusetts, Amherst, MA 01003, USA*
 121
 122 ⁵⁰*National Institute for R&D of Isotopic and Molecular Technologies, Cluj-Napoca, 400293, Romania*
 123 ⁵¹*Joint Institute for Nuclear Research, Dubna 141980, Russia*
 124 ⁵²*INFN Laboratori Nazionali di Frascati, Frascati 00044, Italy*
 125 ⁵³*APC, Université Paris Diderot, CNRS/IN2P3, CEA/Irfu, Obs de Paris, USPC, Paris 75205, France*
 126 ⁵⁴*Department of Chemistry, University of Crete, P.O. Box 2208, 71003 Heraklion, Crete, Greece*
 127 ⁵⁵*Universitat de Barcelona, Barcelona E-08028, Catalonia, Spain*
 128 ⁵⁶*LPNHE, CNRS/IN2P3, Sorbonne Université, Université Paris Diderot, Paris 75252, France*
 129 ⁵⁷*M. Smoluchowski Institute of Physics, Jagiellonian University, 30-348 Krakow, Poland*
 130 ⁵⁸*Physics Department, Temple University, Philadelphia, PA 19122, USA*
 131 ⁵⁹*National Research Centre Kurchatov Institute, Moscow 123182, Russia*
 132 ⁶⁰*Institute of High Energy Physics, Beijing 100049, China*
 133 ⁶¹*Engineering and Architecture Faculty, Università di Enna Kore, Enna 94100, Italy*
 134 ⁶²*Department of Physics and Engineering, Fort Lewis College, Durango, CO 81301, USA*
 135 ⁶³*Department of Physics and Astronomy, University of Hawai'i, Honolulu, HI 96822, USA*
 136 ⁶⁴*Department of Physics, University of Alberta, Edmonton, AB T6G 2R3, Canada*
 137 ⁶⁵*Centre de Physique des Particules de Marseille, Aix
Marseille Univ, CNRS/IN2P3, CPPM, Marseille, France*
 138 ⁶⁶*Department of Physics and Astronomy, Laurentian University, Sudbury, ON P3E 2C6, Canada*
 139 ⁶⁷*SNOLAB, Lively, ON P3Y 1N2, Canada*
 140 ⁶⁸*Fermi National Accelerator Laboratory, Batavia, IL 60510, USA*
 141 ⁶⁹*Radiation Physics Laboratory, Belgorod National Research University, Belgorod 308007, Russia*
 142 ⁷⁰*Pharmacy Department, Università degli Studi "Federico II" di Napoli, Napoli 80131, Italy*
 143 ⁷¹*Electronics, Information, and Bioengineering Department, Politecnico di Milano, Milano 20133, Italy*
 144 ⁷²*Energy Department, Politecnico di Milano, Milano 20133, Italy*
 145 ⁷³*Physics Institute, Universidade Estadual de Campinas, Campinas 13083, Brazil*
 146 ⁷⁴*National Research Nuclear University MEPhI, Moscow 115409, Russia*
 147 ⁷⁵*Physics Department, Università degli Studi di Trento, Povo 38123, Italy*
 148 ⁷⁶*Department of Mechanical, Chemical, and Materials
Engineering, Università degli Studi, Cagliari 09042, Italy*
 149 ⁷⁷*Department of Physics, Royal Holloway University of London, Egham TW20 0EX, UK*
 150 ⁷⁸*CERN, European Organization for Nuclear Research 1211 Geneve 23, Switzerland, CERN*
 151 ⁷⁹*Chemistry, Biology and Biotechnology Department, Università degli Studi di Perugia, Perugia 06123, Italy*
 152 ⁸⁰*INFN Perugia, Perugia 06123, Italy*
 153 ⁸¹*Department of Physics, University of California, Davis, CA 95616, USA*
 154 ⁸²*Physics and Astronomy, University of Sussex, Brighton BN1 9QH, UK*
 155 ⁸³*Physik Department, Technische Universität München, Munich 80333, Germany*
 156 ⁸⁴*The University of Manchester, Manchester M13 9PL, United Kingdom*
 157 ⁸⁵*Physics Department, Università degli Studi di Milano, Milano 20133, Italy*
 158 ⁸⁶*Chemical, Materials, and Industrial Production Engineering Department,
Università degli Studi "Federico II" di Napoli, Napoli 80126, Italy*
 159 ⁸⁷*Instituto de Física, Universidad Nacional Autónoma de México (UNAM), México 01000, Mexico*
 160 ⁸⁸*Physics and Astronomy Department, University of California, Los Angeles, CA 90095, USA*
 161 ⁸⁹*Institute of Applied Radiation Chemistry, Lodz University of Technology, 93-590 Lodz, Poland*

CONTENTS

166	List of Figures	vi
167	List of Tables	vii
168	1. Executive Summary	1
169	2. Physics Case	1
170	2.1. DarkSide-20k: The High-Mass Search Program	3
171	2.2. DarkSide-LowMass: The Low-Mass Search Program	4
172	2.3. Argo	4
173	2.4. Comparison with Xenon-Based Experiments and the “Neutrino Floor”	5
174	2.5. Completed R&D for DS-20kProgram	6
175	2.6. Ongoing R&D for DS-20kProgram	7
176	3. Organization	7
177	3.1. Specific Roles and Responsibilities	10
178	4. Project Overview	10
179	5. Photoelectronics	14
180	5.1. PhotoDetector Modules (PDM)	14
181	5.2. Signal Transmission	15
182	5.3. PDM Fabrication and Characterization	16
183	5.4. Motherboard Assembly	17
184	5.5. Mass Production	18
185	6. Inner Detector and Cryogenics System	19
186	6.1. DS-20k LAr TPC	19
187	6.2. Cryogenics	26
188	7. Material Assays	31
189	7.1. Radio-purity database	31
190	7.2. Managing Assay Capabilities	32
191	7.3. Radioactive budget	33
192	8. Calibration	34
193	8.1. Distributed Gas Sources	34
194	8.2. Gamma Sources	35
195	8.3. Neutron Sources	35
196	8.4. Guide Tube System	36
197	9. Veto Detector	37
198	9.1. Overall Design	37
199	9.2. Assembly	39
200	9.3. Background Rejection	39
201	10. Data Acquisition	41
202	10.1. General DAQ scheme	42
203	10.2. Digitizers	42
204	10.3. DAQ software	43
205	11. Computing	43

206	11.1. Computing systems and data workflow	44
207	11.2. Software Environment	44
208	11.3. Simulation	45
209	12. The ReD Experiment	46
210	13. DarkSide-Proto	49
211	13.1. Prototype Overview and Status	49
212	13.2. The DS-Proto TPC	50
213	13.3. Materials for DarkSide-Proto	51
214	13.4. Validation tests and operation	51
215	14. AAr Cryostat	53
216	15. Argon Procurement and Purification	56
217	15.1. Urania	57
218	15.2. Aria	61
219	15.3. DArT	63
220	16. Technical Design	65
221	16.1. Installation Space and Services Needed	66
222	16.2. Electrical Power for DS-20kOperation	66
223	16.3. Nitrogen Argon and Water Services for DS-20kOperation	66
224	16.4. Underground Argon Storage and Transport	67
225	16.5. IT Infrastructure	67
226	17. Validation	67
227	18. Installation and Commissioning	67
228	18.1. Cryostat Description and Construction	68
229	18.2. Metallic Structure	69
230	18.3. Cryogenic System	69
231	18.4. The Radon Free Clean Room	69
232	18.5. TPC and Veto Detector Assembly and Installation	70
233	18.6. DS-20k Proposed Installation Sequence	70
234	19. Health, Safety and Environmental Issues	75
235	20. Radiation Protection Issues	75
236	21. Project Management	75
237	21.1. Update with respect to the attached PEP	76
238	References	76

LIST OF FIGURES

240 1	Artist rendering of the DS-20k detectors	2
241 2	Current DM limits and sensitivities for future experiments.....	4
242 3	5 σ discovery potential of the leading future noble liquid dark matter searches.....	5
243 4	The organization structure of the GADMC and of the DarkSide project	8
244 5	Artist rendering of the DS-20k experiment in Hall C of LNGS	12
245 6	The first PDM and first motherboard resulting from the assembly of PDMs.....	14
246 7	Schematic of the transimpedance amplified and summing circuits	15
247 8	Variance of impedance of SiPMs quenching resistors	16
248 9	SiPM <i>I-V</i> curves and SNR	17
249 10	SNR of the SiPMs tiles of the first motherboard	18
250 11	Artist rendering of the PMMA vessel and the TPC	20
251 12	PDM patterning scheme	22
252 13	DS-20k PDM motherboard designs	22
253 14	3D model of the full DS-20k LAr TPC reflector panels system	23
254 15	DS-20k LAr TPC anode and cathode regions	24
255 16	Simulated electric field mapping of the DS-20k LAr TPC	25
256 17	DS-20k cryogenics system P&ID	28
257 18	DS-20k condenser box	29
258 19	DS-20k materials database structure	32
259 20	Web interface of DS-20k materials database	32
260 21	Schematic of the sources insertion system	35
261 22	Pictures of the miniature $^{241}\text{AmBe}$ neutron source	36
262 23	Schematic and 3D cut-away view of the DS-20k veto detector	38
263 24	3D drawings of the DS-20k Veto detector	40
264 25	Picture of the LNS beamline in use for ReD	47
265 26	Preliminary data from the ReD experiment	49
266 27	The DS-Proto cryostat and components delivered at CERN	50
267 28	Conceptual design of the DS-Proto detector	52
268 29	Schematics of the setup for the optimization of the S2 signals	54
269 30	Details of the AAr cryostat	55
270 31	3D view of the large AAr cryostat	55
271 32	Cross-sectional view of the large AAr cryostat	56
272 33	Process Flow Diagram for the Urania UAr extraction plant	59
273 34	Screening test plant for the Urania PSA sorbent	60
274 35	Schematic view of UAr cryogenic shipping vessel	61
275 36	Block diagram of Aria	63
276 37	The Seruci-0 cryogenic distillation column	64
277 38	Details of the installation sequence (I)	72
278 39	Details of the installation sequence (II)	73
279 40	Details of the installation sequence (III)	74
280 41	Details of the installation sequence (IV)	75
281 42	Preliminary Risk Registry Table for DarkSide-20kproject(from LNGS teamplate	77
282 43	Cost Breakdown Structure for DarkSide-20kproject (from LNGS teamplate	77

LIST OF TABLES

284 I	Managerial roles of the project	11
285 II	DS-20k LAr TPC detector parameters	19
286 III	DarkSide-20k cryogenics system parameters	26
287 IV	Summary of DS-20k assays performed	33
288 V	Summary of the assay capabilities available for DS-20k	33
289 VI	Radiogenic neutrons from detector materials and background before and after cuts. .	41
290 VII	Inlet argon purity required for operation of the DarkSide-20k getter	57

291

1. EXECUTIVE SUMMARY

292 **La parte iniziale del TDR riassume le motivazioni scientifiche e/o tecnologiche che**
 293 **hanno portato alla proposta per la realizzazione del progetto in questione, un'overview**
 294 **della soluzione proposta e l'evoluzione del progetto nel tempo. Si tratta di un som-**
 295 **mario esecutivo dalla lunghezza di 1-2 pagine, che include anche una descrizione som-**
 296 **maria dei contenuti del documento.**

297 To be written....

298

2. PHYSICS CASE

299 **In questa parte viene riassunto inizialmente il lavoro svolto durante la fase di R&D**
 300 **del progetto, finanziata nella fase di CDR. Vengono descritti i risultati degli R&D ma**
 301 **anche i problemi trovati in questa fase, e le soluzioni proposte per risolverli o soluzioni**
 302 **alternative. Vengono anche elencati ulteriori R&D che si pensa di dover svolgere**
 303 **per finalizzare eventuali scelte tecniche Inoltre viene descritto il progetto nelle sue**
 304 **generalità e nel suo contesto. Vengono discusse le motivazioni scientifiche che hanno**
 305 **portato alla proposta in questione, con una chiara indicazione degli obiettivi e dei**
 306 **risultati attesi.**

307 There is strong evidence from astronomical and cosmological observations for the existence of
 308 dark matter in our Universe. Weakly Interacting Massive Particles (WIMPs) are a well-motivated
 309 dark matter candidate that may have been produced in the early Universe but are so massive and
 310 weakly interacting that they have yet to be observed in a terrestrial experiment. The observation
 311 of WIMPs with masses up to about $1 \text{ TeV}/c^2$ is a major objective of the experimental program at
 312 the High Luminosity Large Hadron Collider. Future high energy colliders like the FCC-*hh* (Future
 313 Circular Collider) will be able to extend these searches up to the $10 \text{ TeV}/c^2$ mass range [1]. Direct
 314 and indirect dark matter detection techniques allow for a search program complementary to future
 315 colliders. For example, the direct detection of dark matter via elastic scattering of galactic WIMPs
 316 from a liquid argon target is a demonstrated technique capable of probing masses well above the
 317 reach of the LHC.

318 Liquid argon (LAr) is a particularly favorable target for the detection of WIMPs thanks to its
 319 excellent event discrimination capabilities. Scintillation light initiated by particles recoiling from
 320 atomic electrons (ERs), the primary source of background in a WIMP direct detection experiment,
 321 has a time constant of approximately a microsecond. This is in stark contrast to the nanosecond
 322 time constant of scintillation light emitted during an expected WIMP-nuclear recoil event (NR).
 323 The DEAP-3600 experiment has exploited this effect via pulse shape discrimination (PSD) to
 324 achieve ER background rejection of 2.4×10^8 [2, 3]. Additional event discrimination in an argon-
 325 based detector was demonstrated by the DarkSide-50 (DS-50) experiment, which uses a two-phase
 326 time projection chamber to measure both the prompt argon scintillation light and the ionized
 327 electrons resulting from a particle interaction in the detector. This technique provides excellent
 328 position resolution and efficient detector fiducialization while maintaining PSD capabilities [4, 5].
 329 DS-50 has performed a blind analysis of their data and observed no background events over a run
 330 period in excess of two years [6]. In addition to sensitivity to WIMPs with masses above $30 \text{ GeV}/c^2$,
 331 the two-phase DS-50 detector has extended its reach to WIMP masses below $10 \text{ GeV}/c^2$ by detecting
 332 single ionization electrons extracted from the liquid argon volume [7, 8]. With careful control of ER
 333 background from local radioactivity and a reduction of the ^{39}Ar background, a 1 t LAr detector
 334 has the potential to reach the “neutrino floor” of solar neutrinos in this low-mass parameter space.

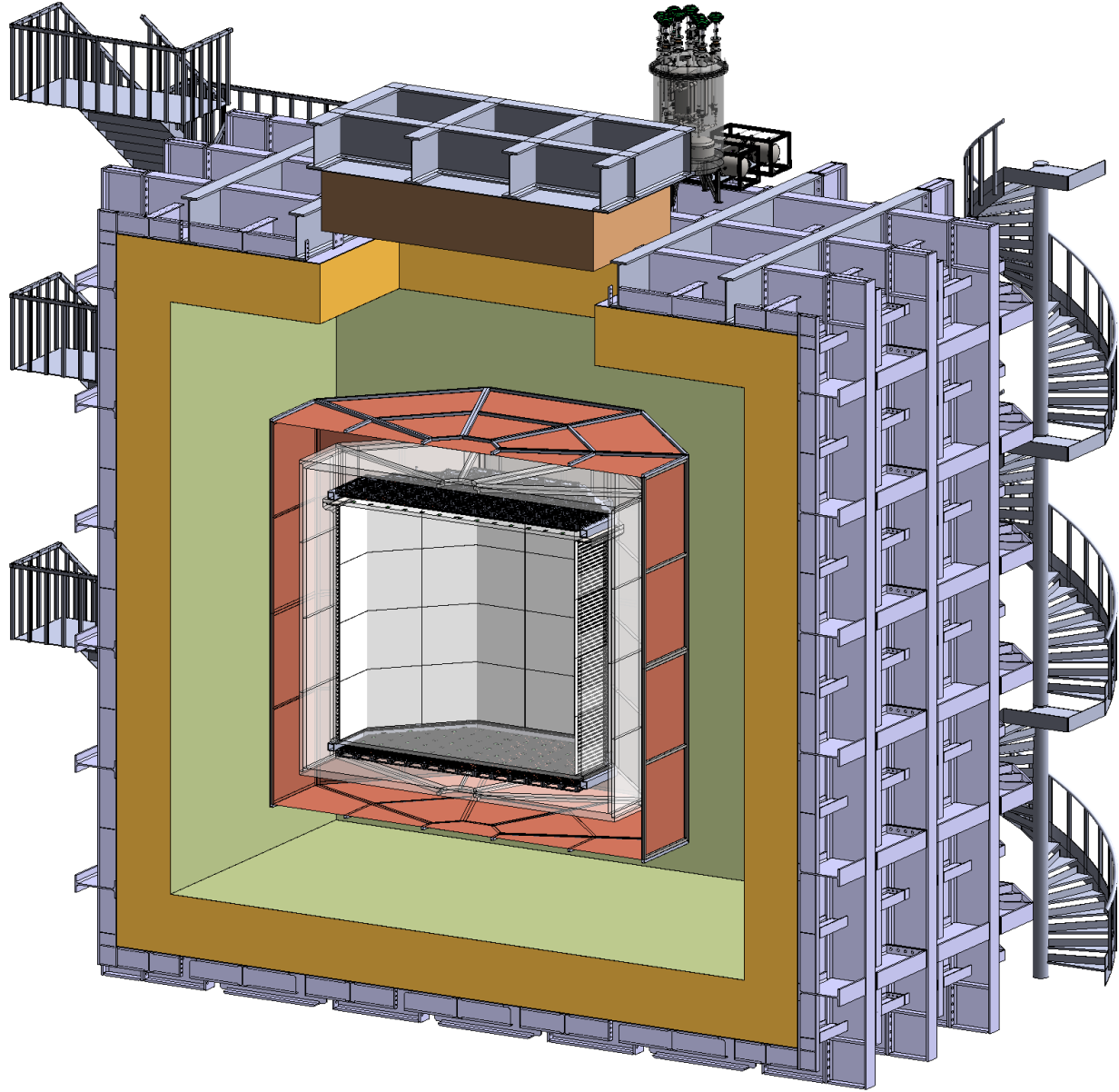


FIG. 1. Artist rendering of the DS-20k detectors, with many components omitted for clarity of presentation. The drawing shows the acrylic (PMMA) sealed TPC filled with UAr, surrounded by the veto detector consisting of a Gd-loaded acrylic Shell (GdAS) sandwiched between two atmospheric argon (AAr) active layers (the Inner Active Buffer, IAB and the Outer Active Buffer, OAB), all contained in the ProtodUNE-like cryostat. The OAB is optically separated from the rest of the AAr by a copper vessel. Technical designs of the support structure of the TPC are already available, and intentionally omitted for clarity of presentation of the main elements.

Given the potential reach of an argon-based detector, scientists from all of the major groups currently using LAr to search for dark matter, including ArDM, DS-50, DEAP-3600, and MiniCLEAN, have joined to form the Global Argon Dark Matter Collaboration (GADMC) with a goal of building a series of future experiments that maximally exploit the advantages of LAr as a detector target.

2.1. DarkSide-20k: The High-Mass Search Program

340 The immediate objective of the GADMC is construction of the DS-20k two-phase LAr detector,
 341 which will operate in Hall-C of the Gran Sasso National Laboratory (LNGS). Fig. 1 shows a 3D
 342 schematic of the DS-20k detector. DS-20k detector consists of two nested detectors housed within
 343 a ProtoDUNE-style membrane cryostat [9, 10].

344 The inner detector is a dual-phase argon time projection chamber (LAr TPC) contained within
 345 a vessel made from ultra-pure acrylic (PMMA) and filled with UAr. The central active volume of
 346 the TPC is defined by eight vertical reflector panels and the top and bottom windows of the acrylic
 347 vessel. Instead of the traditional copper field cage rings and Indium-Tin-Oxide (ITO) cathode
 348 and anode, DS-20k will use poly(3,4-ethylenedioxothiophene) polystyrene sulfonate (also known
 349 as PEDOT:PSS and commercialized under the name CleviosTM [11]). All the TPC surfaces in
 350 contact with the active argon volume will be coated with wavelength shifter tetraphenylbutadiene
 351 (TPB) to convert LAr scintillation light to a wavelength detectable by SiPMs. 8280 SiPM-based
 352 PhotoDetector Modules (PDM) arrays will view the argon volume through the top and bottom
 353 windows of the acrylic vessel. The height of the TPC is 350 cm. The total mass of LAr in the
 354 active volume is 49.7 t.

355 The outer veto detector is made of a passive Gd-loaded PMMA shell surrounding the inner
 356 detector and between two active AAr layers. The Gd-loaded PMMA shell moderates
 357 neutrons emitted from the LAr TPC until they capture on Gd, resulting in the emission of multiple
 358 γ -rays. The γ -rays interact in the AAr layers and cause scintillation light that is detected by
 359 photodetectors, thereby providing an efficient veto of radiogenic neutrons that could result in a
 360 NR in the TPC. The ProtoDUNE-like cryostat will be surrounded by layers of plastic to moderate
 361 cosmogenic and radiogenic neutrons from the rocks surrounding Hall C.

362 The DS-20k detector will have ultra-low backgrounds and the ability to measure its backgrounds
 363 *in situ*, resulting in an expected sensitivity to WIMP-nucleon cross sections of $1.2 \times 10^{-47} \text{ cm}^2$
 364 ($1.1 \times 10^{-46} \text{ cm}^2$) for $1 \text{ TeV}/c^2$ ($10 \text{ TeV}/c^2$) WIMPs following a five years run. This projected
 365 sensitivity is a factor of >50 better than currently-published results above $1 \text{ TeV}/c^2$ and covers a
 366 large fraction of the parameter space currently preferred by supersymmetric models.

367 The sensitivity would further improve to $7.4 \times 10^{-48} \text{ cm}^2$ ($6.9 \times 10^{-47} \text{ cm}^2$) for $1 \text{ TeV}/c^2$ ($10 \text{ TeV}/c^2$)
 368 WIMPs for a ten years run with a 200 t yr exposure, see Fig. 2. During the 200 t yr exposure, 3.2
 369 NRs events are expected from the coherent scattering of atmospheric neutrinos, making DS-20k the
 370 first ever direct dark matter detection experiment to reach this milestone. The DS-20k experiment
 371 is foreseen to begin operating in 2022 and will either detect WIMP dark matter or exclude a large
 372 fraction of favored WIMP parameter space.

373 DS-20k is designed to operate with zero backgrounds, meaning that all sources of instrumental
 374 background are reduced to <0.1 events over a 200 t yr exposure. All background from minimum-
 375 ionizing radiation sources will be completely removed thanks to the combined action of PSD of the
 376 primary scintillation pulse and comparison of the primary and secondary scintillation (see Sec. 2.2.4
 377 for details on the suppression of background from pp scatters on electrons and Ref. [24] for that
 378 from ^{222}Rn , ^{220}Rn , and progenies). Table VI shows the expected radiogenic neutron background
 379 contributions of the various detector components following all TPC and veto cuts for the full DS-20k
 380 exposure. The only remaining background for WIMP searches will be the signal from the coherent
 381 scattering of atmospheric neutrinos on argon nuclei, with an expected 3.2 events over the 200 t yr
 382 exposure. DS-20k will thus be the first experiment in a position to detect this important signal.

383 This outstanding sensitivity to coherent nuclear recoils will enables DS-20k to detect a supernova
 384 neutrino burst coming from anywhere in the Milky Way Galaxy and, for a majority of the galaxy,
 385 clearly identify the neutronization burst. DS-20k would perform a flavor-blind measurement of
 386 the total neutrino flux and average energy, setting an overall normalization that is not affected
 387 by neutrino oscillations. When combined with a flavor-specific measurement from a detector like
 388 Super-Kamiokande or DUNE, this observation could have sensitivity to the neutrino mass hierarchy.

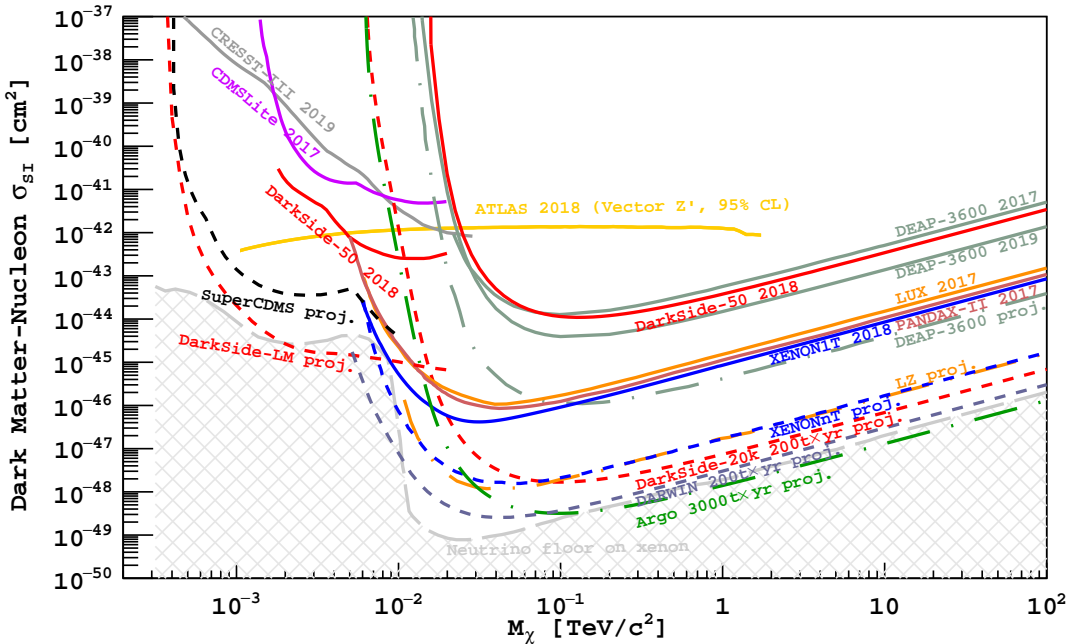


FIG. 2. 90 % C.L. exclusion limits showing leading results from direct (continuous lines, Ref. [6, 7, 12–15]) and accelerator-based dark matter searches (region above the yellow line [16]) compared with sensitivities of future germanium-, xenon-, and argon-based direct searches (dashed lines, Ref. [17–21] and this work). The “neutrino floor” curve follows the definition of Ref. [22]. The 95% C.L. limit from the ATLAS Experiment is shown for a benchmark model in which Dirac-fermion WIMPs interact with ordinary matter via a vector mediator with coupling strengths to quarks, leptons and WIMPs of 0.25, 0.01, and 1, respectively [23].

389

2.2. DarkSide-LowMass: The Low-Mass Search Program

390

In parallel to DS-20k detector, the GADMC will pursue the development of an approximately 391 1 t detector specifically optimized for the detection of low-mass dark matter, DarkSide-LowMass 392 (DS-LM). DS-LM will achieve a lower energy threshold than DS-20k by triggering on the electro- 393 luminescence signal from ionization electrons, thereby adding sensitivity to WIMP masses below 394 10 GeV/ c^2 at the expense of the PSD power afforded by argon prompt scintillation light. Without 395 PSD, contributors to the ER background in DS-LM must be reduced beyond the requirements of 396 DS-20k through careful detector design and material selection. While the DS-LM experiment is 397 outside the scope of this proposal, the implementation of DarkSide-20k project will have direct 398 impacts on the technological advancements required to enable DS-LM and the goal of reaching the 399 neutrino floor for WIMP masses between 1 GeV/ c^2 and 10 GeV/ c^2 , see Fig. 2. Among these are the 400 development of low-background PDMs [25, 26] and the construction of the Aria cryogenic distilla- 401 tion column, which will completely remove ^{85}Kr and reduce ^{39}Ar levels to the level of 1 $\mu\text{Bq}/\text{kg}$. 402 The development of DS-LM may exploit components of the DS-Proto detector under development 403 at CERN. Funding for the development, construction, commissioning, and operation of DS-LM 404 will be separately requested via alternative funding programs.

405

2.3. Argo

406

The ultimate objective of the GADMC is the construction of the Argo detector, which will have 407 a 300 t fiducial mass and will push the experimental sensitivity to the point at which the coherent 408 scattering of atmospheric neutrinos becomes a limiting background. The excellent ER rejection

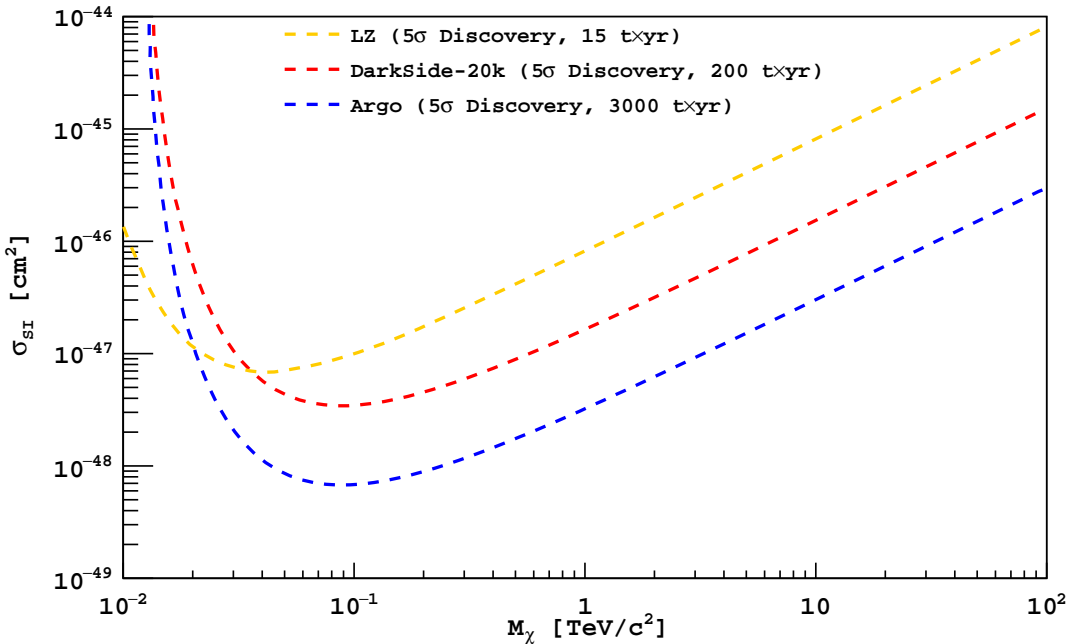


FIG. 3. 5σ discovery potential of the leading future noble liquid dark matter searches.

possible in argon will eliminate backgrounds from solar neutrinos, which will extend the sensitivity of Argo beyond that of technologies with more limited ER discrimination. The throughput of the Urania plant and Aria facility will enable 400 t of UAr to be extracted and purified over a period of about 6 yr. In addition to dark matter detection, such a large detector would also have excellent sensitivity to a neutrino burst associated with a galactic supernova. If located at SNOLAB or at similar depth, Argo will also have the potential to observe CNO neutrinos for the first time and solve the Solar Metallicity Problem [27]. While the construction of Argo is not within the scope of this proposal, the implementation of DarkSide-20k project will pave the way for the development of Argo towards the end of the next decade.

Combined DS-20k, DS-LM, and Argo, will completely cover the spin-independent WIMP hypothesis parameter space down to the neutrino floor for WIMP masses from $1 \text{ GeV}/c^2$ to several hundreds of TeV/c^2 .

2.4. Comparison with Xenon-Based Experiments and the “Neutrino Floor”

Next generation dark matter experiments will be sensitive to several sources of neutrinos via $\nu - e$ elastic scattering and coherent elastic neutrino scattering (CE ν NS) on nuclei (NR). Atmospheric and diffuse supernovae neutrinos, which due to their high energies can produce NRs in excess of $20 \text{ keV}_{\text{nr}}$, will be the dominant CE ν NS background contributor for WIMP masses above $30 \text{ GeV}/c^2$. Solar neutrinos are the main CE ν NS background for dark matter masses below $10 \text{ GeV}/c^2$. With argon’s ability to discriminate ER from NR to better than a part in 2.4×10^8 , CE ν NS represents the only irreducible background for a large exposure argon dark matter search. The neutrino background is exacerbated in liquid xenon detectors, which, due to their limited ER rejection power, accept a non-negligible number of $\nu - e$ elastic scatters as signal.

When calculating the discovery sensitivity of a large dark matter search experiment, one must fully account for the presence of neutrino-induced backgrounds. We note that the position of the “neutrino floor”, initially conceived as indicative of the maximum sensitivity attainable by an ex-

periment in the presence of CE ν NS background, is critically dependent on the target, experimental technique, statistical analysis, neutrino flux uncertainty and theoretical cross section uncertainty. We therefore include a detailed accounting of the CE ν NS and $\nu - e$ backgrounds in the sensitivity and discovery potential curves shown in Fig. 2 and Fig. 3. We conservatively estimate a 20 % uncertainty on the neutrino background for high-mass ($30 \text{ GeV}/c^2$) searches with Argo. This accounts for a 15 % uncertainty on the atmospheric neutrino flux at mid-latitude locations, such as SNOLAB or LNGS, based on the latest data-driven models of cosmic primaries [28] as well as models of solar cycle, seasonal, geographic, and geomagnetic dependence of the neutrino flux [29, 30]. Additionally, we account for a 5 % theoretical uncertainty on the Standard Model interaction cross-section, driven by uncertainties on the nuclear form factor and the expected constraints that the COHERENT collaboration will place on non-Standard Model contributions using a LAr target [31], which in turn is driven by their current 10 % uncertainty on neutrino flux [32] and a 6 % uncertainty on the LAr response as measured by SCENE [33, 34] and ARIS [35]. Planned improvements of COHERENT, including a sharper characterization of the neutrino flux and a measurement with a LAr target, would further reduce the uncertainty on the neutrino background below 10 %, strongly benefiting the DS-20k, and Argo experiments.

Within this framework, we calculate the 5σ discovery potential for DS-20k and Argo and compare it with that of the near-future LXe experiment LZ [36]. As seen from Fig. 3, DS-20k has significantly greater discovery potential than that of LZ.

2.5. Completed R&D for DS-20k Program

The following technologies are key to the success of DarkSide-20k project and the long term scientific goals of the GADMC. Their development will also have potentially wide-reaching effects within the physics community.

Low-Radioactivity Underground Argon with Urania [24]: The DS-50 experiment established that UAr is depleted of ^{39}Ar by a factor of approximately 1400, a sufficiently low rate to be deployed in a detector the size of DS-20k. However, constructing DS-20k will require that large amounts of UAr be procured in a timely fashion. This will be accomplished by Urania, an argon extraction and purification plant capable of extracting 250 kg/d of UAr. The Urania plant is fully funded by the INFN and will be built by a contracted vendor following specifications established by the Urania Project team. The tender process for the plant's final design, construction, and shipment to the installation site in Cortez, Colorado, is underway and will conclude by the end of July 2019 with the selection of a contractor. The preparation of the extraction site, as well as the installation and commissioning of the plant, falls under the responsibility of the U.S. NSF-supported groups. The Urania UAr extraction plant is projected to collect approximately 60 t of argon for use in DS-20k detector by 2022 and could continue to produce underground argon for Argo and other interested particle physics experiments that require UAr to achieve their scientific objectives.

Purification and Active Depletion with Aria [24]: The Aria plant is a 350 m tall cryogenic distillation column that was designed to explore the possibility of chemically separating argon isotopes. The construction of Aria is fully supported by INFN and Regione Autonoma della Sardegna.

SiPM-based Cryogenic Photosensors [24–26]: The development of low-background, large-area, cryogenic silicon photomultiplier (SiPM) detectors capable of replacing conventional photomultiplier tubes is critically important for achieving the desired sensitivity of DS-20k and other large-scale LAr-based experiments, including DUNE, and LXe-based detectors, such as nEXO [37] and NEXT [38–40]. The DS-20k photodetector modules will be assembled at the Nuova Officina Assergi (NOA), a dedicated cleanroom packaging facility that will have future utility for any experiment needing large volume silicon detector production.

ProtoDUNE Liquid Argon Cryostat [9, 10]: DS-20k detector will operate within a membrane cryostat filled with liquefied atmospheric argon, a technology initially developed at CERN for ProtoDUNE. Eliminating the organic liquid scintillator veto used in DS-50 for the AAr veto

484 has several advantages. With the the DS-20k LAr TPC directly immersed in AAr, the massive
485 stainless steel vacuum cryostat necessary for DS-50, and its correspondingly large contribution of
486 background events, can be replaced with a transparent, radio-pure PMMA vessel. Photodetector
487 modules can then be mounted outside of the PMMA vessel, reducing their contribution to the
488 background rate and simplifying their assembly strategy. The ProtoDUNE cryostat has the added
489 advantage that it is scalable, making it a technology appropriate for Argo.

490 **Sealed PMMA TPC** [2, 41, 42]: The DEAP-3600 collaboration has extensive experience
491 developing large, radio-pure sealed PMMA vessels. This technology will be used to build the vessel
492 for the DS-20k LAr TPC, eliminating the need for some of the most problematic radiogenic neutron
493 contributors in DS-50, most notably the stainless steel cryostat. The PMMA vessel will also reduce
494 the complexity of the TPC assembly.

495 2.6. Ongoing R&D for DS-20kProgram

496 All the major technologies needed for the design and construction are proven and do not neces-
497 sitate further R&D by the collaboration as discussed in the preceding paragraph. Some limited
498 developments are only needed in order to finalize the mass production for SiPM and the production
499 of the Gd loaded acrylic panels for the construction of the neutron veto. In both cases the R&D is
500 actively on-going and will be finalized by 2020.

501 3. ORGANIZATION

502 Definire la struttura organizzativa dell'esperimento:

- 503 • Spokesperson,
- 504 • Technical Coordinator,
- 505 • Local Responsible,
- 506 • Site Manager,
- 507 • Funds Responsible,
- 508 • GLIMO-S&E.

509 The organization structure of the GADMC and of the DarkSide project is defined in Fig. 4. The
510 governance of the GADMC is carried out by two distinct branches: the policy-making branch and
511 the executive branch.

512 The organization structure of the DarkSide project is defined in Fig. 4. The governance is carried
513 out by two distinct branches: the policy-making branch and the executive branch.

514 Policy-making is done by the **Institutional Board (IB)**. Each institution is represented within
515 the IB by its PI. The IB is guided by an elected **IB Chair** with a renewable 2 year mandate. The
516 IB is responsible for the definition of rules and the governance of the Collaboration, the overall
517 organization of the Collaboration, the appointment of all managers belonging to the policy-making
518 and executive branches; the final approval of major design changes proposed by the executive
519 branch; and the control of financial and human resources. The current IB Chair is G. Batignani
520 (Pisa), elected in November 2016 and re-confirmed in November 2018.

521 Within the policy-making branch there are three committees charged with providing recommen-
522 dations to the IB and its Chair. The members of the three committees are appointed by the IB
523 upon proposal of the IB Chair, taking into account the composition of the Collaboration and the
524 need to represent its diverse composition. These three committees are:

525 **The Advisory Board**, consisting of the IB Chair and 6 senior IB members nominated by the
526 IB Chair, of which 2 members are from Italian institutions, 1 member is from a US institution,
527 1 member is from a Canadian institution, and 2 members are from institutions outside the

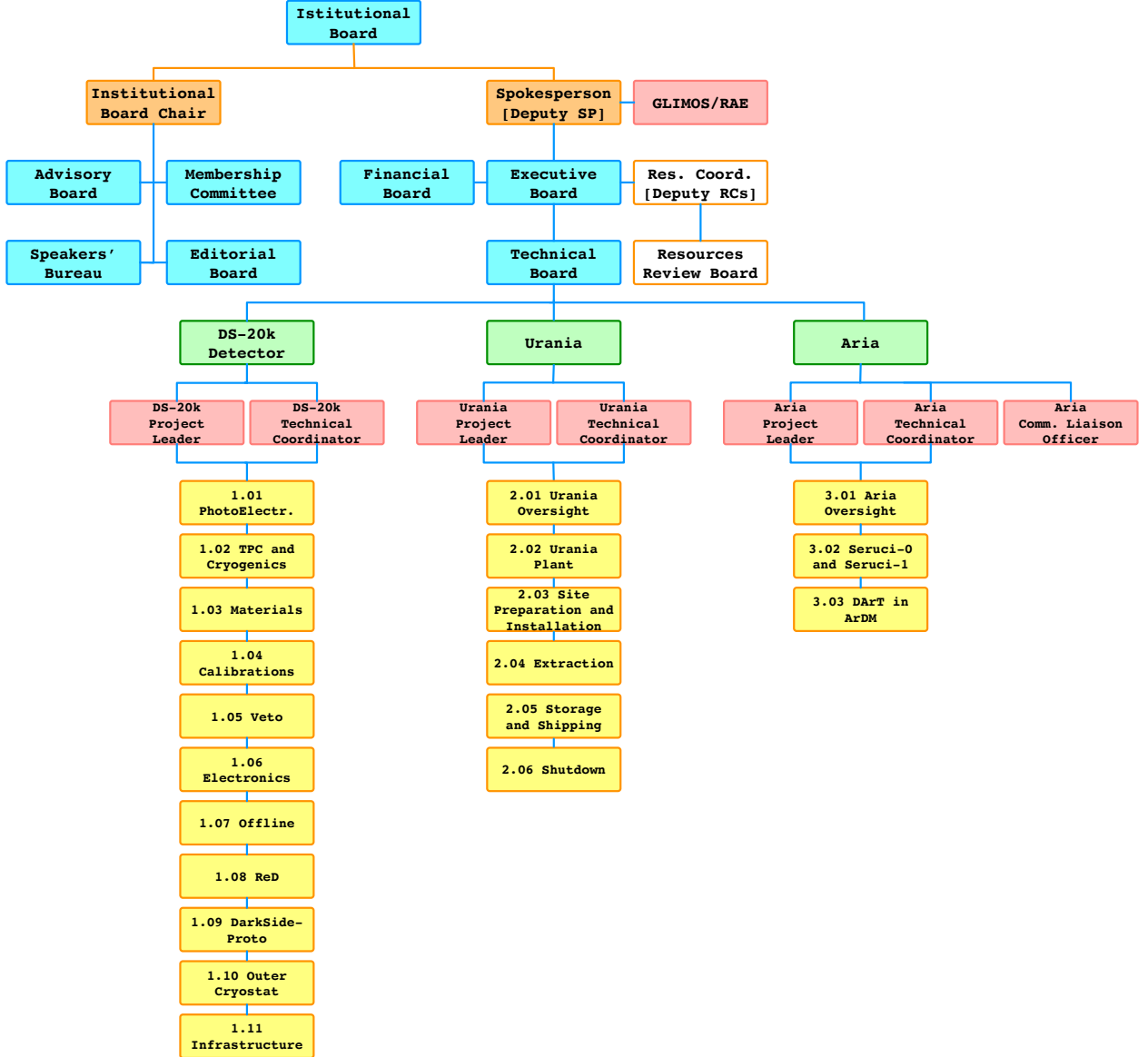


FIG. 4. The organization structure of the GADMC and of the DarkSide project.

528 three countries already listed. This committee is mandated with advising the IB Chair on IB
 529 management issues.

530 **The Membership Committee**, consisting of 6 members nominated by the Advisory Board and
 531 confirmed by the IB, as well as 2 *ex officio* Advisory Board members. This committee addresses
 532 requests from new groups wishing to join the Collaboration, helps define the commitments of
 533 new groups, and maintains the database and mailing lists of the collaboration.

534 There are two additional committees within the policy-making branch charged with providing
 535 recommendations to the IB on the communication of scientific and technological results. The
 536 members of the two committees are appointed by the IB upon proposal of the IB Chair, taking into
 537 account the composition of the Collaboration and the need to represent its diverse composition.
 538 The two committees are:

539 **The Speakers' Bureau**, consisting of 5 members nominated by the Advisory Board and con-
 540 firmed by the IB, 1 *ex officio* Advisory Board member, and the SP and Deputy SP. This commit-
 541 tee appoints speakers at conferences and workshops and approves material that will be presented
 542 on behalf of the Collaboration.

543 **The Editorial Board**, consisting of 6 members nominated by the Advisory Board and confirmed
544 by the IB. This committee approves the start of paper preparation, guides the internal paper
545 review process, and issues final approval of papers before publication.

546 The executive branch of the GADMC is led by an elected **Spokesperson (SP)**. The primary
547 responsibility of the SP is to oversee the DS-20k experiment, oversee any other scientific efforts
548 pursued by the Collaboration, and act as the Collaboration's primary public face. The SP is
549 assisted by an elected **Deputy SP (dSP)**. The mandates of the SP and dSP are 3 years, renewable.
550 C. Galbiati and G. Fiorillo were elected as SP and Deputy SP respectively in December 2016.

551 The DarkSide-20k project is organized into 3 sub-projects: **the DS-20k detector, Urania**,
552 and **Aria**. Each of the sub-projects is managed by two **Project Coordinators (PCs)**, *i.e.*,
553 a **Project Leader (PL)** and a **Technical Coordinator (TC)**. The PL manages the overall
554 progress of the sub-project and is responsible for and coordinates the **Level-1 (L1) Work Groups**
555 (**WGs**) in which the sub-project tasks and objectives are subdivided and organized, ensuring
556 that the design and construction of the sub-project is carried out on schedule, within the cost
557 ceiling, and in a way that meets the performance and reliability requirements determined within
558 the framework of GADMC resource planning. The PL plans the schedule and budget, sets deadlines,
559 and monitors quality and progress of the sub-project under their oversight. The TC is responsible
560 for the sub-project construction and the technical integration of all its components. The TC ensures
561 the implementation of engineering standards and procedures, monitors the overall construction of
562 detectors and infrastructure, and is responsible for the sub-project's integration and safety. The
563 Aria sub-project, due to its complex nature, has an additional PC, a **Community Liaison Officer**
564 charged to act as a link with the local authorities in Sardinia.

565 In addition to the PCs defined above, three **Project Scientists (PSs)** are charged with the
566 scientific oversight of the detector design and construction to ensure that all technical decisions are
567 fully compliant with the requirements of the project and compatible across all sub-systems.

568 The management of each sub-project is divided between **Level-1 (L1) Managers** and **Level-
569 2 (L2) Managers**, who are responsible for the direction of the **L1** and **L2 WGs** in which the
570 sub-project are organized and structured.

571 The **Executive Board (EB)**, which is chaired by the SP and includes as members the dSP, the
572 PSs, all PCs, and all L1 Managers, manages the executive branch of the GADMC. The IB Chair
573 is an *ex officio* member of the EB. The SP regularly invites senior PIs charged with significant
574 organization and funding responsibilities but without a formal PC role to the EB meetings.

575 The PSs and the PCs of DS-20k and Urania report to the EB. The PCs of Aria report to the
576 **Scientific Responsible (SR) of Aria**, which is jointly appointed by INFN and the Regione
577 Autonoma della Sardegna. The SR of Aria is C. Galbiati, the inventor and founder of the Aria
578 program. The SR of Aria reports to the EB.

579 All PCs and PSs are nominated by the SP to the EB, proposed by the EB to the IB, and
580 appointed by the IB. PCs are required to pledge that DS-20k will be their top scientific priority
581 and that they will dedicate a dominant fraction of their research time to their effort within the
582 GADMC. The EB and by the IB monitor closely the effectiveness of the PCs.

583 The L1 Managers are proposed by the PCs, confirmed by the EB, and appointed by the IB.
584 The L1 Managers report to the PCs. The L2 Managers are proposed by the L1 coordinators in
585 concurrence with the PCs, confirmed by the EB, and appointed by the IB. The L2 Managers report
586 to the L1 Managers.

587 The **Technical Board (TB)**, chaired by the SP and with a membership of the dSP, the PSs,
588 all PCs, and all L1 and L2 Managers, is responsible for the execution of the project. The IB Chair
589 is an *ex officio* member of the TB. All TB meetings and calls are open to the entire Collaboration.
590 The TB is the forum where all major and minor decisions affecting the project are debated and
591 finalized. In its decision making process, the TB typically operates by building consensus. The TB
592 also monitors the execution of the individual sub-projects and discusses matters at the interface
593 between different sub-projects. All TB meetings are prepared and chaired by the DS-20k TC.

594 The DarkSide resource coordination is delegated to a **Resources Coordinator (RC)**, who has
595 responsibility for the administration of the common fund. The RC is appointed by the IB upon

596 proposal of the EB.

597 The **Resources Review Board (RRB)** is made up of representatives from the funding agencies
598 providing major contributions to the project, the IB Chair, the SP, the dSP, the RC, and the
599 **Country Representatives (CRs)**, who are appointed by the assembly of PIs supported by any
600 given funding agency and is in charge of the relationship with said agency. The RRB responsibilities
601 include the monitoring and management of the financial instruments that constitute the GADMC
602 resources, defining the national and regional contributions to the project, developing the MoU, and
603 approving in-kind contributions. The **Financial Board (FB)** is composed of the **CRs** and advises
604 the SP on the specific allocation of tasks and funding requests.

605 A requirement of the LNGS Safety Management System is the appointment of a collaborator as a
606 **Group Leader in Matters of Safety (GLIMOS)**. The GLIMOS has the primary responsibility
607 for health and safety within the Collaboration, providing an interface with LNGS. The GLIMOS
608 is appointed by the LNGS Director upon recommendation by the Collaboration. An additional
609 requirement of the LNGS Environmental Management System is the appointment of a collabora-
610 tor as contact person for environmental issues or **Referente Ambientale dell'Esperimento**
611 (**RAE**). The RAE acts as the link between the experimental collaboration and LNGS for all mat-
612 ters concerning environmental protection. The RAE is appointed by the LNGS Director upon
613 recommendation by the Collaboration management

614 3.1. Specific Roles and Responsibilities

615 Table I offers a brief summary of the most significant executive responsibilities within the 3
616 sub-projects.

617 4. PROJECT OVERVIEW

618 **Sulla base del disegno concettuale e dei risultati della fase di ricerca e sviluppo**
619 **identificati nel paragrafo 2 del CDR si illustra la configurazione finale dell'apparato**
620 **proposto. Le caratteristiche dell'esperimento, quelle dei sistemi e dei sottosistemi**
621 **principali devono essere descritte e riassunte tramite tavole e schema del PBS (Product**
622 **Breakdown Structure), un esempio mostrato in figura 1. Vengono altresì mostrati i**
623 **requisiti del progetto nella presente configurazione.**

624 Many fundamental design parameters for the DarkSide-20k (DS-20k) experiment are based on
625 the successful experience of the DarkSide Collaboration in constructing, commissioning, and oper-
626 ating the DarkSide-50 (DS-50) detector in a background-free mode. The many technical details of
627 DarkSide-50 can be found in [4–8, 35, 43–50]. The DS-20k liquid argon time projection chamber
628 (LAr TPC) will, too, be deployed at LNGS in the underground Hall C, at the center of a newly
629 constructed active veto system. Fig. 5 shows the rendering of the future installation of DS-20k in
630 the underground Hall C of LNGS and Fig. 1 shows an overview of the detailed arrangement of the
631 LAr TPC and its anti-coincidence veto detector. The DS-20k experiment is designed to operate for
632 a minimum of 10 yr while maintaining an irreducible background level in the WIMP search region
633 of less than <0.1 events for the total exposure. To achieve this goal, the design parameters of the
634 DS-20k experiment have been taken directly from DS-50, where possible. Design changes have been
635 made where needed in order to accommodate for the much larger size of DS-20k and to allow the
636 experimental design to be scalable to a detector at the multi-hundred tonne scale. In building this
637 preliminary design, issues that have arisen because of design choices or materials selections have
638 been dealt with by limited design modifications, and further optimization will continue as the final
639 development work is completed and a full technical design is made.

Project Scientists		P. Meyers W. Bonivento A. Razeto	Princeton INFN Cagliari INFN LNGS
DS-20k Project Coordinators	Project Leader Technical Coordinator	E. Scapparone An. Ianni	INFN Bologna Princeton
	DarkSide-Proto Managers	G. Fiorillo	INFN Napoli
	Technical Integration Manager	T. Napolitano	INFN LNF
	Materials Manager	R. Santorelli	CIEMAT
	ArDM Manager	C. Regenfus	ETH Zürich
	Inner Detector Manager	H. Wang	UCLA
	Deputy Inner Detector Manager	E. Pantic	UC Davis
	Outer Detector Manager	G. Testera	INFN Genova
DS-20k L1 Managers	Deputy Outer Detector Manager	J. Monroe	RHUL
	PhotoElectronics Manager	A. Razeto	INFN LNGS
	Electronics Manager	M. Rescigno	INFN Roma 1
	Calibration Manager	J. Maricic	Hawai'i
	Offline Manager	D. Franco	CNRS/IN2P3
	ReD Manager	L. Pandola	INFN LNS
	Outer Cryostat Manager	M. Nessi	CERN
Urania Project Coordinators	Project Leader Technical Coordinator	M. Simeone A. Renshaw	INFN Napoli University of Houston
Urania L1 Managers	Plant Manager Site Preparation and Installation Extraction	M. Simeone A. Renshaw H. Back	INFN Napoli Houston PNNL
Aria Project Coordinators	Project Leader Deputy Project Leader Technical Coordinator Deputy Technical Coordinator Community Liason Officer	W. Bonivento F. Gabriele R. Tartaglia M. Razeti A. Devoto	INFN Cagliari INFN LNGS INFN LNGS INFN Cagliari INFN Cagliari
Aria L1 Managers	Seruci-I Manager DArT Manager	F. Gabriele W. Bonivento	INFN LNGS INFN Cagliari

TABLE I. Overview of the most significant managerial roles within the DarkSide sub-projects.

640 DS-20k will be built by the Global Argon Dark Matter Collaboration (GADMC) and will consist
 641 of two detectors: the inner detector and the veto detector, both hosted in a ProtoDUNE-like
 642 cryostat [9, 10]. The inner detector is a LAr TPC filled with underground argon (UAr). The veto
 643 detector is made of a plastic shell, loaded with Gd, surrounding the inner detector, sandwiched
 644 between two active atmospheric argon (AAr) layers.

645 The decision to abandon an organic liquid scintillator veto and to host DS-20k within a
 646 ProtoDUNE-like cryostat was originally motivated by the need of minimizing the environmental
 647 impact on underground LNGS operations, but carries significant performance advantages.
 648 Indeed, operating the TPC directly in the ProtoDUNE-like cryostat eliminates the need of a cryo-
 649 stat in the immediate proximity of the UAr target, which would significantly contribute to the
 650 residual background. We therefore adopted a new design, with the UAr-filled TPC immersed in a
 651 bath of liquefied AAr held at the same temperature and pressure. This then allows for the use of
 652 a TPC vessel fabricated from the same ultra-pure poly(methyl methacrylate) (acrylic or PMMA)
 653 developed for the DEAP-3600 experiment, and thus eliminating the need for a dedicated cryostat
 654 or UAr containment vessel. The outer walls of the TPC will sit approximately 2 m away from inner
 655 wall of the cryostat. The ProtoDUNE-like cryostat may be surrounded by layers of plastic for
 656 moderation of cosmogenic and radiogenic neutrons from the rocks surrounding the LNGS Hall C,
 657 this option is being investigated.

658 While this overview section gives a general outline of the project and introduces the major
 659 features of the experiment as they stand in the current preliminary design, the real details are
 660 given in the subsequent sections. The development of the SiPM photosensors, the LAr TPC and
 661 its cryogenics and gas handling system, and the materials screening plan that will ensure the radio

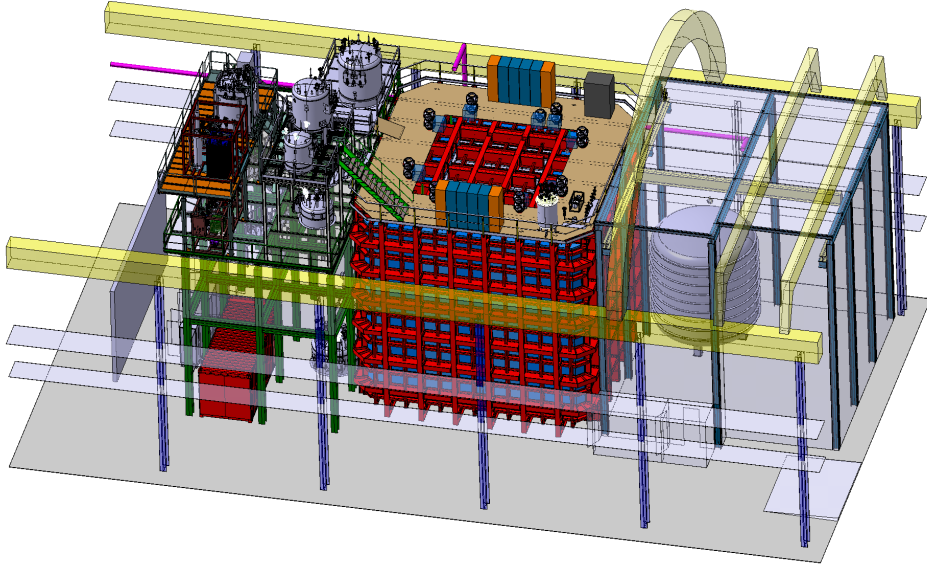


FIG. 5. Artist rendering of the DS-20k experiment in Hall C of LNGS.

purity of the experiment, are detailed in Sec. 5, Sec. 6 and Sec. 7, respectively. The plan for the calibration of the experiment is given in Sec. 8, the design of the veto detector is presented in Sec. 9, and the details about the data acquisition system and the plan for offline computing are given in Sec. 10 and Sec. 11, respectively. The two ancillary detectors, ReD and DarkSide-Proto, are described in Sec. 12 and Sec. 13. Finally, the design and use of the atmospheric argon cryostat, modeled after the ones deployed for ProtoDUNE, are given in Sec. 14, while the procurement of the underground argon (UAr) target is detailed in the final section, Sec. 15. Note that the following forms a preliminary design for an experiment capable of the stated physics goals, but may change as the technical details evolve in the final engineering stages. DS-20k will be built to operate for a minimum of 10 yr, providing the best sensitivity to high-mass WIMP dark matter.

Energy deposits in the LAr target result in the production of excited and ionized argon atoms, according to the underlying process for recoiling electrons or nuclei. Excited argon atoms, which can also be produced by recombining ionization charge, lead to an efficient formation of argon excimers decaying via the emission of scintillation light characterized by two decay time constants. Both of the components are combine to yield an instant light signal, called S1. Due to the deep UV nature (around 128 nm) of this scintillation light, which is absorbed by most materials, a thin layer of wavelength shifter, tetraphenyl butadiene (TPB), must cover all exposed surfaces to convert the photons to those of optical wavelengths for detection by photosensors. Ionization electrons escaping recombination are drifted to the top of the LAr by an applied electric field, where an electric field stronger than the field applied to drift the electrons, extracts the electrons into the gas pocket above the liquid. Here the strong field accelerates the electrons, enough for them to excite (but not ionize) the argon gas, producing a secondary scintillation signal S2, proportional to the ionization charge. Photosensors placed behind the wavelength shifter-coated windows at the top and bottom of the TPC, read out both scintillation signals (S1 and S2) of each event. S1 is used for energy determination, as well as for pulse shape discrimination (PSD). The latter is derived from the ratio of the prompt and delayed light fractions. S2 is used for energy and 3D position measurements of the event, the vertical coordinate is measured from the drift time between S1 and S2, and the horizontal coordinates from the light pattern resulting in the top photosensors from S2.

The octagonal LAr TPC will have a height of 350 cm and a distance between parallel walls of 355 cm. It will be instrumented with a new kind of photosensors, arrays of SiPMs, arranged in assemblies called photodetector modules (PDMs). Each PDM has an area comparable to that of

693 a 3" photomultiplier tube (PMT), with the LAr TPC containing 8280 PDMs in total. Substantial
694 effort was put into the development of this technology, since SiPMs promise a higher effective
695 quantum efficiency, higher reliability at LAr temperature, and a much higher radiopurity than
696 PMTs. All of these properties are crucial for DS-20k since the PSD, which is the most important
697 mechanism for background discrimination in LAr, depends critically on the light yield. Additionally,
698 the large material budget of PMTs is often a limiting factor for neutron- and gamma-induced
699 backgrounds. The LAr TPC will be equipped with arrays of SiPMs, totaling 21 m² in area.

700 In comparison to DS-50, where a full digitization and recording of the waveform of each PMT
701 could be achieved, a custom scheme for the sampling of the two-orders-of-magnitude higher channel
702 count of the DS-20k SiPM PDMs has to be developed. Design parameters for the data acquisition
703 (DAQ) system are driven by rates and occupancies, as well as leading edge timing and limited
704 charge information from each channel, while compromising as little as possible on energy resolution
705 and pulse-shape discrimination.

706 All components of the detector, especially the inner components, like the LAr TPC, the SiPM
707 arrays, and cables, must be made from materials of the highest radiopurity to keep backgrounds as
708 small as possible.

709 The veto detector consists of three separate volumes:

- 710 • An inner volume of active liquid AAr, called the Inner Argon Buffer (IAB), surrounding the
TPC;
- 712 • A passive shell of acrylic loaded with Gd, called the Gd-loaded Acrylic Shell (GdAS), of octagonal
713 shape mounted around the IAB. The GdAS surrounds the TPC in all directions (lateral, top
714 and bottom, with exceptions due to the signal and utility service holes).
- 715 • An outer active volume of AAr, called the Outer Argon Buffer (OAB).

716 A copper cage which acts as a Faraday cage provides the optical insulation from the rest of the
717 AAr external to OAB and, at the same time, it realizes the necessary electric shield for reducing
718 external noise from contaminating the detector signals. The details of the veto design and expected
719 performance are given in Sec. 9.

720 In order to demonstrate and test technological developments on a scale relevant to DS-20k,
721 the collaboration will build and operate a ~1 t prototype. The project is called DarkSide-Proto
722 (DS-Proto) and is described in Sec. 13. DarkSide-Proto will be at an intermediate scale between
723 DS-50 and DS-20k, able to test a number of full size components intended for use in DS-20k. The
724 size of DS-Proto was chosen to be able to validate detector and PDM components, including the
725 readout system, both from the mechanical and performance aspects of the experiment. The full
726 size cryogenic system will also be tested in this way, especially the argon condenser, the gas pump,
727 and the heat recovery system. Functionality and stability control, as well as safety issues during
728 power failures, purification flow rates and general controls are meant to be explored. DS-Proto also
729 serves to validate the readiness of the various production lines in the different institutions of the
730 collaboration to ensure quality control and assurance for the production of components for DS-20k.

731 For the DarkSide-20k detector to reach its physics goals, a comprehensive plan of calibrations for
732 the LAr TPC and Veto detectors is necessary. The calibration equipment and techniques specific
733 to the DS-20k experiment are described in detail in Sec. 8. In addition to this, it will be important
734 to also utilize measurements taken with external calibration experiments placed within the line of
735 sight of a neutron beam. In the SCENE experiment,[33, 34] a monochromatic, low energy, pulsed
736 neutron beam at the Notre Dame Institute for Structure and Nuclear Astrophysics was used to
737 study the scintillation light yield from recoiling nuclei in a small LAr TPC, but only down to
738 57.3 keV_{nr}. The ARIS experiment was exposed to the highly collimated and quasimonoenergetic
739 LICORNE neutron beam at the Institut de Physique Nucléaire d'Orsay (IPNO) in order to study
740 the scintillation response to nuclear and electronic recoils [35].

741 The collaboration is now expanding this external calibration work with a new external calibration
742 experiment, the Recoil Directionality (ReD) experiment, described in Sec. 12. The ReD detector
743 is a small LAr TPC (similar in size to SCENE) equipped with the same SiPM tiles planned for use
744 in DS-20k. ReD is designed to select and measure single neutron elastic scatters on argon nuclei,
745 by means of a large acceptance neutron spectrometer, composed of an array of liquid scintillator

746 detectors. Kinematic requirements of the neutron interactions will allow for the precise detection
747 of nuclear recoils in the LAr, since the neutron energy, scattering angle, and drift field direction
748 can all be precisely measured with the use of external neutron detectors.

749

5. PHOTOELECTRONICS

750 Silicon photomultipliers (SiPMs) are one of the key enabling technologies for large-scale LAr-
751 based dark matter experiments. SiPMs will also play an important role in the next generation of
752 LAr-based neutrino detectors, such as DUNE [10], and liquid xenon based detectors for neutrinoless
753 double beta decay, such as nEXO [37]. SiPMs have a number of performance advantages over
754 traditional PMTs, including higher photon detection efficiency (PDE) and much better single-
755 photon resolution, all while operating at much lower bias voltage. SiPMs can also be efficiently
756 integrated into tiles that cover large areas and feature better radio-purity than PMTs.

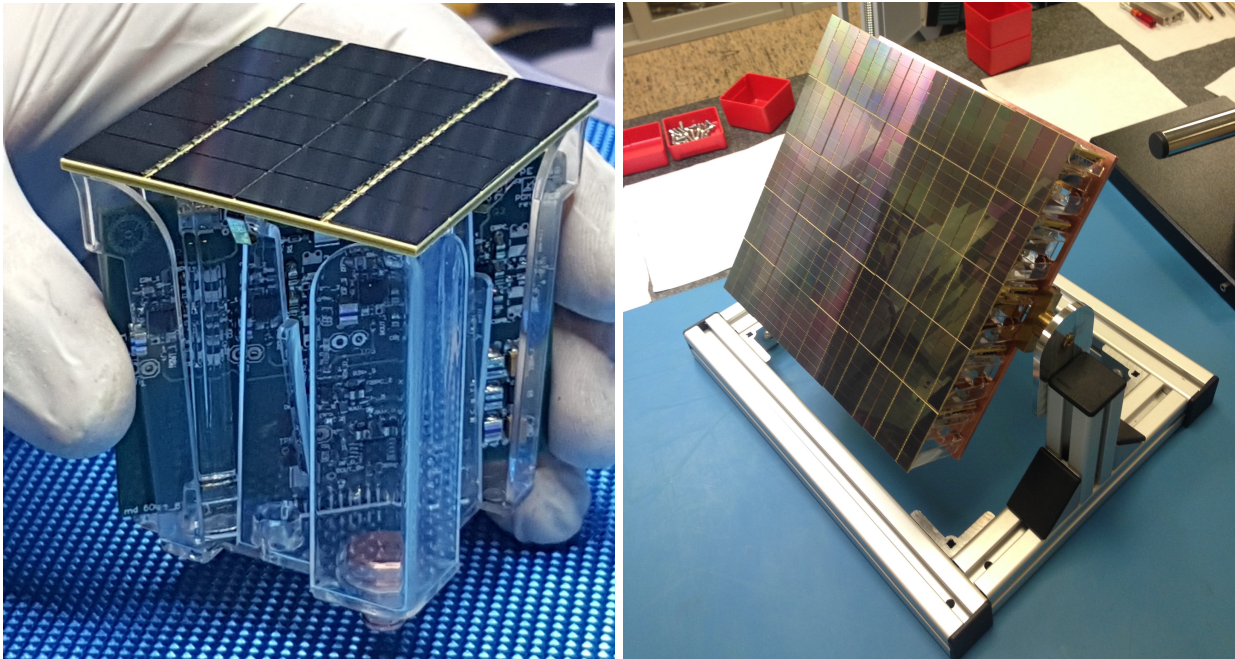


FIG. 6. **Left:** Single channel PhotoDetector Module (PDM) consisting of a $50 \times 50 \text{ mm}^2$ tile of 24 SiPMs and a front-end board. **Right:** The DS-20k motherboard assembled with 25 PDMs.

757

5.1. PhotoDetector Modules (PDM)

758 For DS-20k, the photosensing unit will be a “PhotoDetector Module” (PDM), consisting of a
759 large tile of SiPMs covering a total area of $50 \times 50 \text{ mm}^2$ operating as a single detector (see the left
760 panel of Figure 6). Besides the tile, each module will also contain a cryogenic preamplifier board
761 that will amplify and shape the signal in the immediate proximity of the sensor. The output of
762 the cryogenic amplifier will be passed on to a signal transmitter, also integrated into the PDM,
763 and responsible for transmission of the signal through the cryostat penetration. Finally, the PDM
764 will also include the mechanical structure required to assemble all components and to efficiently
765 dissipate heat in the LAr target, minimizing the production of bubbles. An intelligent power
766 distribution system is also foreseen, capable of disabling individual PDMs in case of failure.

767 The unique challenge in readout presented by SiPMs is mainly due to their capacitance. At
768 50 pF/mm^2 , a single SiPM with a $5 \times 5 \text{ mm}^2$ surface area passes the nF scale for capacitance. Yet,

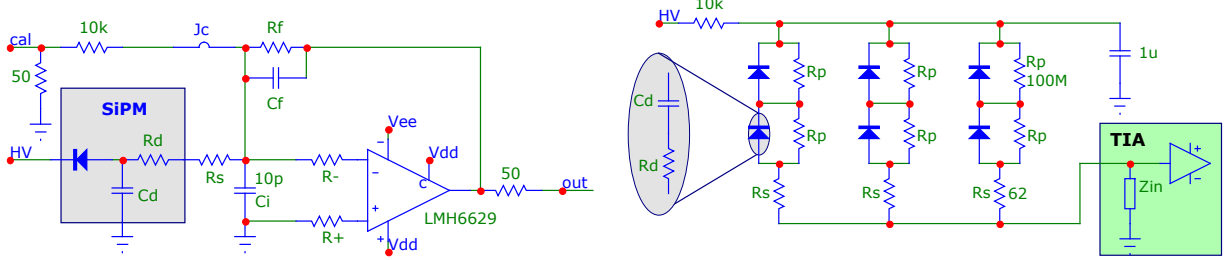


FIG. 7. **Left:** Schematic diagram of the transimpedance amplifier circuit developed to readout SiPMs. **Right:** Schematic diagram of the 2s3p readout scheme optimized for summing six SiPM signal together.

the experiment foresees a photo-sensing area of 21 m^2 . The readout of a LAr calorimeter faced a similar challenge, with capacitance for the individual cells often passing the nF scale [51]. Early developments on LAr calorimeter readout [52–55] demonstrated that the use of a transimpedance amplifier (TIA) is preferable to a charge integration amplifier where the noise and rise time are very strongly affected by the large detector capacitance. With this in mind, the DarkSide Collaboration has developed and optimized a TIA (schematic is shown in the left panel of Figure 7) with performance at 87 K in mind [25]. The specific goal was to maximize the amplification factor while preserving a stable signal bandwidth and SNR.

The SiPMs readout scheme strongly affects the PDM performance in terms both of SNR and bandwidth of the signal. A hybrid readout scheme, with parallel-series combination of SiPMs, first introduced for the MEG experiment [56, 57], solves at once these two problems. In this configuration, the output signal of an individual SiPM is reduced by a factor equal to the number of SiPMs put in series, but this disadvantage is offset by the attenuation of the noise gain due to the reduction in the input capacitance. Most importantly, a strong improvement of the bandwidth with respect to the parallel readout scheme is achieved, with six SiPMs easily readout by connecting in parallel three branches of two SiPMs put in series (known as the 2s3p configuration [26], see right panel of Figure 7) with a bandwidth comparable to the one achievable with a single SiPM in input. Four such readout quadrants are fit in a single PDM, with their output signals summed at the transmission stage.

788

5.2. Signal Transmission

789 The signal transmission from the PDMs to the warm electronics is of primary importance for
 790 the experiment. Given the high number of independent channels, cables would introduce a large
 791 mass in the cryostat with the inherent problems of radio-purity and heat load. The delivery of the
 792 PDM signals to the outside world through optical fibers will solve at once these two problems. For
 793 this purpose an optical analog cryogenic transmitter has been developed. The prototype boards
 794 of the opto-link system (optical driver and optical receiver board) have been recently produced.
 795 The optical receiver board (32 channels) was successfully tested, while the optical driver board (25
 796 channels) is at the moment undergoing testing.

797 The PDMs will be located above the anode and below the cathode, fully covering the top and
 798 bottom faces of the LAr TPC active volume, to detect both the S1 and S2 signals with high
 799 efficiency. The top and the bottom photon readout assemblies will consist of 4140 PDMs each.
 800 Multiple PDMs are mounted to a single motherboard to form two larger basic mechanical units
 801 called the square board (SQB) and the triangular board (TRB), described in Sec. 6.6.1 and shown
 802 in Figure 13. The SQB and TRB have the same edge size of 25 cm. The SQB and TRB are then
 803 used to form the full readout planes (shown in Figure 12). The total number of readout channels
 804 (top and bottom) is 8280.

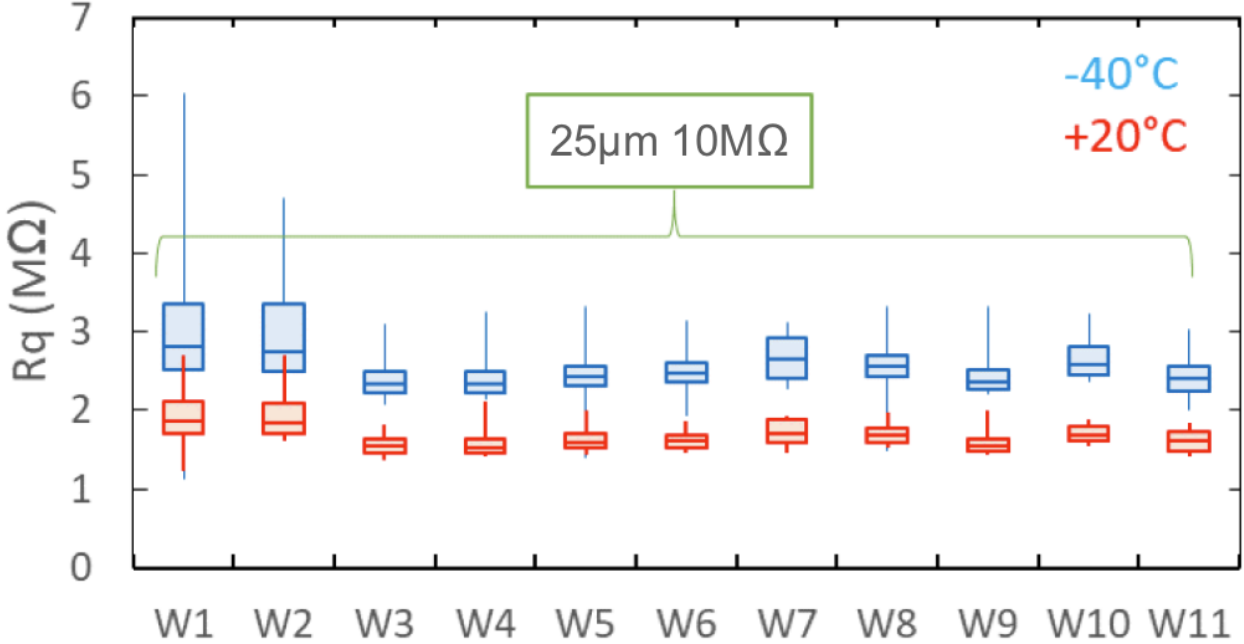


FIG. 8. Average SiPM quenching resistor value vs. wafer number measured at 20 °C and –40 °C.

5.3. PDM Fabrication and Characterization

Following the successful construction of the first Photo-Detector Module (PDM) in March 2018, the Photo-Electronics Working Group proceeded to the construction of the first Motherboard, shown in Figure 6. The FBK company delivered two SiPM runs: the first one with standard doping SiPMs (cell size $25 \times 25 \mu\text{m}^2$ and quenching resistor $10 \text{ M}\Omega(77 \text{ K})$) and the second one with triple doping SiPMs (cell size $30 \times 30 \mu\text{m}^2$ and quenching resistor $5 \text{ M}\Omega(77 \text{ K})$). Since the latter SiPM type is considered the best candidate for the DS-20k experiment, we decided to use the single doping SiPMs for the first Motherboard construction, so that the triple doping type could be mounted later, taking advantage of the experience gained with the mounting of the first Motherboard.

This SiPM run was characterized by a reasonable yield at –40 °C of about 50 %. A detailed inspection of the SiPM quenching resistor (R_q) showed good uniformity for most of the wafers, while the first and the second wafers (W1,W2) had a 20 % larger R_q (see Figure 8). The optimal working voltage of the SiPM is expected to change as a function of R_q , so in the forthcoming mass production by the LFoundry company, where hundreds of 8 " SiPM wafers are scheduled, this quenching resistor spread is not an issue since the SiPMs with similar R_q can be paired. In this way, each Motherboard, with PDMs biased at the same voltage, will be made of devices with similar R_q . Due to the limited SiPMs available in the present production we had to use all of them to make the first Motherboard, and thus all were biased with a common voltage despite the slight difference in R_q . As a consequence, the tiles made with SiPMs belonging to wafers 1 and 2 were fed with an overvoltage lower than the optimal one for some of the SiPMs, i.e. 5 V. It is worth noting that a dedicated facility for the Motherboard production is not available yet, and therefore the use of equipment through outsourcing and additional man power was therefore required.

The tile and the Front-End Board PCBs were made with an Arlon 55-NT substrate, following the experience gained during the first PDM construction. The electronic components were mounted with outsourced equipment, under the supervision of LNGS personnel. The tile PCBs were tested both at warm and at cryogenic temperatures to verify the correct circuit impedance. After the wafer dicing, the SiPMs were shipped from FBK to Princeton University, where the first Motherboard tiles were bonded by personnel from LNGS, Princeton University and TIFPA. A cryogenic epoxy for the SiPM back-side and a wire-bonding connection for the front-side was used. The 27 tiles, each made of 24 SiPMs, were then shipped to LNGS, using multipurpose acrylic boxes, designed

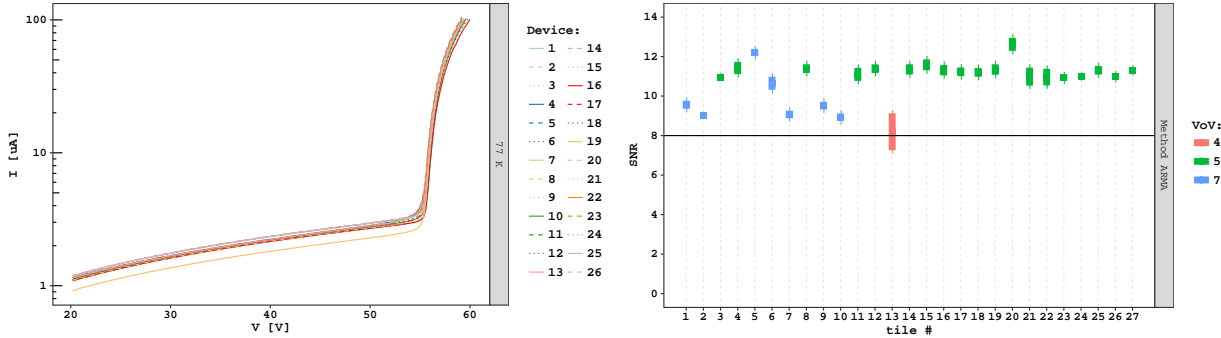


FIG. 9. **Left:** Reverse I-V curves for the SiPM tiles measured at 77K. **Right:** SNR of the 27 bonded SiPM tiles.

by the Pisa group. This box allows for safe shipping of the tile, offering an adequate protection of the SiPM wire bonding and, at the same, time allows the tile characterization in liquid nitrogen by permitting the insertion of the Front End Board without removing the tile from the box. The tiles underwent a comprehensive test at LNGS both at warm temperature and in LN, including the reverse I-V curve measurement, the power spectrum and the charge spectra. We found just one tile out of the 27 with two SiPM branches (4 SiPMs) not working properly. Another tile showed a noise level higher than the average. These two tiles were therefore excluded from the list of the tiles selected to populate the first Motherboard.

As an example, the left side of Figure 9 shows the tile I-V curves taken at 77K, indicating a homogeneous behavior.

The right panel of Figure 9 shows the signal to noise ratio (SNR) for the 27 tiles at their optimal voltage. It is worth noting that all of them have a SNR larger than the minimum SNR of 8, required by the DarkSide-20k experiment specifications. For each tile, the SNR was obtained relying on several different procedures and analysis methods. The bar length in the figure represents the spread of each measurement, depending on the method used. The signal-to-noise ratio (SNR) is defined as the ratio between the gain and the width of the baseline noise peak. The gain is measured by fitting the center values of the amplitude multiple peaks and evaluating the slope of a linear fit. The baseline noise is extracted from the average standard deviation of the waveform in a pre-pulse window, 500 ns long, using 500 samples. For most tiles, the distribution of the standard deviation is not symmetric around the peak. The most important contribution to the noise baseline is the presence of one or more photoelectrons not stimulated by the laser pulse. These can originate from a SiPM having an excess of dark-rate or more probably by an excess of after-pulsing.

Since the distribution is not symmetric, the estimate of the baseline noise is intrinsically biased and two options are possible, corresponding to the mean value or the most probable value (mode). Consequently the SNR is defined in a confidence interval between $\text{SNR}_{\min} = \text{gain}/\text{noise}_{\text{mean}}$ and $\text{SNR}_{\max} = \text{gain}/\text{noise}_{\text{mode}}$.

Figure 10 shows the SNR obtained with the common over-voltage of 5 V. Although a few tiles, as expected, manifest a SNR slightly below 8, the SNR is quite good for all tiles used in the assembly of the first Motherboard.

864

5.4. Motherboard Assembly

Before assembling the first Motherboard, a full mock-up made of an aluminum Motherboard structure, an FR4 Motherboard strip PCB, 25 dummy tiles and FEBs, and the PDM acrylic mechanics was mounted at Bologna. Each PCB had the same dimensions of the final one, while the HV/LV and signal layers were not included in the stack-up. The mounting required just a few hours and the overall procedure was validated, while the mechanics of the different components nicely merged, suggesting just a few minor mechanical improvements.

After these tests, the tiles were finally shipped to Pisa, while the PDM pillars and the copper

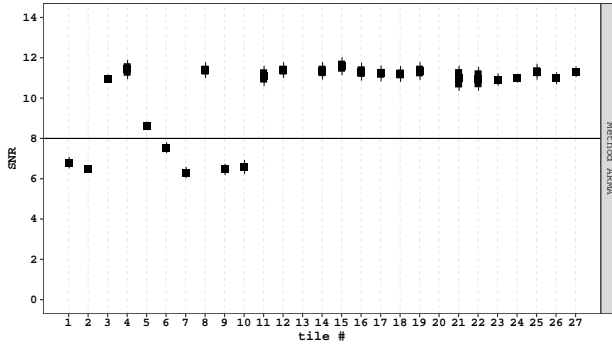


FIG. 10. SNR of the 25 SiPM tiles populating the first motherboard while operating the SiPM tiles at an over-voltage of 5 V.

872 Motherboard structure were milled at Bologna using 99.997 % pure copper sold by the Luvata
 873 Company. The first Motherboard was equipped with a PCB strip connecting the PDMs, made of
 874 a thin stack-up (0.5 mm) based on a Pyralux substrate and shipped to Pisa to start the mounting
 875 of the 25 PDMs on the Motherboard.

876 The PDMs were assembled in the Pisa clean room, following the prescriptions used for the first
 877 PDM, assembled in March 2018. The mounting of the 25 PDMs on the Motherboard was finalized
 878 in few days. A picture of the first Motherboard, fully equipped with the first 25 PDMs is shown in
 879 the right panel of Figure 6.

880 In summary the construction of the first Motherboard required the production, testing, selection
 881 and bonding of more than 600 SiPMs. Although a cryogenic probe and an automatic bonder were
 882 not available yet, the Collaboration was able to increase the number of successfully built PDMs
 883 from 1 to 25, in just 6 months. The bonding yield exceeded 95 % (just 1 tile out of the 27 showed
 884 problems with the SiPM bonding strategy), while the satisfactory PDM SNR demonstrated the
 885 validity of the full Motherboard construction process.

886 After the completion of the first motherboard, equipped with 25 PDMs each containing 24 single
 887 dose SiPM's, the collaboration moved to the construction of a second Motherboard, equipped with
 888 triple dose SiPMs. At the moment, half of the PDMs have already been assembled and mounted
 889 in the copper structure. The remaining PDMs will be mounted within the summer of 2019. The
 890 FEBs were already successfully tested, while the SiPM tiles are currently undergoing testing in
 891 LN. The next step in the photo-electronics schedule is the production of about 400 PDMs for the
 892 DS-Proto detector. These SiPMs will be produced by the LFoundry Company in Avezzano, Italy.
 893 The first run is expected in the summer of 2019.

894

5.5. Mass Production

895 The first engineering run, finalized in September 2018 and tested shortly after, showed the
 896 capability of the silicon foundry to implement the FBK technology. The produced SiPMs showed
 897 good performance at both room temperature and in liquid nitrogen. A second LFoundry engineering
 898 run, presently ongoing, is devoted to the development of the through silicon vias (TSV). This post-
 899 production rework requires some delicate mechanical manipulation of the SiPM wafers.

900 The DS-20k SiPM packaging foresees the production of more than 10 000 PDMs in 2.5 yr. This
 901 remarkable effort requires a large clean room, relying on cutting edge technology equipment and
 902 trained personnel. The GADM selected for the NOA DS-20k SiPM packaging facility a clean room
 903 at the *Tecnopolo dell'Aquila*, with surface exceeding 700 m². The clean room will be soon refurbished
 904 to comfortably host the needed equipment and personnel. This facility will be managed by GSSI,
 905 through an agreement with INFN that will soon be finalized. Concerning the procurement of the
 906 equipment for the DS-20k PDMs mass production, the cryogenic probe tender was just approved
 907 by the INFN Executive Board and the flip-chip bonder tender will follow in the weeks to come.

DS-20k TPC Dimensions	
TPC Drift Length	350 cm
Octagonal Inscribed Circle Diameter	355 cm
Total LAr Mass	51.1 t
Active LAr Mass	49.7 t
Fiducial Cut Distance (vertical)	70 cm
Fiducial Cut Distance (radial)	30 cm
Fiducial LAr Mass	20.2 t
Nominal TPC Fields and Settings	
Drift Field	200 V/cm
Extraction Field	2.8 kV/cm
Luminescence Field	4.2 kV/cm
Cathode Voltage	-73.8 kV
Extraction Grid Voltage	-3.8 kV
Anode Voltage	ground
Gas Pocket Thickness	7 mm
Grid Wire Spacing	3 mm
Grid Optical Transparency	97 %
SiPM PDM	
Number of PDM on TPC Top	4140
Number of PDM on TPC Bottom	4140
PDM Effective Area	50 × 50 mm ²

TABLE II. DS-20k LAr TPC detector parameters.

908

6. INNER DETECTOR AND CRYOGENICS SYSTEM

909

6.1. DS-20k LAr TPC

910 The DarkSide-20k LAr TPC is the dark matter detector and the central element of the experiment,
911 with all auxiliary detectors and systems specified and designed in support of it. The DS-20k
912 LAr TPC will use 50t of LAr extracted from an underground source as the target material for
913 WIMP detection. An ultra-pure acrylic vessel is used to contain the LAr. Features directly fabri-
914 cated onto the inner surfaces of the acrylic vessel will form the TPC itself. These feature are the
915 TPC field cage system, the anode and the cathode and are implemented on the acrylic panels with
916 a commercial conductive polymer coating, called Clevios™. Use of this coating eliminates the use
917 of metal conductive materials.

918 The same pure acrylic material, in the form of 4 mm thick sheets, is used to hold the Enhanced
919 Specular Reflector (ESR) reflector foils installed to maximize light collection. The TPC is designed
920 such that all the inner surfaces facing the active volume are coated with TPB, a wavelength shifter,
921 to ensure the complete conversion of the 128 nm argon scintillation light to 420 nm, where the
922 SiPMs' peak in their PDE. Two identical photosensor arrays of 4140 channels each are placed on
923 top and bottom of the TPC, but outside of the acrylic vessel. The TPC is mounted inside a neutron
924 veto detector, whose most important component is a 10 cm thick, gadolinium loaded, acrylic shell
925 that completely encapsulates the TPC. This plastic shell defines two 40 cm thick active volumes,
926 respectively named the inner and outer buffer, filled with liquid AAr. The buffers are further
927 segmented with ESR, also coated with TPB. The whole apparatus is placed inside a light and
928 electromagnetic shield barrier, contained in the ProtoDUNE-like cryostat filled with AAr.

929 **Sealed PMMA Vessel:** An acrylic (PMMA) vessel will be used to confine the UAr rather than
930 a metallic vessel, since PMMA is extremely radiopure, resulting in a residual neutron background
931 estimated to be $<10^{-3}$ for the exposure of 200 t yr. As described above, the TPC active volume is
932 confined in all directions by the sealed PMMA vessel that is formed by bonded plates or panels.
933 In order to use the UAr more efficiently, all the UAr will be sealed in this PMMA vessel, so that
934 no other external vessel will be required (as shown in Figure 11). The body of the PMMA vessel
935 will be fused together by 5 cm thick acrylic plates, and then flanged and sealed with the top and
936 the bottom lid, that serve as the anode plate and cathode plate of the TPC, respectively.

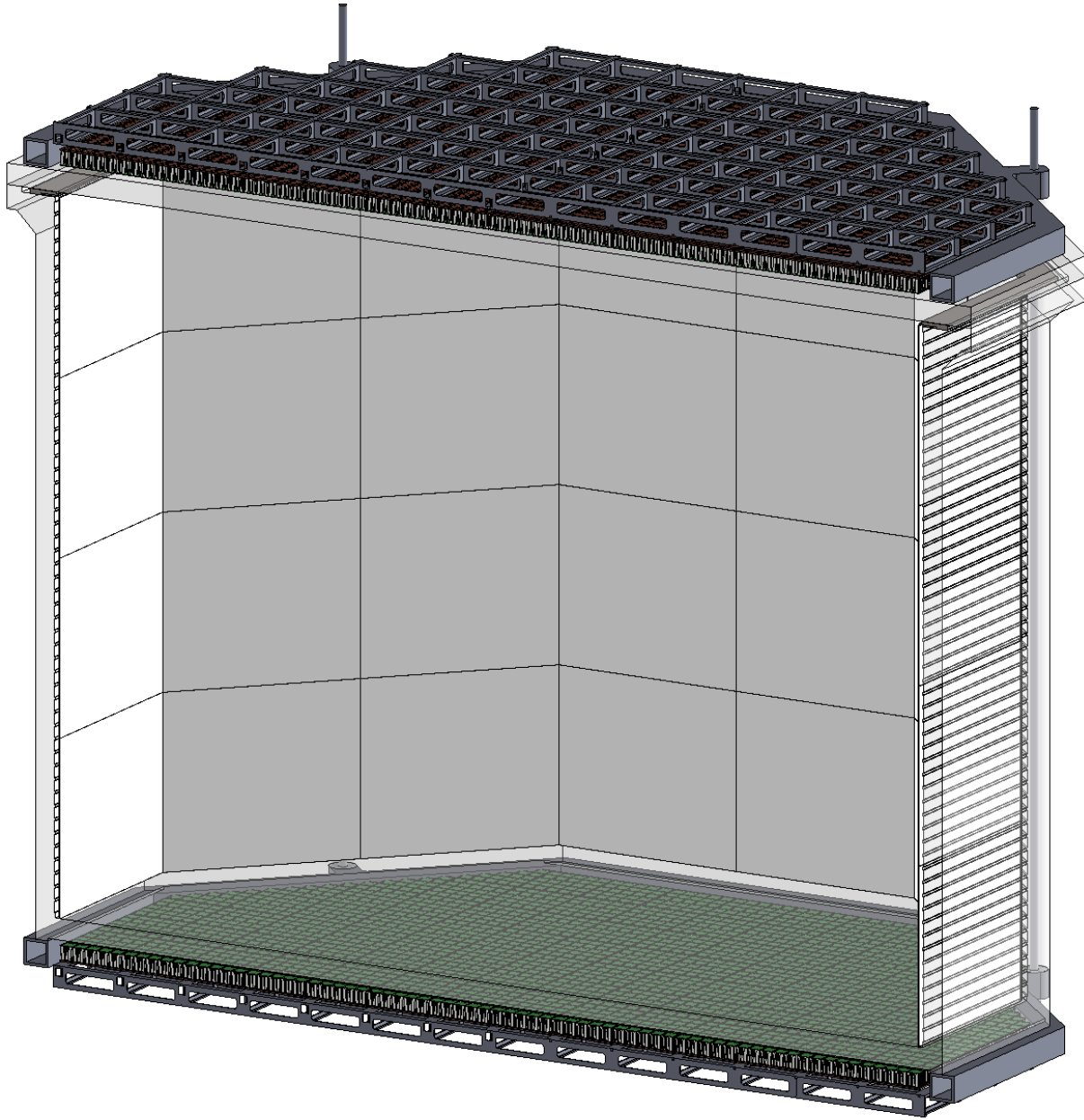


FIG. 11. Artist rendering of the PMMA vessel and the TPC.

937 The ESR-acrylic reflector panels are located inside the acrylic vessel. The top and bottom PDM
 938 arrays are placed outside of the acrylic vessel, immersed in the AAr of the neutron veto detector.
 939 PDM arrays will be isolated from any light generated in the veto detector. In this way, 97.3 % of
 940 the total argon is active, resulting in the most efficient usage of UAr. All cables, HVFTs, and most
 941 mechanical structures are moved outside of the UAr volume as well, resulting in less outgassing
 942 and hence higher purity of the UAr.

943 The HV Cathode connection through the acrylic vessel is being studied and a new design will be
 944 tested to adapt the cable connection to the cathode itself. The acrylic vessel design integrates the
 945 HV connection so that the contact point is outside the vessel. In this case, both the HV cable and
 946 the HVFT are in the AAr volume. The HVFT will penetrate through the veto cryostat.

947 A commercial conductive and transparent Polymer coating, CleviosTM, is found to be a very

948 promising alternative to the traditionally used indium tin oxide (ITO) thin film coating. CleviosTM
949 is being used in industrial applications such as transparent electrodes for touch panels and printed
950 electronics. The main advantage of CleviosTM is its composition. Being a water-based solution, the
951 large-area coating needed for the anode and cathode will be easier to accomplish with respect to an
952 ITO coating. A sample of 100 g has been procured for the radioactivity assay. The initial ICP-MS
953 assay results from PNNL are encouraging, and further analysis of Rn emanation is scheduled at
954 Krakow. In terms of the optics, three coating samples of CleviosTM on acrylic plates were provided
955 by The Heraeus Company. The wet coating thickness of each sample is 4 μm , 8 μm and 12 μm ,
956 respectively, and their transparency has been measured at Princeton University. A 1.5 % absorption
957 at 420 nm was observed for a 4 μm thick CleviosTM layer, which is a good result comparable to
958 the 98 % transparency of ITO measured in DS-50. Further studies, including coated thickness
959 resistivity, TPB coating on CleviosTM, and durability in LAr are ongoing. Besides the anode and
960 cathode, the new design replaces the bulky copper field shaping rings with CleviosTM conductive
961 coatings. Consequently, the use of this polymer will reduce the expected background, as well as
962 the total cost, and make the fabrication and installation of the TPC simpler.

963 **LArTPC Size Consideration:** Since the SiPM tiles are all square shaped, the DS-20k TPC
964 will be an octagonal shape to best fit the coverage of the PDM, while optimizing the fiducial mass.
965 The size of the TPC is determined by the patterning strategy of the SiPMs, driven by the design
966 size of the square and triangular motherboards (SQB and TRB, respectively). Figure 12 shows
967 the current SiPM pattern strategy for both the top and bottom arrays. Each array consists of 156
968 SQBs and 16 TRBs. Each TRB contains 15 PDMs and each SQB contains 25 PDMs, as shown
969 in Figure 13. Thus, the number of PDMs used in each array is 4140, while the total number
970 envisioned in the TPC is 8280. Based upon this pattern strategy, and considering that the edge
971 of the active volume of the TPC will shrink about 2.7 cm from the edge of the SiPM array, the
972 distance from edge to edge of the octagonal active volume will be 355 cm. The height of the TPC
973 will be 350 cm. With this design, the total mass of LAr in the active volume and fiducial volume
974 (with 70 cm vertical and 30 cm lateral cuts) are 49.7 t and 20.2 t respectively.

975 **Reflector Panel:** In order to get rid of the conventional PTFE reflectors, which would be the
976 predominant source of neutron background and Cherenkov background due to the enormous mass
977 required for DS-20k, ESR foils will be used as the TPC reflector. The ESR is a thin layer foil which
978 has reflectivity of 98 % for 420 nm light, with a thickness of only 50 μm . In order to hold the ESR
979 foils in place and maintain their flatness during the operations, 4 mm thick UVT acrylic sheets will
980 be used. The thickness of the backside acrylic sheet is chosen to be 4 mm, providing the panels
981 with enough strength to maintain the flatness of the ESR foils. The surface of each ESR foil facing
982 the active LAr volume will be coated with TPB.

983 The entire reflector panel of the TPC is shown in Figure 14. The ESR mountings are strategically
984 arranged such that no gaps can develop during the cool down of the TPC, hence guaranteeing 100 %
985 TPB coverage. Each ESR-acrylic sub assembly will be fixed by several acrylic screws, with the screw
986 heads facing the active volume. To avoid losing any light, each head of the screw will also be coated
987 with TPB. By design, some space is left between the acrylic and the ESR to allow venting of any
988 gas during the filling with LAr, but also to allow the LAr to fill the space between the back of the
989 ESR and the acrylic panel. The flat and corner assemblies will be mounted on the field cage, which
990 is attached to another set of acrylic structures by PTFE screws. The ESR holding panels are not
991 connected at the corners in order to accommodate the shrinkage when the assemblies are cooled to
992 LAr temperature. Overlaps between ESR foils at each joint are also designed for the same reason.
993 A small mock-up to mimic the shrinkage has been built at UC Davis, whose results have confirmed
994 the design concept. Repeated tests in liquid nitrogen showed that all parts moved in the desired
995 way during cooling down and warming up, which proves the design idea.

996 **Field Region:** Within the sealed acrylic vessel, the electrode features of the TPC are realized
997 using the CleviosTM conductive polymer coated directly onto the acrylic vessel. The inner surface
998 of the acrylic vessel will be machined with grooves such that recessed areas have geometries similar
999 to an electrode ring, and when coated with the CleviosTM comprise the TPC field-shaping rings
1000 that are highly uniform across the height of the TPC.

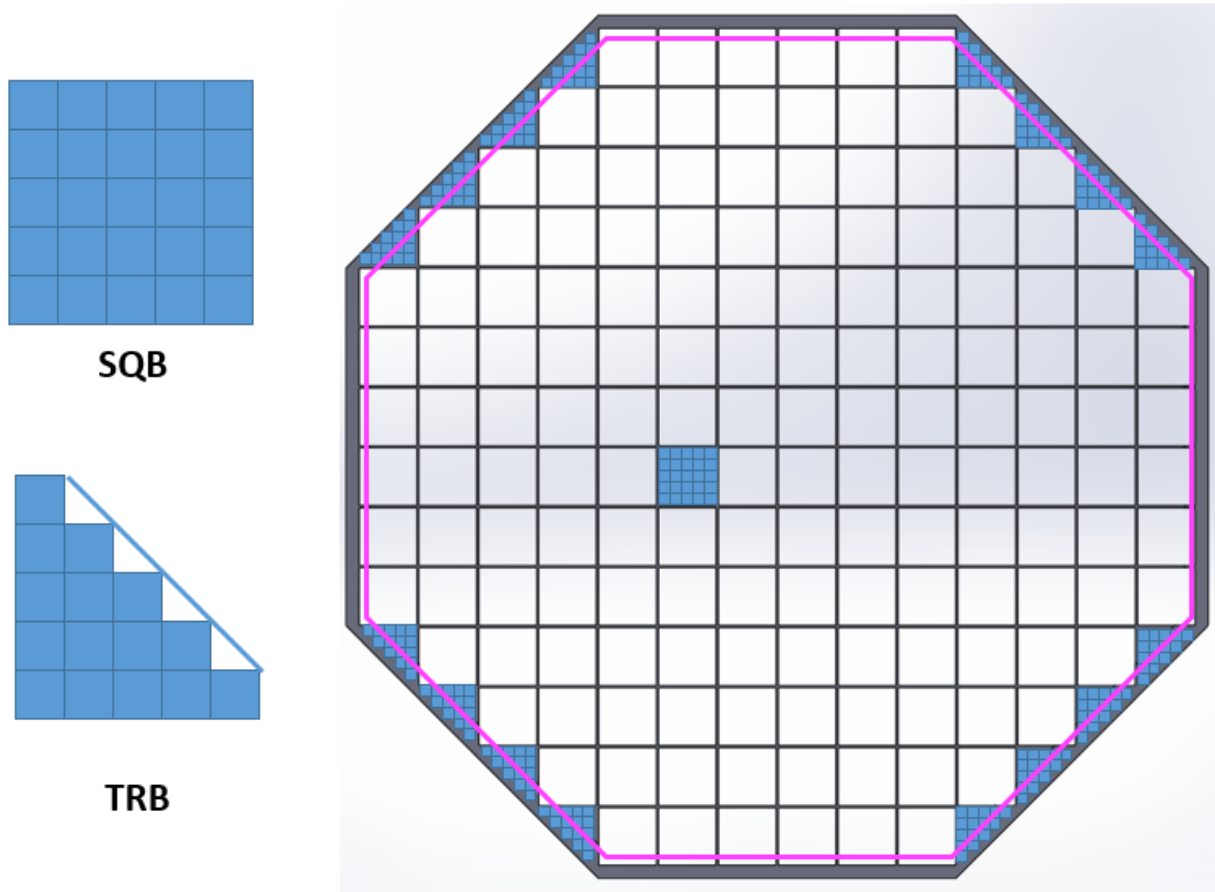


FIG. 12. Patterning scheme for the PDMs. Pink lines indicate the edges of the TPC active volume.

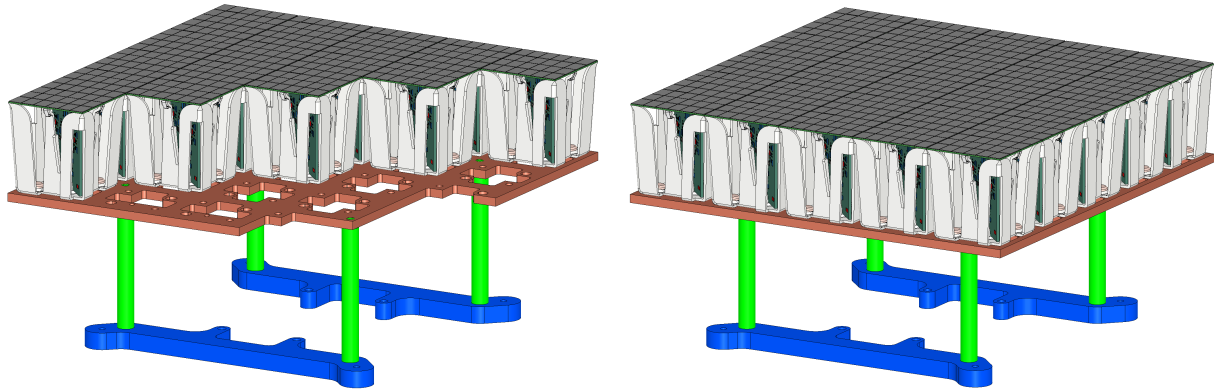


FIG. 13. Schematic drawings of the two types of DS-20k PDM motherboard arrangements. **Left:** triangular with 15 PDMs arranged for center and edge placement. **Right:** square with 25 PDMs.

1001 The relative permittivity of LAr and GAr are 1.54 and 1.03, respectively. By applying electric
 1002 potentials of zero, -3.8 kV , and -73.8 kV to the anode, extraction grid and cathode, respectively,
 1003 three different field regions are formed in the TPC:

- 1004 • The uniform drift field of 200 V/cm in the liquid phase, formed by the geometry of the field cage.
 1005 The drift distance between the cathode CleviosTM layer and the extraction grid is 350 cm ;
 1006 • The extraction field in the liquid phase above the grid is 2.8 kV/cm . The distance between the

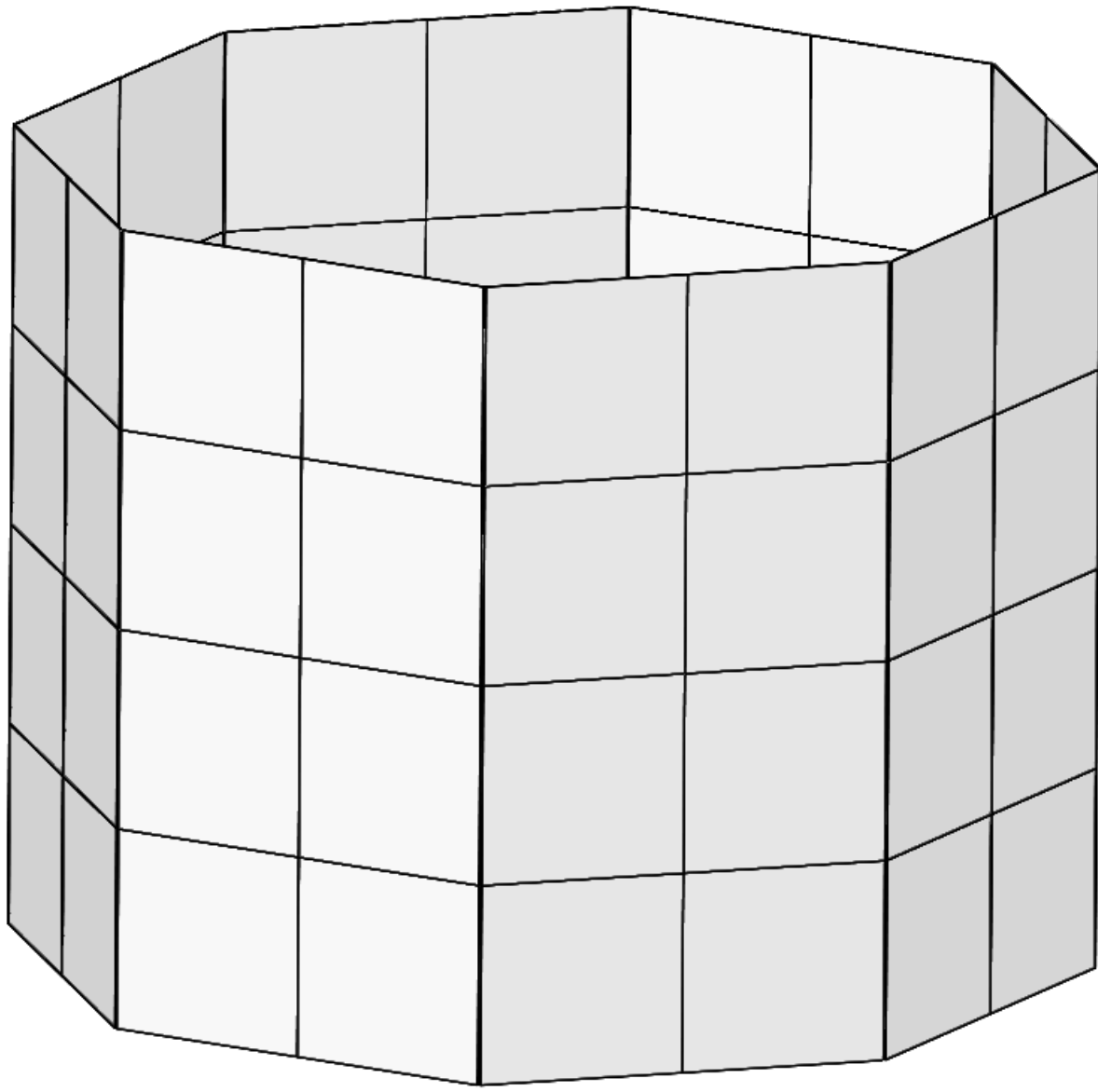


FIG. 14. 3D model of the full DS-20k LAr TPC reflector panels system.

1007 extraction grid and the surface of the LAr is 3 mm;

- 1008 • The electroluminescence field in the gas phase is 4.2 kV/cm. The gas gap between the surface of
 1009 the LAr and the CleviosTM layer acting as the anode is 7 mm thick.

1010 These values are based on the settings used for DS-50, while since the DS-20k gas pocket will be
 1011 operating at a higher pressure, the extraction and luminescence fields will be scaled by the ratio of
 1012 the electric field to the pressure of the gas pocket. The final values to be used will be confirmed with
 1013 the DS-Proto detector that is designed to confirm final design choices for the DS-20k LAr TPC.

1014 As the top boundary of the active volume, a 5 cm thick acrylic window serves as the diving bell
 1015 to maintain a stable gas pocket. A thin layer of CleviosTM conductive polymer is coated on the
 1016 inner surface to act as the anode and a layer of TPB coated onto the CleviosTM layer to shift the
 1017 scintillation light wavelength. The CleviosTM layer coating geometry is optimized for gas pocket
 1018 electroluminescence field uniformity, as shown in the left panel of Figure 15. Right below the liquid
 1019 surface is the extraction grid, composed of stainless steel wires (not shown in figure) stretched in

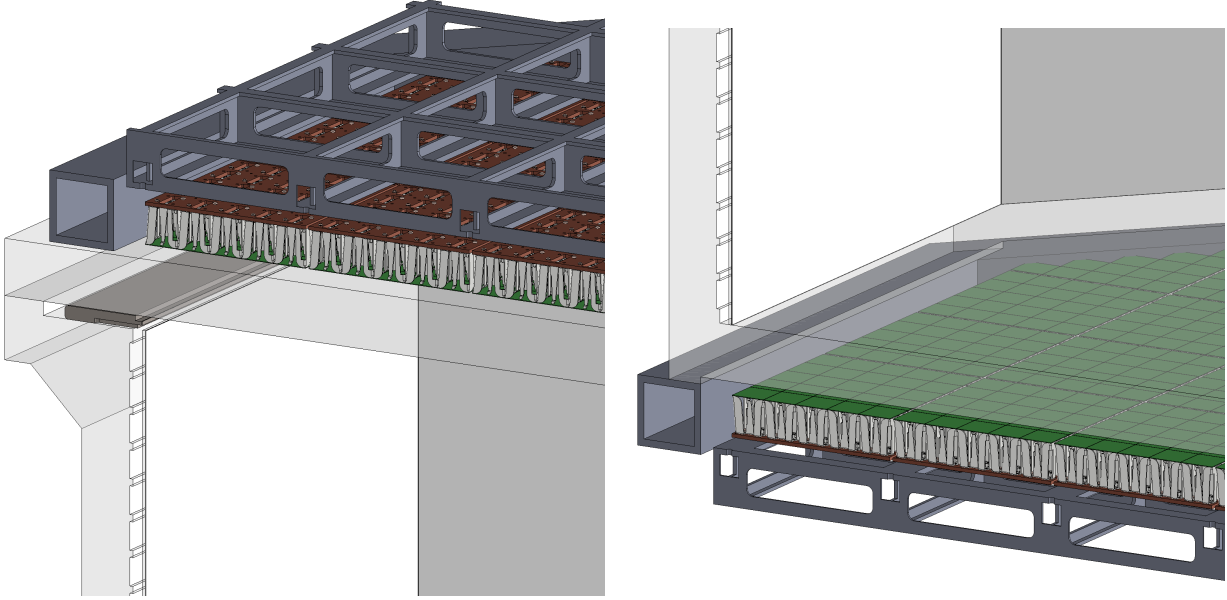


FIG. 15. **Left:** 3D model of the LAr TPC anode and extraction grid region. **Right:** 3D model of the LAr TPC cathode region.

1020 parallel with 3 mm spacing and held in place via small posts set into a stainless steel frame. Slots
 1021 going in the radial direction and on the rim of the acrylic diving bell act as a concentric guide,
 1022 to compensate the different thermal expansion coefficients between the acrylic and stainless steel
 1023 while maintaining precise alignment. The LAr level will be maintained at the top surface of the grid
 1024 frame. Suitable tensions will be pre-loaded on each of the grid wires to minimize the sagging, an
 1025 effect that would distort the electroluminescence field. The frame must be stiff enough to sustain
 1026 the total tension load of all wires, while having as little mass as possible. Both simulation studies
 1027 and prototyping tests are well underway and have presented a feasible design for the extraction
 1028 grid.

1029 The bottom boundary of the active volume, shown in the right panel Figure 15, is a 5 cm thick
 1030 acrylic window coated with a thin layer of Clevios™ on both sides. A layer of TPB will be coated
 1031 on the top Clevios™ layer for wavelength shifting. The edge of the top Clevios™ layer is in
 1032 contact with a C-profile feature on the walls of the acrylic vessel, which acts as a field shaping
 1033 ring and smooths the electric field lines in the corner of the cathode region. Similarly, the bottom
 1034 Clevios™ layer is in contact with a smoothing-profile solid guard copper ring to provide connection
 1035 for the ground bias and electric field minimization. The 5 cm thick acrylic window can easily sustain
 1036 the applied electric field with this design. Figure 16 shows the full field mapping modeled with
 1037 the COMSOL Multiphysics software. Since the vessel is sealed, there is no path for HV to break
 1038 through the acrylic at the cathode region. To confirm this, a full scale mock-up will be built to
 1039 confirm the cathode HV delivery method around the acrylic vessel bottom. The bottom surface of
 1040 the cathode acrylic window will have a convex shape to avoid bubble accumulation. Any bubbles
 1041 generated by the bottom photon detector array, or any other parts, will be driven outwards and
 1042 rise to the top of the AAr cryostat.

1043 A one tonne-scale prototype with full features of the DarkSide-20k TPC will then be built to
 1044 validate the design comprehensively. General considerations, such as the requirements of surface and
 1045 bulk contamination, coating procedures, handling and bonding of acrylic, are based on knowledge
 1046 available within the GADMC. Detailed plans and procedures are currently being developed. All
 1047 mock-up designs and tests will use final DS-20k geometries and full size components in order to
 1048 confirm the validity of the final DS-20k mechanical design and functional parameters. The DS-20k
 1049 LAr TPC parameters are summarized in Table II.

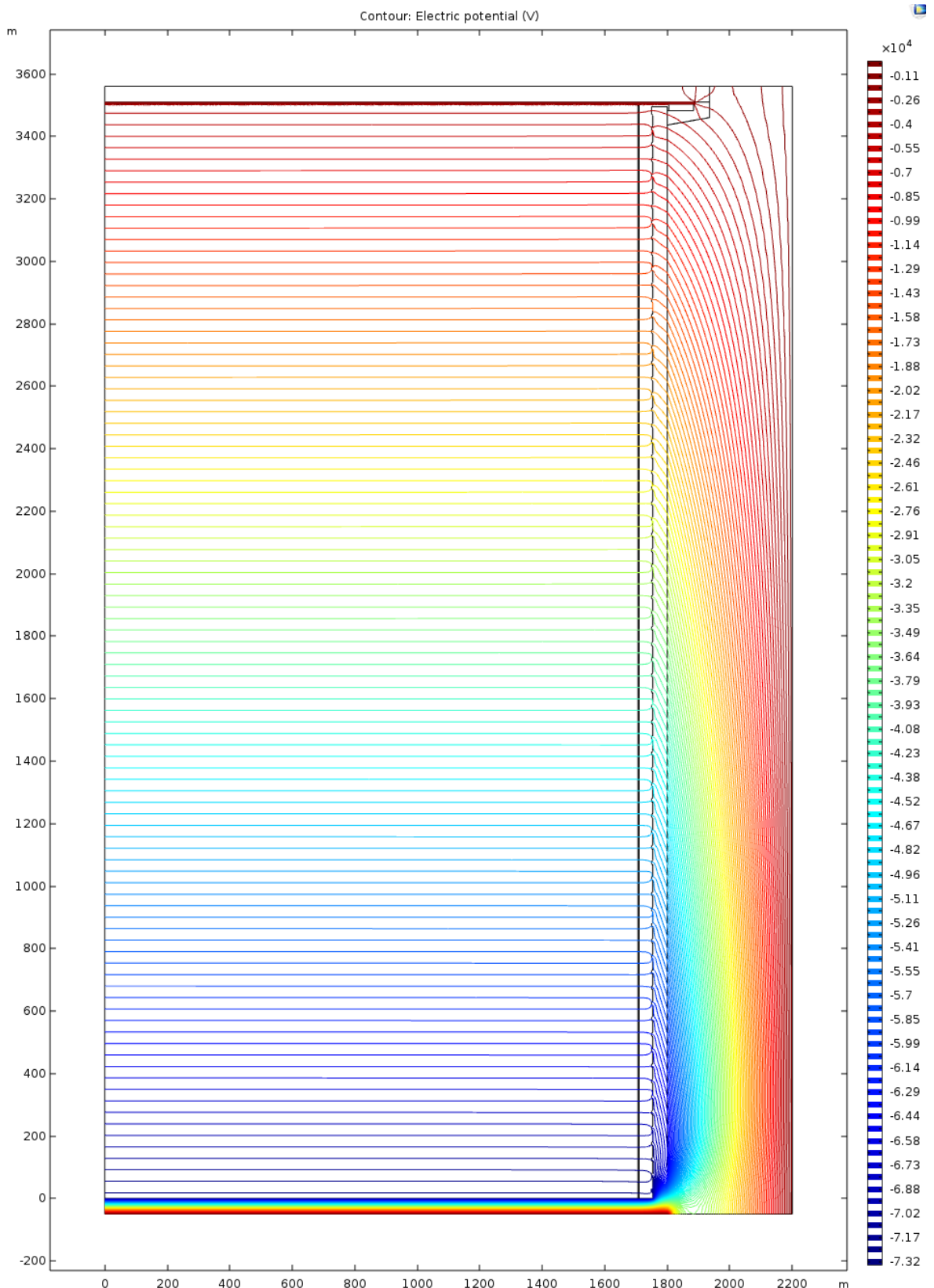


FIG. 16. Equipotential lines mapping in the DS-20k TPC showing an extremely uniform field distribution, modeled with the COMSOL Multiphysics program. Parameter settings for the calculation are those defined in Table II.

Parameter	Value
ProtoDUNE Cryostat parameters for AAr	
ProtoDUNE Cryostat inner width	8548 mm
ProtoDUNE Cryostat inner height	7900 mm
LAr height in ProtoDUNE Cryostat	7500 mm
Total AAr in ProtoDUNE Cryostat	700 t
ProtoDUNE Cryostat insulation per unit area	6.5 W/m ²
Thermal Heat Load of ProtoDUNE Cryostat	2.7 kW
TPC PDM Cold Electronics Power	1.5 kW
Veto PDM Cold Electronics Power	0.5 kW
AAr System Design Mass Circulation Speed	10 000 std L/min
Minimum heat recovery efficiency of AAr heat exchanger	>95 %
AAr Turn Over Time	30 d
Total Cooling Power Required	10 kW
LAr boiling threshold at 3 m depth	60 mW/cm ²
Minimum AAr condenser cooling power to hold LAr inventory	2.7 kW
ProtoDUNE AAr top pressure	1.075 bar
TPC Cryogenics Parameters for UAr	
Total UAr mass during normal operation	51.1 t
TPC UAr Cryogenics Design Mass Circulation Speed	1000 std L/min
Minimum heat recovery efficiency of UAr heat exchanger	>95 %
UAr Turn Over Time	20 d
Total Cooling Power Required for UAr	500 W
UAr Turn Over Time	20 d
UAr electron lifetime required for stable S2 generation	>5 ms (<0.01 ppb O ₂ equiv.)
Pressure stability achieved in DarkSide-50	0.023 psi (RMS)
Nominal flow rate of single DarkSide-20k GAr circulation pump	500 std L/min
Total mass of LN ₂ storage in cooling system	30 t
Efficiency of radon purification by activated charcoal trap	<2 μ Bq/kg after trap
Maximum required helium leak rate at all welds and joints	2×10^{-9} std cm ³ /s

TABLE III. DarkSide-20k cryogenics system parameters.

1050

6.2. Cryogenics

1051 The main system parameters of the cryogenics system are given in Table III. The parameters
 1052 that are listed in bold are considered to be system requirements, most often driven from experience
 1053 gained during operations of the DS-50 cryogenics system.

1054 The cryogenics system is derived from the successful scheme of the DS-50 cryogenics and gas
 1055 handling system. Additional lab tests, already performed over the past 4 years, demonstrated
 1056 individual or integrated features required for the performance of the control system and the safety
 1057 of the large amount of UAr in the DarkSide-20k system. A full P&ID diagram is already developed
 1058 as shown in Figure 17. There are two major linked systems: one for the AAr in the veto shield
 1059 inside the ProtoDUNE cryostat and one for the UAr in the sealed acrylic vessel for the LAr TPC.
 1060 The AAr cryogenics system can be the same as the demonstrated ProtoDUNE system already
 1061 built at CERN, or an optimized version specific for the LNGS installation. The UAr cryogenics
 1062 system for the TPC will be an upgraded system based on DS-50. The ProtoDUNE cryostat is a
 1063 passively insulated system so that its thermal load is not subject to the availability of the electric
 1064 power. Liquid nitrogen is the primary cooling source of the entire cryogenics system. A minimum
 1065 storage of the liquid nitrogen is maintained such that the system will be protected during power
 1066 failure mode. A full scale version of the condenser box for the underground argon has already been
 1067 designed and all parts procured. The cryogenics test of the condenser is planned at the CERN
 1068 cryogenic division in summer 2019.

1069 Heat exchangers are strategically placed throughout the system for LAr filling and LAr removal at
 1070 the various required speeds for the different operational modes. The continuous argon circulation for

1071 purification is driven by a set of specialized gas argon pumps (developed within the collaboration).
1072 Combined with the integrated heat exchanger systems, the system can handle high circulation
1073 rates (10 000 std L/min AAr, and 1000 std L/min UAr) drawing either, or both, liquid and gas
1074 phase argon to effectively remove electronegative impurities. The designed P&ID system allows
1075 the use of SAES hot getter to effectively remove N₂, CO₂, and O₂. The total cooling power of the
1076 cryogenics system is designed to handle the total heat load from the power dissipated by the cold
1077 electronics operating inside the liquid argon volume.

1078 The cryogenics system for the LAr TPC in DS-20k shares the same principle as that fully demon-
1079 strated in DS-50, which has been running smoothly for five years. The long-term TPC pressure
1080 stability, an essential parameter for S2 resolution, has been achieved with incredible success, quan-
1081 tified as 0.023 psi RMS. A drift electron lifetime of \geq 5 ms has been achieved, resulting in an oxygen
1082 contamination in LAr of less than 0.01 ppb, which is greatly beneficial to the low-mass dark matter
1083 search, as recently published in [7, 8]. The immunity to total power failure (including UPS system
1084 failure), as tested in the commissioning phase and verified by a recent accident of total LNGS
1085 blackout, secures the safety of the entire LAr TPC, especially the valuable UAr.

1086 The features of the DS-50 cryogenics system are fully implemented into the DS-20k system, not
1087 only by simply scaling up the argon volume, but also upgrades based on experience and lessons
1088 learned. A major improvement is to increase the circulation speed to the required 1000 std L/min,
1089 to initially reach the purity requirement of LAr in a couple of turn-over times of 20 d. Another
1090 major improvement is to increase the cooling power needed to accommodate such a large circulation
1091 speed. A full-size prototype LAr condenser, the core component in the cryogenics system, has been
1092 built and tested at UCLA, and a cooling power of 2.2 kW (latent heat only) has been achieved,
1093 nearly twice that needed for the DS-20k UAr cooling requirement. The main components of the
1094 UAr cryogenics system condenser box have already arrived at CERN and are ready for welding and
1095 the first test to follow in summer 2019.

1096 The UAr cryogenics system is made up of several sub-systems (while the AAr system will be
1097 similar except at larger scale in volume and power, but with lower requirements on purity): the
1098 liquid argon handling system, the liquid nitrogen reserve system, the purification system, the cold
1099 box, the gas circulation pump, the recovery and storage system, the integrated heat exchanger
1100 system, and heat exchangers close to the TPC. The overall schematic is shown in Figure 17,
1101 including the AAr cryogenics system for the veto detector, which employs the same principle. Two
1102 cryogenics systems share the same liquid nitrogen reserve loop, but have separate argon loops of
1103 UAr and AAr, respectively. Also shown in the figure is the condenser box integrated with the heat
1104 exchangers and inline radon trap.

1105 The LAr handling system delivers the clean radon-free UAr, which is initially stored in the
1106 recovery storage system capable of storing the full target of UAr for DS-20k. Two options are
1107 being considered, full liquid phase storage or gas phase high-pressure storage. The gas handling
1108 system will be adopted to either solution in order to pre-purify the UAr before filling the TPC
1109 volume. The system is also designed such that the UAr can be recuperated from the inner detector
1110 to the recovery system, as needed, if an emergency occurs or at the end of the experiment.

1111 The LN₂ reserve system is a closed loop with a LN₂ plant located outside of Hall C and a few
1112 local liquid nitrogen dewars. The system delivers liquid nitrogen as the source of cooling power to
1113 the condensers in the inner detector UAr cryogenics system, the AAr cryogenics system, and the
1114 recovery system, if liquid phase storage is chosen, and recuperates the boiled-off nitrogen gas to
1115 liquify it back into the LN₂ system. The UAr purification system purifies the argon in gas phase
1116 during the circulation. A commercial SAES getter system has already been proven to work well in
1117 DS-50 and an identified model with increased circulation capability will be used in DS-20k.

1118 The cold box, as shown in Figure 18, is one of the key components of the DS-20k cryogenics
1119 system, which contains all the major cryogenic handling components. Apart from the condenser,
1120 the cold box contains five heat exchanger modules to efficiently pre-cool the argon gas by cold
1121 nitrogen gas and cold outgoing argon gas. In this way the necessary cooling power is reduced
1122 dramatically. The radon trap is placed between the coldest and the second coldest heat exchanger
1123 modules to ensure that the argon passing through is still in its gas phase, while at its lowest

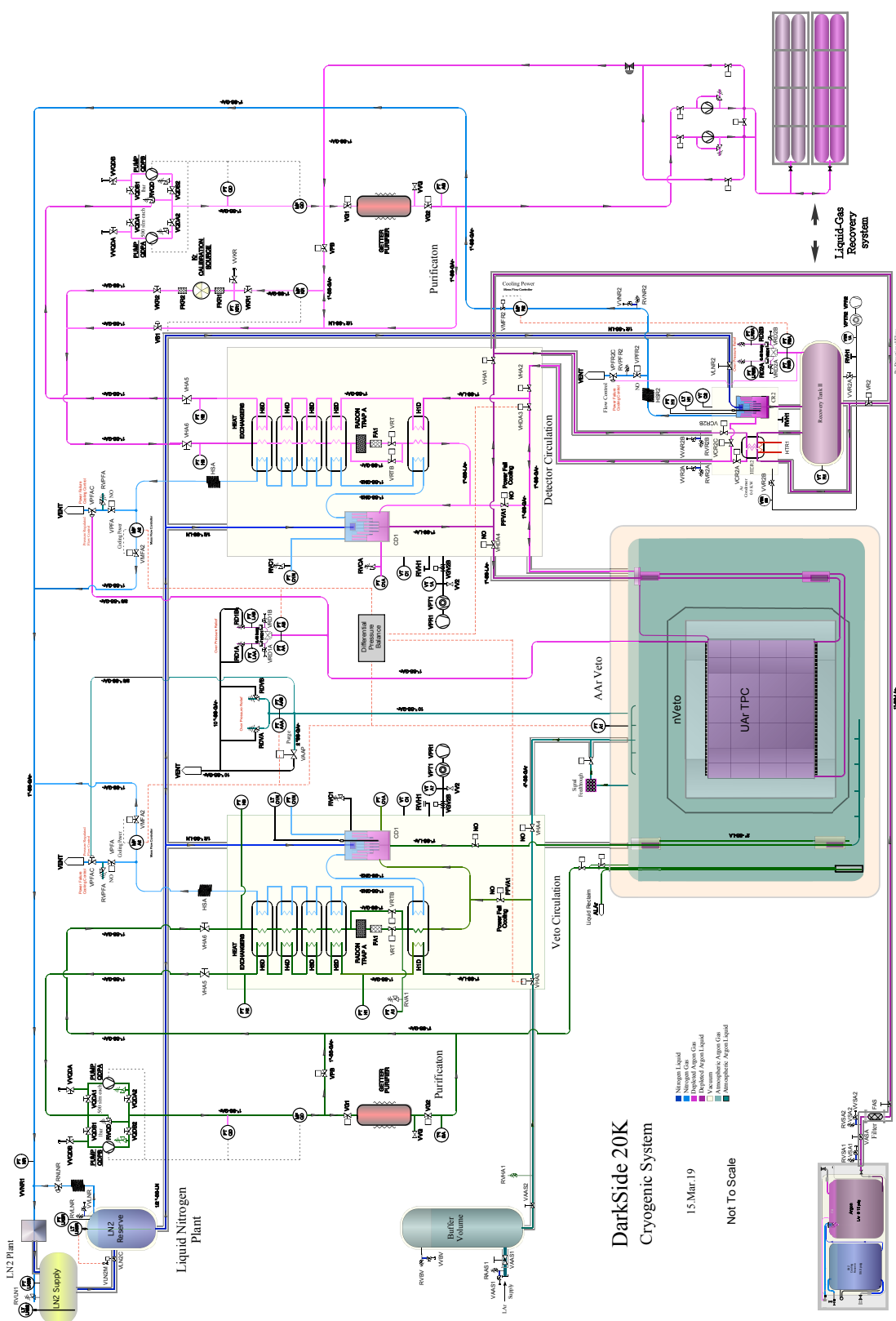


FIG. 17. DS-20k cryogenics system P&ID.

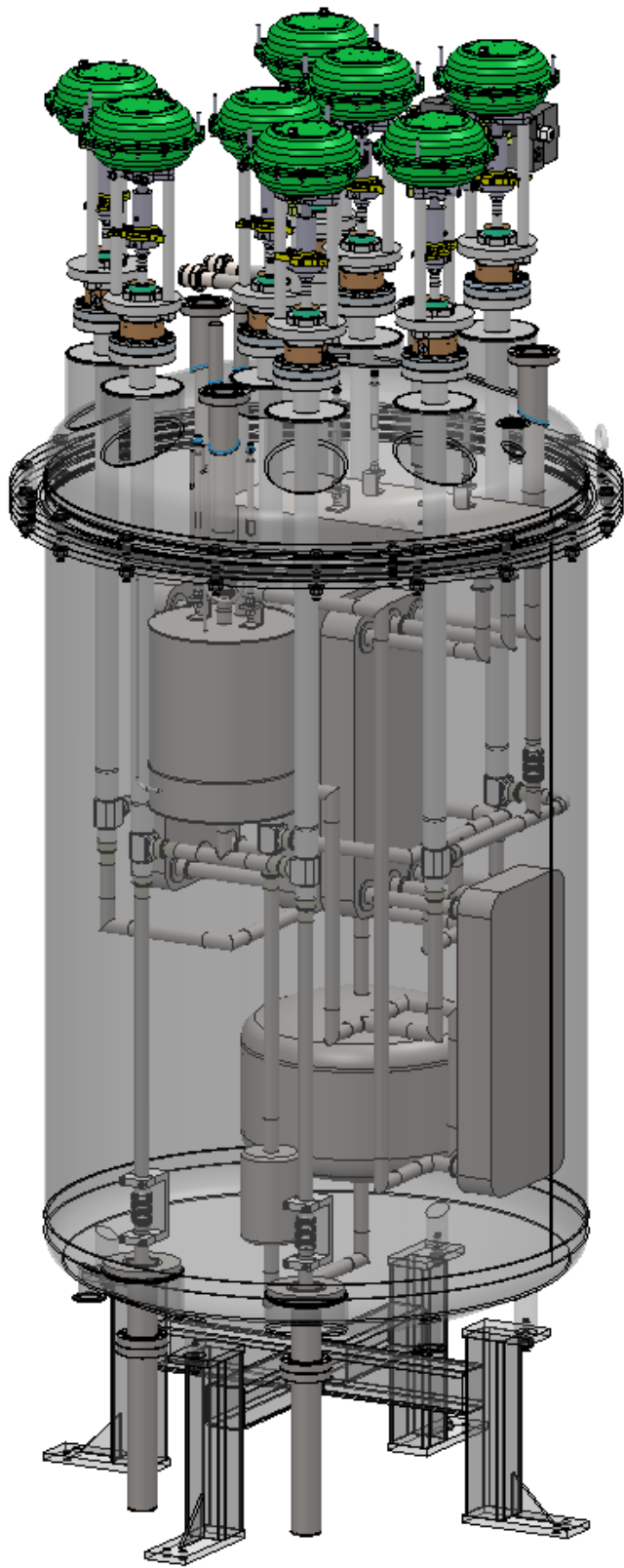


FIG. 18. DS-20k condenser box.

1124 temperature, which maximizes the radon removal efficiency. Eight cryogenic valves and several
1125 temperature and pressure sensors are also installed to control and monitor the system. Tubings
1126 are chosen as 1" OD stainless steel, in order to accommodate the argon circulation speed up to
1127 1000 std L/min.

1128 The stainless steel LAr condenser contains 127 0.5" OD top-sealed tubes finely patterned on a
1129 thick plate as the thermal exchanging part of the condenser. The condenser is therefore separated
1130 into the nitrogen volume on the top and the argon volume on the bottom. A so-called *chicken*
1131 *feeder* is mounted at the end of the liquid nitrogen delivery tube to maintain a continuous liquid
1132 nitrogen dropping. The flow of the evaporated nitrogen gas is monitored by a mass flow meter
1133 and adjusted by a control valve, both located at ambient temperature. The control valve uses
1134 the LAr TPC pressure from both UAr and AAr as feedback signal to automatically adjust the
1135 evaporated nitrogen gas flow rate, which is essentially the cooling power of the condenser, hence
1136 in return maintains the LAr TPC pressure at the desired set point and balanced with AAr system
1137 with an incredible stability, as demonstrated in DS-50.

1138 Based on the successful demonstration of the gas circulation pump in DS-50, which provides a
1139 speed up to 50 std L/min, the gas circulation pump of DS-20k uses the similar design, relying on two
1140 components: linear motors and reed valves. The linear motors, consisting of a piston and cylinder
1141 pair, can provide a continuously adjustable pumping power. The reed valves guide the gas flow
1142 direction when the linear motors going back and forth. Two balanced linear motors will be placed
1143 face to face, to counteract the vibration produced during the motor operation. The combination of
1144 the linear motors and the reed valve allows the pump to work in a frictionless condition, resulting
1145 in a long lifetime. The initial fast circulation requires a speed of 1000 std L/min to achieve a good
1146 UAr purity level, and then the circulation speed can be decreased to only maintain the purity
1147 and stability. This minimum flow could be very low since the UAr system essentially is embedded
1148 in the AAr system while all cold electronics are outside the UAr volume so no cooling power is
1149 required. To achieve such a high circulation speed, flexibility of operations, as well as the ease of
1150 the pump development, two individual circulation pumps will be placed in parallel, each providing
1151 a circulation rate up to 500 std L/min. A full-size prototype circulation pump has been fabricated
1152 at UCLA and Princeton, and passed the initial tests. It was shipped to CERN and is being certified
1153 for the EU safety requirement. Once fully tested, it will be integrated into the prototype cryogenics
1154 system for the full-system test.

1155 The heat exchangers close to the TPC are basically large heat exchangers using many tubes as
1156 the thermal exchanging parts, similar to the concept of the LAr condenser described above, but
1157 with a much increased thermal exchanging surface area. Outgoing LAr from the LAr TPC absorbs
1158 heat from the incoming liquid-gas mixture of purified argon here, boils off into gas phase, and then
1159 enters the circulation loop. This heat exchanger is located above the LAr TPC and ensures that all
1160 outgoing argon above it will be in gas phase, avoiding otherwise a large argon head height coming
1161 directly from the LAr TPC to the lowest heat exchanger modules in the cold box. This would
1162 result in an argon pressure below its triple point at some point in the argon loop and causing argon
1163 to freeze. Another set of near TPC heat exchangers are strategically placed close to bottom level
1164 of the UAr TPC for fast recovery during the draining stage. This lower level heat exchanger is
1165 completely passive during normal operations and only useful during the draining phase. The entire
1166 near TPC heat exchangers are immersed in LAr inside the ProtoDUNE cryostat, which serves as
1167 a thermal bath for them.

1168 The integration and tests of the full scale UAr cryogenics system at CERN is ongoing. The first
1169 pass FEA engineering has proven the design load is as anticipated and fabrication is officially ap-
1170 proved. All condenser box components, large pneumatic cryogenics valves and associated auxiliary
1171 components are on site at CERN for integration. The full scale cryogenics test of the DarkSide-20k
1172 UAr system will be performed over the summer of 2019.

1173

7. MATERIAL ASSAYS

1174 Trace radioactivity in detector materials can be a dominant background for the direct dark-
 1175 matter searches. In addition to this bulk contamination, a major source of background can be
 1176 caused by the cosmogenic activation of the materials and by the surface contamination (due to
 1177 radon diffusion and plate out of the radon daughters produced in the surrounding air). Beta and
 1178 alpha particles produced by the radionuclide decays can typically contribute to the background
 1179 only if the atom is in contact with the LAr target, while gammas and neutrons, the last ones from
 1180 spontaneous fission and (α, n) interactions, can produce background from more distant sites.

1181 A strategy for selecting the materials, as well as machining, storing, transporting and mounting
 1182 the detector components, is mandatory in order to control the backgrounds and to maximize the
 1183 physics reach of DS-20k. This will be accomplished by developing the “background budget” to
 1184 identify materials’ purity requirements. In addition to the assays on the raw purchased materials,
 1185 performed to identify the right technologies and compositions, we are developing cleaning and
 1186 handling procedures to meet radiopurity standards, and performing assays to validate processes for
 1187 the construction and commissioning of the detector and its components.

1188 In DS-20k this responsibility is delegated to the Materials and Assays Working Group (M&A WG),
 1189 a single Working Group within the collaboration, comprised of experts in each of the assay methods
 1190 and representatives from each institution that hosts assay capabilities. The group coordinates and
 1191 schedules the assays according to the pre-evaluated radiopurity requirements, the urgency, the
 1192 capacity of the available assaying resources and their queue.

1193 The goal is to assay and approve *all* materials or items selected to reside within the cryostat,
 1194 particularly by scrutinizing the entire ^{232}Th and ^{238}U decay chains. This calls for multiple assays
 1195 with multiple techniques for each sample, as different techniques are applicable to different sub-
 1196 chains of the ^{232}Th and ^{238}U decay chains. These results are combined with the (α, n) cross-sections,
 1197 calculated according to the chemical composition of the material in order to extract the neutron
 1198 yield expected in the detector.

1199

7.1. Radio-purity database

1200 The need for fast access to, and exchange of data between different Working Groups (WG) is
 1201 addressed by the DarkSide Materials Database (MDB). Information on the radioactive content of
 1202 materials to be used for DS-20k construction is stored therein, and is crucial for the comprehensive
 1203 estimation of the background budget for the experiment. The MDB contains all the relevant
 1204 information about samples: chemical composition, origin (production batch), data-sheets, pictures,
 1205 part of the detector where it will be placed, history of assays etc. This information is included in
 1206 the total background budget estimation and carefully evaluated. Rules for handling and cleaning of
 1207 samples, developed and verified during the screening process, are also stored in the database. Later,
 1208 during the detector construction and integration, reproducible results of the estimated internal
 1209 background may be expected upon application of the provided handling and cleaning procedures.

1210 The database helps to systematize the radioactive background budget estimation, material se-
 1211 lection and tracking, assay prioritization, and cleaning and handling methods. Additionally, the
 1212 database is also used to balance the workload and assay resources between numerous institutions
 1213 involved in the task by coupling assay needs with assay capabilities of members of the Materials
 1214 WG.

1215 The MDB structure reflects the flow of the material assay process, aiding material selection
 1216 and application during the construction phase of the experiment. The database consists of several
 1217 cross-related tables, holding information on the status of the assay requests, screening methods,
 1218 samples, assay results and people (institutions) involved (see Fig. 19). It also keeps track of the
 1219 queues in different facilities, and the history and the current status of any assay performed within
 1220 the M&A WG. A convenient web-based interface is provided for the users (see Fig. 20), dedicated
 1221 to: ease submission of new assay requests from other Working Groups; browse and report of the

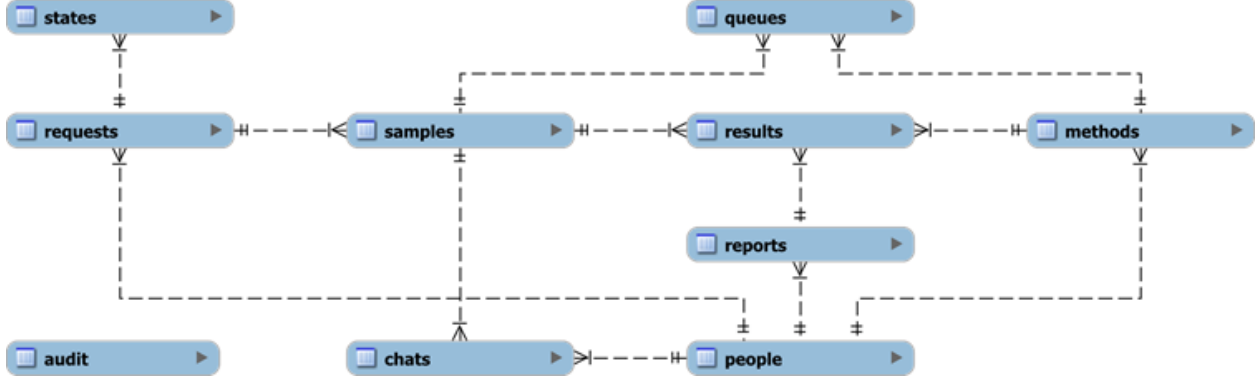


FIG. 19. A simplified DS-20k materials database structure. Information on each relevant aspect of the assay process is stored in the database, facilitating the management of the whole assay process.

Sample name											Description		Batch			DS-20 reference		Search ▾	
Show 25 entries											Copy CSV Hide empty Show all Column visibility ▾		Search: capa						
ID	Report	Name	Reference	Method	Sample	Date	^{60}Co	^{137}Cs	K	^{40}K	^{234m}Pa	Pb	^{210}Pb	^{210}Po	^{226}Ra				
1910	253	Capacitor 22pF	273 Non-satisfactory	PDM module	HPGe GeDSG (Matthias Laubenstein, LNGS, INFN),	complete 2018- 12-13	<6 [mBq/kg] (3 sigma)	<6 [mBq/kg] (3 sigma)		1.5±0.7 [Bq/kg] (1 sigma)	<1 [Bq/kg] (3 sigma)				<1 [Bq/kg] (3 sigma)				
36	5	Panasonic SMD capacitors	5 Decision pending	PDM module	HPGe GeCris (Matthias Laubenstein, LNGS, INFN),	complete 2017- 12-14	<2 [mBq/kg]	<4 [mBq/kg]		<1 [Bq/kg]	<2 [Bq/kg]				<6 [mBq/kg]				
1854	246	Panasonic capacitors	57 More assays needed	PDM module	HPGe BEGe (Matthias Laubenstein, LNGS, INFN),	complete 2018- 08-30	<7 [mBq/kg]	<5 [mBq/kg]		<2 [Bq/kg]	<7 [Bq/kg]				<0.2 [Bq/kg]				

FIG. 20. Interface web page, presenting a selection of assay results for various types of capacitors. The database is also used to manage the assay process of each sample.

assay results (including uploading the results); and to manage the assay status of the samples and queues at different facilities.

Assay results obtained for the materials used for DS-50 were also imported to the new database. Currently the database stores almost 2000 assay results (more than 120 assays performed since 2017) of nearly 300 samples, and counts (see Tab. IV). The M&A WG has established protocols to efficiently handle the radioactive budget of the experiment.

7.2. Managing Assay Capabilities

To ensure the radiopurity of all detector materials to the levels defined by the background model, the M&A WG has developed a radiopurity assay program that takes advantage of facilities throughout the collaboration. Overall, it is anticipated that this program will span approximately three years and will involve around a thousand more assays, including searches for radiopure materials, development and validation of cleaning and handling procedures, and screening of all detector components. The collaboration has extensive and diverse assay capabilities that are sufficient to complete this program on schedule, with extra capacity to handle additional unforeseen assays. Estimates of the capacity available to DS-20k for each assay type are summarized in Tab. V. The assay challenges are organized into six focus areas: mass spectrometry (ICP-MS), radon emanation,

Assay Method	Number of assays
ICP-MS	50
Germanium spectroscopy	40
Chemical extraction of Po	20
Surface α 's counting	5
Radon emanation	5
Other	3

TABLE IV. Summary of the assays performed since 2017 in preparations of the DS-20k construction, with breakdown by assay method.

Assay Method	Capacity [assays per year]
ICP-MS	60
Germanium spectroscopy	35
Chemical extraction of Po	20
Surface α 's counting	10
Radon emanation	10

TABLE V. Summary of the assay capabilities available for DS-20k.

1238 direct gamma assay (HPGe), surface assays (alpha activity), cosmogenic activation and materials
1239 handling and process development.

1240

7.3. Radioactive budget

1241 The radioactive budget states the expected background of everything that goes into the detector,
1242 taking into account material's (element) radiopurity, mass, composition, shape and location. These
1243 parameters are the input of Monte Carlo simulations, performed using a Geant4-based package
1244 written within the collaboration and called G4DS. The result of the simulation is the efficiency of our
1245 detector for rejecting the background coming from different sources, either because of geometrical
1246 reasons or because of active tagging of undesired events. The neutron budget is calculated on a
1247 single-element basis, so the mentioned inputs (radiopurity, composition and the position in the
1248 detector) are needed for every component of the detector.

1249 The most critical requirement in terms of radiopurity is given by the α activity, mainly caused
1250 by the naturally occurring radioactive chains of ^{232}Th and ^{238}U and potentially producing neutrons
1251 through (α, n) reactions. The cross section of this reaction is calculated using the *neucbot* program,
1252 where the energy spectrum of neutrons is generated as well. Hence, the (chemical) composition
1253 and construction of each component needs to be known with sufficient detail in order to calculate
1254 the interaction cross-sections correctly.

1255 Provided that some construction elements may be in similar locations, and that a component may
1256 be used in different places, a cross-linked, multi-tab spreadsheet is used to calculate the expected
1257 neutron budget. Propagation of any modifications or updates in a coherent way is easy to maintain.
1258 A summary of background budget components is tabulated in a user-friendly form, collecting all the
1259 relevant information structured following the same organization scheme as the Working Groups in
1260 the collaboration (Veto, TPC, PhotoElectronics, etc). M&A WG is in close cooperation with other
1261 WGs through dedicated group representatives, aiding selection of proper construction materials
1262 at the early stages of the design. The background budget is constantly evolving and converging
1263 as the material assay campaign progresses, such that more components' activities are determined.
1264 It is estimated that over 1000 more assays will be performed until the completion of the detector
1265 construction, for more than 150 expected material samples.

1266

8. CALIBRATION

1267 Calibrations for both the TPC and the Veto range from low-level detector issues, such as the
 1268 single-photoelectron response of individual photosensors, to high-level physics issues like the accep-
 1269 tance as a function of energy for nuclear recoils. The combination of radioactive sources, neutron
 1270 generators, and light sources ensures a robust calibration plan to reach ultimate science goals of
 1271 DS-20k.

1272

8.1. Distributed Gas Sources

1273 Full volume calibration of the TPC will be achieved with distributed gas sources: ^{83m}Kr and
 1274 ^{220}Rn . Gas sources are simple to implement, since they are added to the argon recirculation stream
 1275 and feature short halflives, quickly decaying out from the argon target volume. The monoenergetic
 1276 decays of ^{83m}Kr , distributed through the active volume of the TPC, can give a key calibration
 1277 point in the WIMP recoil energy region. The 3D reconstruction of events in the TPC allows a full
 1278 mapping of position-dependence of the light yield using the ^{83m}Kr source. This means that, while
 1279 broad dissemination through the active volume is important, a uniform distribution is not required.

1280 The ^{83m}Kr decays quickly ($\tau = 2.64\text{ h}$) to a stable nuclide and causes no long-term contamina-
 1281 tion or background to the WIMP search. The DS-20k ^{83m}Kr source is based on the source used
 1282 successfully in DS-50. A tiny droplet of a solution of ^{83}Rb ($\tau=124.4\text{ d}$) is adsorbed into a piece
 1283 of charcoal, which, after drying, is placed between two particulate filters in a branch of the argon
 1284 recirculation system which is normally isolated by valves and can separately be pumped to vacuum.
 1285 In DS-50, an initial 8.5 kBq of ^{83}Rb gave a ^{83m}Kr trigger rate of hundreds of Hz, even though the
 1286 flow subsequently passed through a cooled radon trap. In DS-20k, the challenge will be to get the
 1287 ^{83m}Kr broadly distributed in the 49.7 t active mass before it decays. To further this, LAr will be
 1288 returned to the TPC after repurification via numerous tubes whose endpoints will be distributed
 1289 over the surface area of the TPC side panels.

1290 ^{220}Rn and its short-lived daughters produce several γ -rays, β 's, and α 's of various energies,
 1291 making it an attractive distributed calibration source that can be implemented in a similar manner
 1292 as the ^{83m}Kr source, except fo the need to bypass the charcoal trap before insertion into the gas
 1293 stream. The source of ^{220}Rn may be prepared as an electroplated ^{228}Th on stainless steel or copper.
 1294 Enclosed in a small metal-sealed and vacuum-tight volume equipped with a VCR/CF port. The
 1295 advantages of the ^{220}Rn source are the following:

- 1296 • ^{220}Rn and its daughters are short-lived, the longest half-life in the chain is 10.6 h for ^{212}Bi ,
 1297 therefore the activity introduce into the detector will disappear after a few days;
- 1298 • The high energy alphas appearing in the chain (6.05 MeV, 6.09 MeV, 6.29 MeV, 6.78 MeV, and
 1299 8.78 MeV);
- 1300 • The coincident ^{220}Rn - ^{216}Po and ^{212}Bi - ^{212}Po decays will allow to study the homogeneity of the
 1301 distributed sources, and possible LAr flow patterns as well as potential “dead volumes” that are
 1302 not affected by the LAr circulation;
- 1303 • Drift of the charged ions inside the LAr volume (interesting also with respect to Po isotopes from
 1304 the ^{222}Rn chain);
- 1305 • Low-energy β 's appearing in the chain may be used for calibrations of the low-energy response
 1306 of the detector.

1307 To avoid removal of the ^{220}Rn source by the charcoal trap it should be bypassed during the
 1308 calibration run. Release of ^{220}Rn from the source should be done in a way that avoids contamination
 1309 of the detector with residual ^{224}Ra (half-life 3.6 d) or ^{228}Th (half-life 1.9 yr). A similar risk exists
 1310 for the ^{83m}Kr source, but has been thoroughly mitigated and never observed.

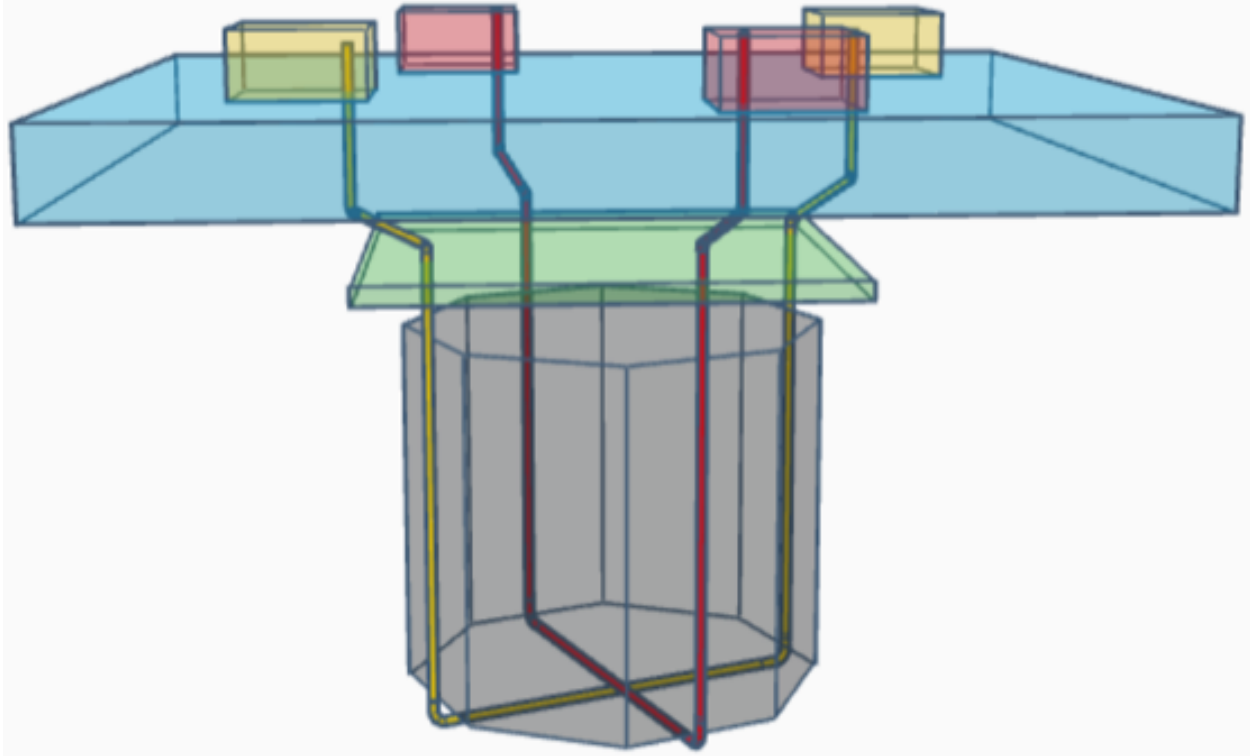


FIG. 21. Schematic representation of the system of guide tubes for insertion of sources.

1311

8.2. Gamma Sources

1312 Three external γ -ray sources, ^{60}Co , ^{133}Ba , and ^{137}Cs , are planned for use in the TPC calibration.
 1313 The combination of these sources in the absence of ^{39}Ar gives an excellent calibration of the electron
 1314 recoil PSD band, energy scale and provide valuable data for tuning of the detector response in the
 1315 Monte Carlo simulation. The γ -ray sources were chosen to span the energy range of interest in
 1316 combination with the distributed ^{83m}Kr source: 41.5 keV for ^{83m}Kr , 122 keV for ^{60}Co , 356 keV for
 1317 ^{133}Ba , and 662 keV for ^{137}Cs . Sources will be miniature in size to be inserted inside the source
 1318 guide tube for TPC, the overall design of which is shown in Figure 21.

1319

8.3. Neutron Sources

1320 Neutron sources are of particular interest for calibration of the nuclear recoil PSD band and
 1321 the efficiency of the neutron veto, a key feature of the DS-20k design. Small (α, n) sources such as
 1322 $^{241}\text{AmBe}$ and $^{241}\text{Am}^{13}\text{C}$ will be fabricated for this purpose. $^{241}\text{AmBe}$ is utilized as a tagged neutron
 1323 source utilizing 4.4 MeV gamma in 56 % cases. $^{241}\text{Am}^{13}\text{C}$ can serve as a gamma-free source for Veto
 1324 neutron calibration, after slowing down alphas for (α, n) reaction to always produce daughters in
 1325 the ground state. Sources will be small in size to be delivered with the source guide.

1326 While the $^{241}\text{Am}^{13}\text{C}$ source represents the best choice for calibration of the neutron detection
 1327 efficiency, interactions in the source holder and materials between the source and the TPC pro-
 1328 duced significant electron recoil background in the DS-50 TPC, problematic for characteriza-
 1329 tion of the nuclear recoils of argon nuclei. The $^{241}\text{AmBe}$ source was shown to be more suitable for this
 1330 calibration. The 4.4 MeV γ -ray is promptly emitted in the $^9\text{Be}(\alpha, n)^{12}\text{C}$ nuclear reaction in about
 1331 56 % of cases. By tagging the 4.4 MeV γ -ray in the Veto in a very tightly constrained time interval
 1332 prior to the signal in the TPC, a very pure sample of nuclear recoils is obtained. The $^{241}\text{AmBe}$
 1333 calibration in DS-50 provided the best available nuclear recoil calibration of the DS-50 TPC *in situ*,

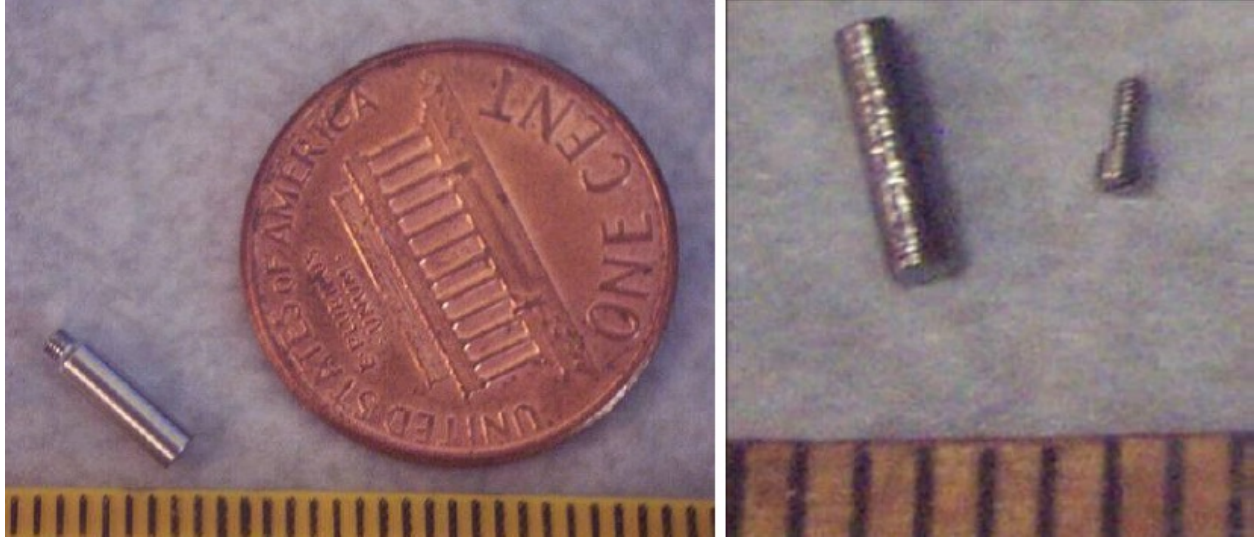


FIG. 22. **Left:** the outer capsule of the custom made $^{241}\text{AmBe}$ source from the Alabama group [58]. **Right:** the inner tungsten capsule of said $^{241}\text{AmBe}$ source.

1334 and was in excellent agreement with the nuclear recoil calibration from the stand-alone SCENE
 1335 experiment [33].

1336 The main novelty planned for the $^{241}\text{AmBe}$ calibration is a custom production of a miniature (a
 1337 few mm) $^{241}\text{AmBe}$ source, since the typically available commercial sources cannot fit within the
 1338 planned narrow guide tube system. The miniature $^{241}\text{AmBe}$ source will rely on the procedure de-
 1339 veloped by the neutrino group at the University of Alabama [58]. The group successfully fabricated
 1340 an $^{241}\text{AmBe}$ source with an outer capsule dimension of just 2 mm in diameter and 7 mm long, with
 1341 an activity of 50 neutrons per second using 1.9 MBq of ^{241}Am . Fig. 22 shows the outer and inner
 1342 source capsules. The inner capsule is made of tungsten to efficiently suppress the 4 MeV gamma
 1343 emission from the ^{241}Am . A very pure Be powder is mixed with ^{241}Am high purity powder in an
 1344 alcohol solution in a miniature test tube with a special micropipette and then transferred into the
 1345 tungsten capsule. After the alcohol evaporates, the procedure is repeated. In the end, the mixture
 1346 of $^{241}\text{AmBe}$ is compressed with a wire for higher source activity. The wire is also used to seal
 1347 the tungsten capsule. The tungsten capsule is placed inside the stainless steel capsule and welded
 1348 shut. The source is then ready for certification and use. The outside capsule has a threaded part
 1349 to attach the source to the rest of the calibration system.

1350 Photoneutron sources such as YBe emit nearly monoenergetic 157 keV neutrons, suitable for the
 1351 low energy end of the nuclear recoil band. However, such source requires 15 cm thick tungsten
 1352 shield to block copious γ -rays present in the source. Thus, this source is very bulky and requires
 1353 a separate deployment system. Deployments will be monitored via a camera system to avoid any
 1354 undesirable contact while operating in a delicate Veto.

1355

8.4. Guide Tube System

1356 Implementation of calibration sources is being finalized, following the completion of the designs of
 1357 the TPC the Veto, and the AAr cryostat. In parallel, plans are being developed for the calibration
 1358 needs of the DS-20k prototype detectors for x-y positioning, light yield and nuclear recoil calibration.
 1359 While work is still in progress, the overall schematic of how to guide radioactive sources from the
 1360 roof of the AAr cryostat, down around and inside of the Veto detector, and then back up to the
 1361 cryostat roof, is shown in Figure 21. The guide tube systems have been designed for simple, safe
 1362 and efficient calibration of the Veto and TPC using miniature radioactive sources. They will allow
 1363 deployment of the sources inside the Veto without direct contact with the argon, eliminating risks

1364 associated with it.

1365 The guide tube system will bring radioactive sources from the top of the AAr cryostat, to
1366 locations along the TPC exterior. The sources will be delivered through an enclosed stainless steel
1367 tube coming vertically down from the top of the cryostat, passing by the TPC PMMA vessel and
1368 around its bottom. The guide tubes will be 3 cm (1.18") in diameter to minimize shadowing, dead
1369 space and radioactive background coming from the stainless steel. The stainless steel tube segments
1370 will be connected with Swagelok connectors. In addition, relatively small tube diameter will help
1371 for tighter control of the source location, especially important in the case of the gamma sources.

1372 The miniature sources will be attached to the stainless steel guide wire that will be pushed with
1373 a wire driver powered by a stepper motor. A sleeve, made out of the PTFE tubing, will envelope
1374 the guide wire and the source to significantly reduce friction while the source and its guide wire are
1375 being pushed around. The wire driver will be equipped with a set of encoders and two sensor boxes
1376 for accurate positioning of the source. A pair of ring type inductive proximity sensors placed inside
1377 the sensor box will be used to reset the encoders when sources pass through a sensor at exactly
1378 known locations. The system will be purged with a low pressure nitrogen to eliminate any residual
1379 radioactivity that may have entered into the tubes.

1380 Except for the sensor box, all other parts of the guide tube system that require power, control
1381 and nitrogen flow will be at the top of the AAr cryostat. An elaborate testing program must be
1382 performed to ensure high quality and safety of the calibration when using the guide tube system.
1383 All parts will be radio-assayed and the entire system will be tested off-site for robustness, precision
1384 and reliability. Dedicated survey is planned to record the exact guide tube path around the TPC
1385 PMMA vessel.

1386 9. VETO DETECTOR

1387 9.1. Overall Design

1388 Benefiting from the implementation of a ProtoDUNE-like AAr cryostat, the Veto detector will
1389 utilize AAr as the scintillation material. The Veto detector is composed of three separate volumes;
1390 a passive octagonal acrylic shell loaded with gadolinium called the GdA and mounted around the
1391 TPC and providing $4 - \pi$ coverage, a 40 cm thick inner volume of active liquid AAr called the Inner
1392 Argon Buffer (IAB) and sandwiched between the TPC vessel and the GdA, a 40 cm thick outer
1393 active volume of AAr called the Outer Argon Buffer (OAB) contained between the GdA and the
1394 outer copper Faraday Cage. The Faraday Cage will contain the Veto and TPC and optically and
1395 electrically isolate them from the remaining outermost AAr volume contained within the cryostat.
1396 A schematic drawing of the Veto concept is shown in the left side of Figure 23, as well as a 3D
1397 cut-away drawing which presents the preliminary design.

1398 The required thickness of both the IAB and OAB of about 40 cm has been determined by MC
1399 simulation. The required thickness of the GdAS determined by the same simulation, is about 10 cm
1400 with a required Gd loading of 1 to 2 % by weight. The GdAS moderates neutrons emitted from all
1401 of the detector materials, particularly from the ones which make-up and surround the LAr TPC,
1402 while also enhancing the neutron capture probability with the inclusion of the Gd. The capture of
1403 the neutron on a Gd nucleus results in the emission of multiple γ -rays. These γ -rays interact in
1404 the IAB and OAB, their detection efficiency setting the required GdAS thickness and Gd loading
1405 fraction, as well as the minimum required IAB and OAB thickness. γ -rays are detected by use of
1406 scintillation light emitted by the liquefied AAr in both the IAB and OAB.

1407 Vertical segmentation of the IAB and OAB is foreseen to reduce the pile-up rate of ^{39}Ar events
1408 from the AAr. The concept of this is shown in the cut-away view of the detector in the right panel
1409 of Figure 23, while the exact details are still being optimized by use of the Monte Carlo simulation.
1410 SiPMs will be mounted on the sides of the GdAS such that they are facing both the IAB and OAB.
1411 The basic detector element is the same PDM used in the TPC, but with a different front-end board
1412 coupled to it that is optimized for the geometry of the Veto detector. Tests are in progress to

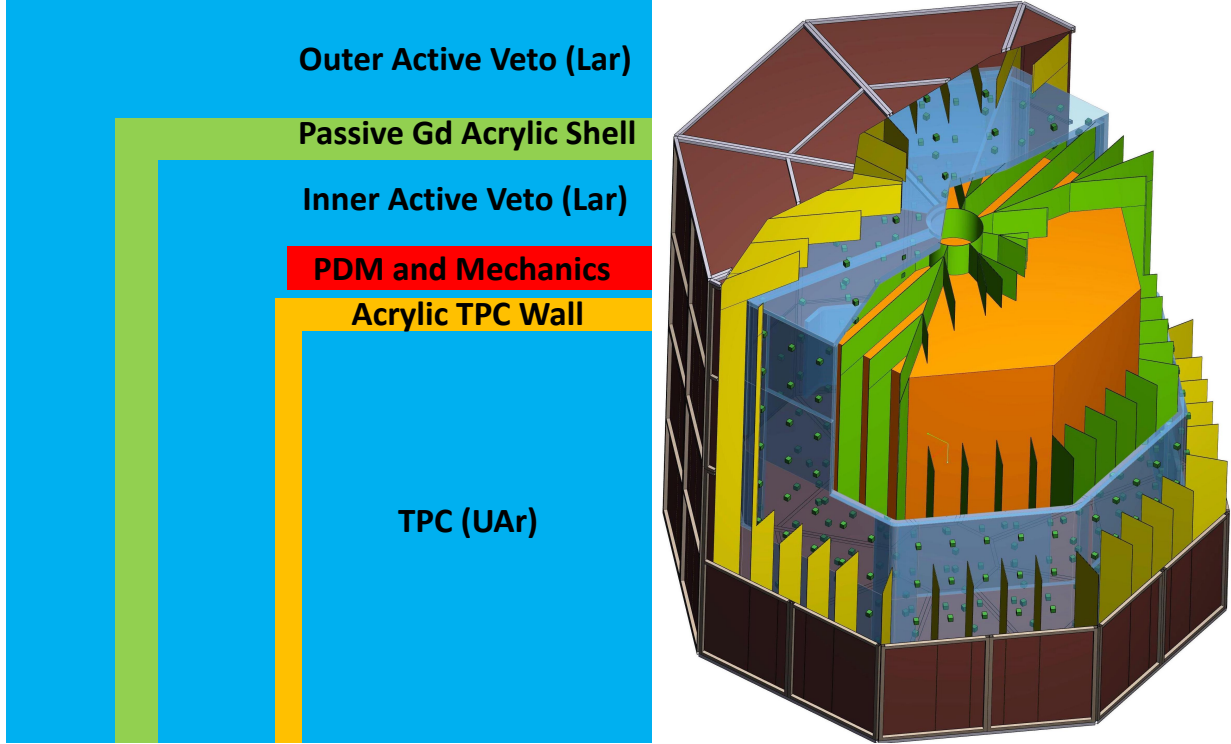


FIG. 23. **Left:** schematic conceptual view of the veto detector. **Right:** 3D cut-away view of the DS-20k veto detector.

1413 investigate the possibility of using an integrated electronics readout design for the Veto detector.

1414 All of the inner surfaces of the Veto, including the external walls of the TPC and the walls of the
 1415 vertical sectors, will be covered with reflector foils coated with wavelength shifter (TPB), so that
 1416 the VUV argon scintillation light is shifted to longer wavelengths where the LAr is very transparent.
 1417 This light is then trapped within a segment of the Veto detector by multiple reflections until it
 1418 reaches a SiPM. The optimal number of segments is being studied with the Monte Carlo simulation.
 1419 We expect no more than 5 segments for each edge of the octagon. The segments are not liquid tight
 1420 to allow flow of the argon through them, with a dedicated fluid-dynamics simulation planned to be
 1421 performed to ensure that the LAr can be properly re-circulated throughout the proposed geometry.

1422 The overall Veto detector design and the Monte Carlo simulation results will be validated using
 1423 smaller prototype setups. Due to the nested nature of the detector system, strategic planning for
 1424 the detector integration is also a big part of the development planning.

1425 This conceptual design promises to achieve the most important criteria for the DS-20k detector,
 1426 which is the efficient detection of neutrons such that no instrumental background interferes with
 1427 the potential nuclear recoil signal from a WIMP scattering off of an argon nucleus. The design
 1428 concept is scalable and lends well to serve as the basis for the future 400 t scale detector designed
 1429 to collect an exposure of 1000 t yr in absence of instrumental background. The Veto design is based
 1430 on elements which require no R&D and therefore can be built out of materials already available,
 1431 with the only exception being the gadolinium loaded acrylic. We have established good contacts
 1432 and an agreement with a company available to test in its laboratory techniques to mix gadolinium
 1433 compounds with liquid MMA before starting the polymerization process. Taking into account that
 1434 we do not need the final Gd-doped acrylic to be transparent to light (it acts only as passive neutron
 1435 moderator), and that the homogeneity of the mixture is also not a critical parameter, several known
 1436 difficulties related to metal loading into plastic scintillators are not an issue. After the success of
 1437 the small scale laboratory test done in 2018, the company who will likely provide the high-quality
 1438 acrylic for the JUNO experiment has agreed to produce samples of gadolinium loaded acrylic using
 1439 their industrial production line. Radio-purity tests will be performed on these samples once they

1440 are available.

1441 9.2. Assembly

1442 The assembly sequence starts with the mounting of the bottom part of the GdAS along with its
1443 PDMs. This component will rest on a stainless steel support structure (Veto support structure)
1444 that is itself supported by the cryostat floor via temporary feet. The TPC is then lowered into its
1445 place above the bottom of the Veto detector. Once in place, the TPC is mechanically connected
1446 to the support structure of the Veto through mounting pillars. This choice has been driven by the
1447 aim of reducing the mass of the support structure of the TPC and avoiding relative movements
1448 between the TPC and the VETO during construction, commissioning and detector operation.

1449 Once the TPC is fixed to the Veto support structure, the lateral panels of the GdAS and their
1450 PDMs are mounted. The vertical thin panels that divide the IAB into segments are then installed.
1451 The top GdAS panels are assembled next. Once the construction of the IAB is completed, PDMs are
1452 installed on the external surfaces of the GdAS and the panels which divide the OAB into segments
1453 are integrated. Then the copper frames that are used as the main structure of the Faraday cage
1454 are installed in the outermost part of the Veto. Finally the Veto detector is hanged from the
1455 cryostat roof using a dedicated support structure and several Kevlar ropes. One the Veto detector
1456 construction is completed, the temporary pillars used to support the Veto on the cryostat floor
1457 during the construction are removed.

1458 9.3. Background Rejection

1459 The combination of the signals occurring inside the IAB and OAB, within a given time window,
1460 is used to tag and reject neutron captures. If a neutron produces a signal in the TPC, it will mimic
1461 that of a WIMP signal, meaning that it produces a single energy deposit with energy in the range
1462 $30 \text{ keV}_{\text{nr}}$ to $200 \text{ keV}_{\text{nr}}$. This also includes fiducial volume cuts which exclude events occurring at a
1463 distance from the TPC walls less than 30 cm in the radial direction and less than 70 cm from the
1464 top and bottom. For events that pass this fiducialization, the Veto is then searched within a time
1465 window of 800 μs around the TPC trigger time. To minimize dead time losses due to β -decay from
1466 ^{39}Ar in the veto filled with AAr, a 800 keV threshold is set for each of the two parts of the Veto
1467 detector, while a lower 100 keV threshold is set for events with coincidence signals in both parts of
1468 the Veto detector.

1469 The design of the Veto and the choice of all the materials used to build the entire detector are
1470 set by the requirement of having less than <0.1 events untagged neutrons during the total exposure
1471 of 200 t yr. The radioactive contamination of the materials used to build the Veto is therefore also
1472 considered and limits are set by requiring that the corresponding neutron background induced in
1473 the TPC, after the implementation of all analysis cuts, is well below the above mentioned threshold
1474 of <0.1 events in 200 t yr.

1475 DS-20k is designed to operate with zero backgrounds, meaning that all sources of instrumental
1476 background are reduced to <0.1 events over a 200 t yr exposure. All background from minimum-
1477 ionizing radiation sources will be completely removed thanks to the combined action of PSD of the
1478 primary scintillation pulse and comparison of the primary and secondary scintillation (see Sec. 22.4
1479 for details on the suppression of background from pp scatters on electrons and Ref. [24] for that
1480 from ^{222}Rn , ^{220}Rn , and progenies).

1481 We focus here on the leading source of background, that is neutrons from the LAr TPC con-
1482 struction materials. We simulated the response of the LAr TPC, IAB, and OAB to (α, n) , which is
1483 expected to be the dominant contribution to the instrumental background budget. The geometry
1484 of the LAr TPC is that described in the rest of the document. The LAr TPC vessel is made of
1485 5 cm-thick PMMA, which helps to mitigate backgrounds by moderating the neutrons coming from

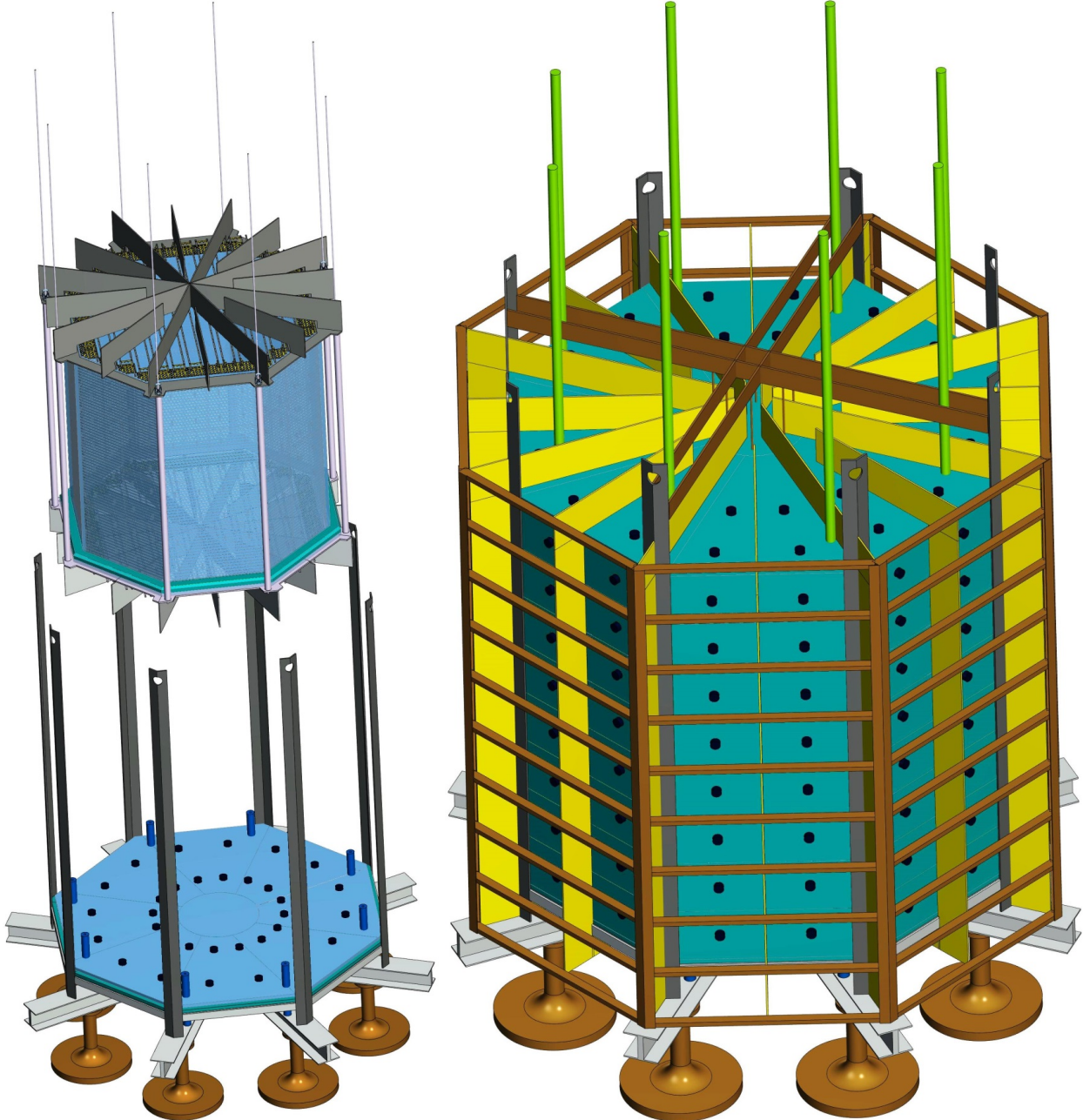


FIG. 24. **Right** Conceptual view of the placement of the TPC within the Veto support structure. **Left** 3D drawing of the DS-20k Veto detector, along with the temporary bottom support structure used for assembly and the Faraday cage.

1486 the detector's construction materials. For the PMMA, we assume the purity achieved in Ref. [42],
 1487 while for the Gd-loaded acrylic, we assume the purity of the scintillator of Ref. [59].

1488 The results of the Monte Carlo simulation are summarized in Table VI, where it is seen that the
 1489 final results meet the goal of <0.1 events in the full 200 t yr exposure. The two main sources of
 1490 contamination are the electronics of the SiPMs and the insulation of the cryostat. The collaboration
 1491 is now working to further improve the materials selection, which could reduce the expected neutron
 1492 flux coming from those components.

1493 The only remaining background for WIMP searches will be the signal from the coherent scattering
 1494 of atmospheric neutrinos on argon nuclei, with an expected 3.2 events over the 200 t yr exposure.

Material	Mass [tonne]	^{238}U [mBq/kg]	^{226}Ra [mBq/kg]	^{232}Th [mBq/kg]	Neutrons $[10\text{ yr}]^{-1}$	+TPC $[200\text{ t yr}]^{-1}$	+TPC+veto $[200\text{ t yr}]^{-1}$
TPC Vessel	2.7	1.2×10^{-2}	10	4.1×10^{-3}	1.1×10^3	0.17	1.7×10^{-2}
TPC SiPMs	0.12	-	-	-	1.1×10^4	0.16	1.6×10^{-2}
TPC Electronics	1.0	-	-	-	2.5×10^4	0.36	3.6×10^{-2}
TPC Mechanics	1.1	3.9	3.9	1.9	1.8×10^3	1.8×10^{-2}	2.0×10^{-3}
Veto SiPMs+elec.	0.40	-	-	-	1.3×10^4	0.10	1.0×10^{-2}
Veto Acrylic	13	1.2×10^{-2}	10	4.1×10^{-3}	5.2×10^3	4.2×10^{-2}	4.0×10^{-3}
Veto Reflectors	1.0	1.2×10^{-2}	1.0	4.1×10^{-3}	4.0×10^2	2.4×10^{-2}	2.0×10^{-3}
Veto Steel	1.1	3.9	3.9	1.9	1.8×10^3	1.4×10^{-2}	1.0×10^{-3}
$\text{Gd}_2(\text{SO}_4)_3$ α 's on self	0.26	7.0	7.0	0.2	2.1×10^2	2.0×10^{-3}	$<1.0 \times 10^{-3}$
$\text{Gd}_2(\text{SO}_4)_3$ α 's on PMMA	0.26	7.0	7.0	0.2	7.2×10^2	6.0×10^{-3}	1.0×10^{-3}
Copper Cage	1.0	0.30	0.30	2.0×10^{-2}	1.2×10^1	$<1.0 \times 10^{-3}$	$<1.0 \times 10^{-3}$
Cryostat Steel	250	50	1.0×10^3	3.9	1.0×10^6	-	$<1.0 \times 10^{-3}$
Cryostat Insulation	40	3×10^3	8.0×10^3	3.0×10^3	8.0×10^7	-	$<1.0 \times 10^{-3}$
Total						0.9	0.09

TABLE VI. Radiogenic neutrons sourced by the LAr TPC construction materials, veto and cryostat materials, with details of expected contamination levels, background after TPC cuts, and residual background after combined TPC and veto cuts, all relative to the full 10 yr run time and the full fiducial 200 t yr exposure. The number of expected neutrons is calculated from the expected contamination levels and material composition. Note that no specific activity is reported for the TPC SiPMs and associated electronics: in this case the predicted neutron yield is the results of an extremely detailed calculation, accounting for the cumulative contribution of several tens of components, individually assayed. The same consideration holds for the veto SiPMs and electronics, which contribution is reported in combination. For neutrons due to (α, n) reactions resulting from α 's originating from impurities in $\text{Gd}_2(\text{SO}_4)_3$, the contribution is broken down between those due to reactions on Gd sulfate itself and those due to reactions in the PMMA matrix containing the Gd sulfate; the mass fraction of Gd in the GdAS 1%, for the anticipated 2% concentration by mass of $\text{Gd}_2(\text{SO}_4)_3$. (For ease of conversion: 1 ppt(^{238}U) $\simeq 1.2 \times 10^{-2}$ mBq/kg; 1 ppt(^{232}Th) $\simeq 4.1 \times 10^{-3}$ mBq/kg.)

DS-20k will thus be the first experiment in a position to detect this important signal.

Surface contamination due to plate-out of radon on the surfaces is an additional source of background that can not be neglected. Radon is present in the outdoor air with a concentration of few to 10 Bq/m³, while inside buildings and in underground laboratories the concentration is typically higher (up to 120-150 Bq/m³). ^{210}Pb atoms accumulate on every surface of materials exposed to air and decay to ^{210}Bi that produces ^{210}Po . This is the potentially dangerous isotope because the α originating in its decay could produce neutrons. We estimate the concentration of ^{210}Pb adsorbed on an acrylic surface using data measured for polyethylene exposed to the SNOLAB air. We roughly expect a few tens of neutrons (before the analysis cuts) per day during the time which the entire surface of the acrylic is exposed to atmospheric air. This sets specific requirements for the cleanliness of the acrylic surfaces and on the mounting procedures of the Veto, which must be done in a radon free environment.

10. DATA ACQUISITION

The current design for the DS-20k electronics and its data acquisition system (DAQ) accommodates both the large number of sensors and the long drift-time (expected maximum electron drift time is 4 ms) of the LAr TPC, as well as the readout of the Veto detector. The trigger rate during normal dark matter search data taking has three major contributions: background events from detector materials, background events from ^{39}Ar , and random triggers. In order to estimate the first term, the event rate measured in the UAr exposures of DS-50 is taken, excluding the contribution from the PMTs and from the remaining ^{39}Ar in DS-50. This is scaled by the ratio of surface areas of DS-20k and DS-50, a factor of 55, obtaining an expected rate of 27 Hz. It is noted that these events will be concentrated at the surfaces of the active volume.

By using UAr and making the assumption of an ^{39}Ar reduction factor of 1400 with respect to

1518 AAr, there will still be an additional rate of about 16 Hz generated by ^{39}Ar decays, uniformly
1519 distributed throughout the active volume. In summary, events with correlated S1 and S2 signals
1520 are expected in DS-20k at a rate of about 50 Hz. On the other hand, the average singles rate per
1521 channel is dominated by the dark count rate (DCR) of the SiPMs. With the required 0.08 Hz/mm²
1522 specification, this will imply a singles rate per PDM of about 200 Hz. The event rate in the Veto
1523 detector, instead, will be dominated by ^{39}Ar decays in the instrumented AAr buffers.

1524 **10.1. General DAQ scheme**

1525 The baseline scheme for the TPC and Veto detector DAQ electronics hardware foresees an optical
1526 signal receiver feeding a differential signal to a flash ADC digitizer board that is connected to a large
1527 Field Programmable Gate Array (FPGA). The digital filtering capability within the digitizer board
1528 would allow the discrimination of single photoelectron signals and the determination of the time
1529 and charge of the individual channel pulses. For large and slow signals, such as the S2 ionization-
1530 born pulses in the TPC, the digitizer board would provide a downsampled waveform matching the
1531 expected signal bandwidth of a few MHz.

1532 The combination of the data processing will provide the needed data reduction to allow trigger-
1533 less operation of the readout for the TPC. Data from the Veto and TPC detectors will be transferred
1534 to the front-end data processing units where further data reduction will be performed. Finally the
1535 data will be passed to an online event building processor that will select interesting events and
1536 write them to permanent storage.

1537 In normal data taking mode, an event could be identified by a coincidence of hits in the TPC
1538 within a specified time window. A coincidence of 7 hits in 200 ns would result in a random trigger
1539 rate well below 0.1 Hz. Nuclear recoil events at the trigger threshold, producing about 15 PE in
1540 5 μs , would result in the collection of 6 PE to 8 PE within the first 200 ns. Thus, the trigger would
1541 be 100 % efficient for the WIMP-like signals of interest.

1542 The event building and software trigger stage is realized with modern commodity CPUs and
1543 connected through fast ethernet with the front-end DAQ processors. Given the low expected rate,
1544 the trigger-less option is foreseen to be feasible to implement. The expected combined event size
1545 for the TPC and Veto detectors is projected to be well below 1 MB.

1546 Synchronization between the TPC and Veto DAQ is fundamental for the effectiveness of the
1547 design, and will be provided and maintained during the data taking. The clock source of the TPC
1548 DAQ will be used as reference and digital signals (like GPS time stamps or trigger IDs) will be
1549 generated to uniquely identify each event regardless of the trigger origin or the detector. A pulsed
1550 signal distributed to all the modules will be used to check and correct the alignment of each channel
1551 among the TPC and Veto detectors.

1552 The DAQ system will be located in an electronics room which will be placed on the roof of the
1553 AAr cryostat. The environment will allow personnel access while minimizing the length of the
1554 optical fibers used to transmit the data from the TPC to the signal receivers.

1555 **10.2. Digitizers**

1556 The basic readout element of the proposed DS-20k DAQ system is a multi-channel board hosting
1557 several fast ADCs linked to a large FPGA for digital signal processing. This will be connected
1558 to a host CPU for control, monitoring and data formatting using as an output channel through
1559 a 1 Gbit/s to 10 Gbit/s ethernet connection to an external computer. The ADC will have 14 bits
1560 resolution and 125 MHz sampling speed. The board will accommodate one octal fADC chip for
1561 each of the 8 mezzanine boards, allowing it to handle 64 channels in total with a single board with
1562 a VME64 6U form factor. Data from the ADCs will be sent using high bandwidth JESD interface
1563 directly to a large FPGA. The board will host a Xilinx made Zync Ultrascale+ with a quad-core
1564 ARM Cortex A53 processor. Recent progress on this development includes the full implementation

1565 of the JESD interface and the ability to output data at the maximum specified speed. Specialized
1566 firmware is to be provided by the collaboration for noise filtering, basic data formatting and zero
1567 suppression to be implemented in the FPGA.

1568 The development of this electronics board is an ongoing partnership between the CAEN Company
1569 from Viareggio, Italy, which was selected as the provider of the electronics by the INFN, and the
1570 collaboration. The basic layout of the boards and the components that will comprise them have
1571 been selected and the first prototype will be available for testing in the summer of 2019. In the
1572 meantime, work in close cooperation between the GADMC and the CAEN firmware experts is
1573 ongoing to implement the needed signal filtering algorithms. In parallel, a DAQ system for the
1574 initial prototype TPC tests has been deployed at CERN in order to acquire data from up to two
1575 PDM Motherboards, amounting to 50 PDM channels.

1576 10.3. DAQ software

1577 The Maximum Integrated Data Acquisition System (MIDAS) has been chosen as a framework
1578 for developing the DAQ readout and related online control software for the DS-20k detector. The
1579 MIDAS DAQ package has been used extensively within the DEAP-3600 experiment, and together
1580 with the CAEN hardware provides a nice baseline for the digitization and recording of the raw data.
1581 A collaboration between the MIDAS and CAEN developers has been established to ensure that the
1582 interfacing of the front-end hardware is compatible with the back-end hardware and software that
1583 will ultimately compile and write the data to permanent storage.

1584 MIDAS is also well suited for handling the DAQ of the DS-Proto, for which, at least in the first
1585 stage, has a readout strategy and hardware implementation similar to those used in the DEAP-3600
1586 experiment. The DEAP-3600 hardware is mainly composed of 32xVME-V1720 and 4xVME-V1740
1587 using the proprietary CAEN CONET2 optical link to 5 different computers, providing optimum
1588 individual link data throughput using the A3818C PCIe interface. The DS-Proto readout will be,
1589 in the first phase, based on 5 CAEN VME-V1725 and a custom trigger module developed by the
1590 TRIUMF group. This system has been already installed at CERN in the first part of 2019 in order
1591 to provide the DAQ system for the first 50 channels (2 motherboards) of DS-Proto. In a later
1592 stage, the readout for DS-Proto will be based on the new digitizer boards from CAEN, previously
1593 described. Work has started toward designing an evolution of the MIDAS software to accommodate
1594 the new hardware boards and provide the needed event building and software trigger capability.

1595 11. COMPUTING

1596 The data storage and offline processing system must support transfer, storage, and analysis of
1597 the data recorded by the DAQ system, for the entire lifespan of the experiment. It must provide for
1598 production and distribution of simulated data, access to conditions and calibration information and
1599 other non-event data, and provide resources for the physics analysis activities of the collaboration.
1600 Necessary components for data storage and offline systems are the software framework and services,
1601 as well as the data management system, user-support services, and the world-wide data access and
1602 analysis job-submission system. The design of the system is built upon the knowledge acquired in
1603 the construction and operations of the DS-50 detector.

1604 The large number of channels in the LAr TPC makes it impractical to digitize and save the full
1605 waveform of each channel, as done in DS-50. Nevertheless, the charge and hit time information
1606 that will be saved will preserve all the necessary details about the amplitude and time evolution
1607 of the signals generated in the target. With appropriate filtering and compression, in addition
1608 to the expected background reduction described elsewhere in this document, the amount of data
1609 selected for recording in DS-20k is expected to be only a few times that of DS-50. The DS-50
1610 experiment typically collects about 9×10^5 events/d, of which 8×10^5 events/d come from laser
1611 calibrations, with the remaining 1×10^5 events/d from the dark matter search. The size of a DS-50

laser calibration event is about 0.1 MB, while the size of a dark matter search data event is about 2.6 MB. This is expected to decrease by a factor of 3 to 4 in DS-20k, despite the much larger number of channels. Taking into account the event size and data rate, the improved background rejection and data filtering, and using the experience from DS-50, the short-term storage required at the experimental site is expected to be 20 TB. The total storage inventory required for the experiment is expected to be more than 20 PB, including the storage needed for simulated and reconstructed events.

11.1. Computing systems and data workflow

The primary event processing will occur at the experimental site in the software trigger farm. Pre-processed data is archived on the temporary storage at the experimental site and copied to central computing centers (Tier-1/Tier-2). These facilities archive the pre-processed data, provide the reprocessing capacity, provide access to the various processed versions, and allow analysis of the processed data. Derived datasets produced in the physics analyses are also copied to the Tier-1/Tier-2 facilities for further analysis and long-term storage. The Tier-1/Tier-2 facilities also provide the simulation capacity for the DS-20k experiment.

Bulk data processing is expected to be performed using low cost commodity cluster computing based on commercial CPUs. Final data analysis will be performed either directly at the Tier-1/Tier-2 centers or on commercial CPUs hosted at institutes participating in the experiment. There is also the option of using the considerable free resources available on the Open Source Grid, which many experiments are currently using to run their reconstruction and analysis jobs.

The amount of short term storage currently available at LNGS for DS-50 consist of 7 TB of front-end storage used as temporary buffer and located in the underground laboratory, plus 710 TB of disk space in the above ground computing center for short- and long-term storage of DS-50 data. From there, raw data are copied to CNAF and Fermilab for reprocessing and analysis. CNAF is making available 1 PB of disk storage and 300 TB of tape storage. At Fermilab, there is 50 TB of fault-tolerant disk storage and about 620 TB on the dCache-based tape system for long-term storage. It is expected that much of this inventory will be recycled for the DS-20k experiment, aside from what is necessary for ongoing storage of DS-50 raw data. Any necessary additional tape storage will be purchased and installed. The total amount of storage for the ten years of data-taking, including calibration and simulated data, is 20 PB of disk storage and 20 PB of tape storage. The processing power currently used for reprocessing and analysis of DarkSide-50 data includes a farm of 400 cores at LNGS for production and validation, plus 400 job queues at CNAF and 25 guaranteed batch slots (soon to increase to 60 guaranteed batch slots) on the Fermilab grid system.

Currently, a single DS-50 event takes about a half of a second to reconstruct on a typical 2.8 GHz processor, meaning that 100 dedicated cores can maintain reconstruction in realtime for an event rate up to 200 Hz. Assuming a factor two increase in the cpu time needed to reconstruct an event, a factor ten to simulate a full event, a real data plus calibration event rate of 100 Hz, and a sample of simulated events of the same dimension of the real-data one, DS-20k needs 100 dedicated cores to maintain reconstruction in realtime of the collected real data + calibration events, and 1000 dedicated cores to produce the simulated samples. Moreover, 2000 physical cores are sufficient to reprocess all physics events collected in one year in a three month time period.

11.2. Software Environment

DS-20k will adopt an object-oriented approach to software, based primarily on the C++ programming language, with some components implemented using other high level languages (Python etc.). A software framework has been built up during the DS-50 experiment which provides flexibility in meeting the basic processing needs of the experiment, as well as in responding to changing

1659 requirements. In order to support code reuse, build a system optimized for both the offline and
1660 software trigger environment, and provide common user access to low-level algorithms used for I/O
1661 and data persistency, the C++ code will make heavy use of object oriented abstract interfaces
1662 techniques.

1663 The reconstruction combines information from the TPC and the veto detectors. A typical recon-
1664 struction algorithm takes one or more collections of information from the event data model (EDM)
1665 raw data stream as input, calls a set of modular tools, and outputs one or more collections of recon-
1666 structed objects. Common tools are shared between reconstruction algorithms, exploiting abstract
1667 interfaces to reduce dependencies. Analysis of calibration data will also be performed within the
1668 reconstruction and simulation software environment.

1669 DS-20k will produce roughly 2 PB of data annually, combining the data processing, simulation,
1670 calibration, and distributed analysis activities. A data storage and management infrastructure is
1671 necessary to allow efficient storage and access to all this data. Two types of data storage are
1672 foreseen. The first is a file-based data and the second is relational-database-resident data. File
1673 storage is used for bulky items such as event data (physics data, calibration data and simulation
1674 data). Database storage is used for other types of information, including technical data like detector
1675 production, installation, survey and geometry data, online/TDAQ databases, conditions databases
1676 (online and offline), offline processing configuration and bookkeeping information, and to support
1677 distributed data and database management services. File-based storage of C++ objects will be
1678 implemented through the use of ROOT I/O, which provides high performance and highly scalable
1679 object serialization to random-access files. Database storage will be based on SQL-based relational
1680 databases (MySQL and SQLite). All these technologies are widely used and well tested in HEP
1681 experiments.

1682 Computing resources will be accessed through Grid middleware components and services. These
1683 provide services for software installation and publication, production operations, and data access
1684 for analysis through a uniform security and authorization infrastructure, as well as interfaces for
1685 remote job submission and data retrieval, and job scheduling tools designed to optimize utilization
1686 of computing resources. The Grid infrastructure will be based on the infrastructure and the software
1687 tools and services developed for the LHC Computing Grid (LCG) project.

1688 The High-Level Software Trigger (HLST) provides the online event selection. The trigger is
1689 based on an online version of the DS-50 reconstruction software, which has been optimized and
1690 tailored for the DS-20k online environment running on farms of Linux PCs and/or GPUs farms.
1691 Overall, the HLST has to provide the required rate reduction and pre-processing of raw data,
1692 including the production of global event records in analysis EDM format. The HLST will use
1693 the offline computing environment, allowing DS-20k considerable commonality in the design and
1694 management of the selection software itself. This also allows the HLST to use various offline
1695 software components, like detector description, calibrations, EDM, and reconstruction algorithms.
1696 The same infrastructure can be used for data monitoring by simply replacing or augmenting the
1697 selection algorithms with those for monitoring.

1698

11.3. Simulation

1699 G4DS is a Geant4-based simulation toolkit specifically developed for DarkSide. The modular
1700 architecture of the code was developed in order to describe the energy and time responses of
1701 all the detectors belonging to the DarkSide program, namely DS-10, DS-50, and DS-20k, but
1702 other variations of the geometries as well. For each of them, G4DS provides a rich set of particle
1703 generators, detailed geometries, real data tuned physical processes, and the full optical propagation
1704 of the photons produced by scintillation in liquid argon and by electroluminescence in gaseous argon.
1705 The main goals of G4DS are to accurately describe the light response, calibrate the energy responses
1706 in S1 and S2 and the time response expressed by the f_{90} variable, tuning of the analysis cuts and
1707 their efficiency estimation, prediction of the electron and nuclear recoil backgrounds, and definition
1708 of the signal acceptance band.

1709 G4DS tracks photons up to their conversion to photoelectrons, which occurs when a photon
1710 reaches the active region of a photosensor and survives according to the quantum efficiency. The
1711 conversion of the photoelectron into a charge signal is handled by the electronic simulation, an
1712 independent, custom-made C++ code. The electronic simulation embeds all the effects induced
1713 by the photosensors (e.g. after-pulse and cross talk) and by the electronics itself (e.g. saturation).
1714 The electronic simulation also has the option to overlap simulated events and real data baselines
1715 in order to provide more realistic simulations. As output, it produces waveforms for each channel
1716 with the same data format of the real data, in order to be processed by the same reconstruction
1717 code.

1718 G4DS can also track events generated by FLUKA and TALYS simulation codes, previously
1719 developed within the collaboration. The FLUKA simulation is mostly used to study cosmogenic
1720 neutrons and isotope productions, while TALYS is used for (alpha,n) reactions, both providing
1721 input for the prediction of the nuclear recoil background.

1722 12. THE ReD EXPERIMENT

1723 The ReD project aims to characterize the light and charge response of the LAr TPC to neutron-
1724 induced nuclear recoils, especially at low energy, and to explore for the possible directional de-
1725 pendence suggested by the SCENE experiment [33, 34]. ReD encompasses the irradiation of a
1726 miniaturized LAr TPC with a neutron beam at the INFN, Laboratori Nazionali del Sud (LNS),
1727 Catania. Neutrons are produced via the reaction p(⁷Li,⁷Be) from a primary ⁷Li beam delivered
1728 by the TANDEM accelerator of LNS. A $\Delta E/E$ telescope, made by two Si detectors, identifies
1729 the charged particles (⁷Be) which accompany the neutrons emitted towards the TPC. Neutrons
1730 scattered from the TPC are detected by using an array of nine 3" liquid scintillator (LSci) detec-
1731 tors, using EJ309 liquid scintillator coupled to ET 9821B PMTs. The Si telescope and the TPC
1732 are not at the same height: this is mandatory in order to tag neutron scatterings (n,n') from a
1733 non-horizontal interaction plane. All LSci are placed such to tag recoils having the same energy,
1734 i.e. the same scattering angle with respect to the incident neutron, but different angle with re-
1735 spect to the drift field of the LAr TPC, thus allowing to search for a possible directional response.
1736 Thanks to the support provided by INFN CSN2, the entire set-up has been procured, integrated,
1737 commissioned and deployed to the "80 deg" beamline of LNS. The first beam run test took place
1738 in June-July, 2018.

1739 The core detector of ReD is a custom-made TPC designed by UCLA, which is a miniaturized
1740 version of the LAr TPC for DS-20k. The TPC is a cube with size of about 50 mm. An acrylic vessel
1741 defines the active volume, with the top and bottom acrylic windows ITO coated to allow for the
1742 application of the electric field, and the side ESR-acrylic sandwich reflection panels to maximize
1743 the reflectivity of the chamber. All of the internal surfaces are coated with TPB to wavelength
1744 shift the argon scintillation light. The drift field is kept uniform along the drift coordinate by
1745 means of the field shaping rings, deposited by thin-coating the walls of the acrylic vessel with
1746 ITO. The drift length, extraction length and electroluminescence length of the ReD TPC are
1747 5 cm, 3 mm and 7 mm, respectively. The ReD TPC uses all the innovative features of the DS-20k
1748 design, in particular the optoelectronic readout based on SiPM developed by FBK and the cryogenic
1749 electronics. Two 5x5 cm² tiles are available from FBK, each made by 24 rectangular SiPMs. The
1750 tile on the top of the LAr TPC has a 24-channel readout, in order to improve the (x,y) sensitivity,
1751 while the bottom tile has a standard 4-channel readout. A dedicated 24-channel Front End Board
1752 (FEB) has been designed and produced by INFN-Na in collaboration with INFN-Bo and LNGS.

1753 The LAr TPC is contained in a new cryogenic system. The commissioning of the system was
1754 carried out in Naples. Starting from April 2018, the new TPC and cryogenic system were operated
1755 and tested. Measurements were taken with lasers, low-energy γ sources and neutrons from a
1756 DD generator. This allowed for the first characterization of the LAr TPC and for an integrated
1757 test of: operating procedures, photosensors, DAQ, slow control, data handling and reconstruction
1758 algorithms. The system was successfully operated in single and double phase modes, with a light

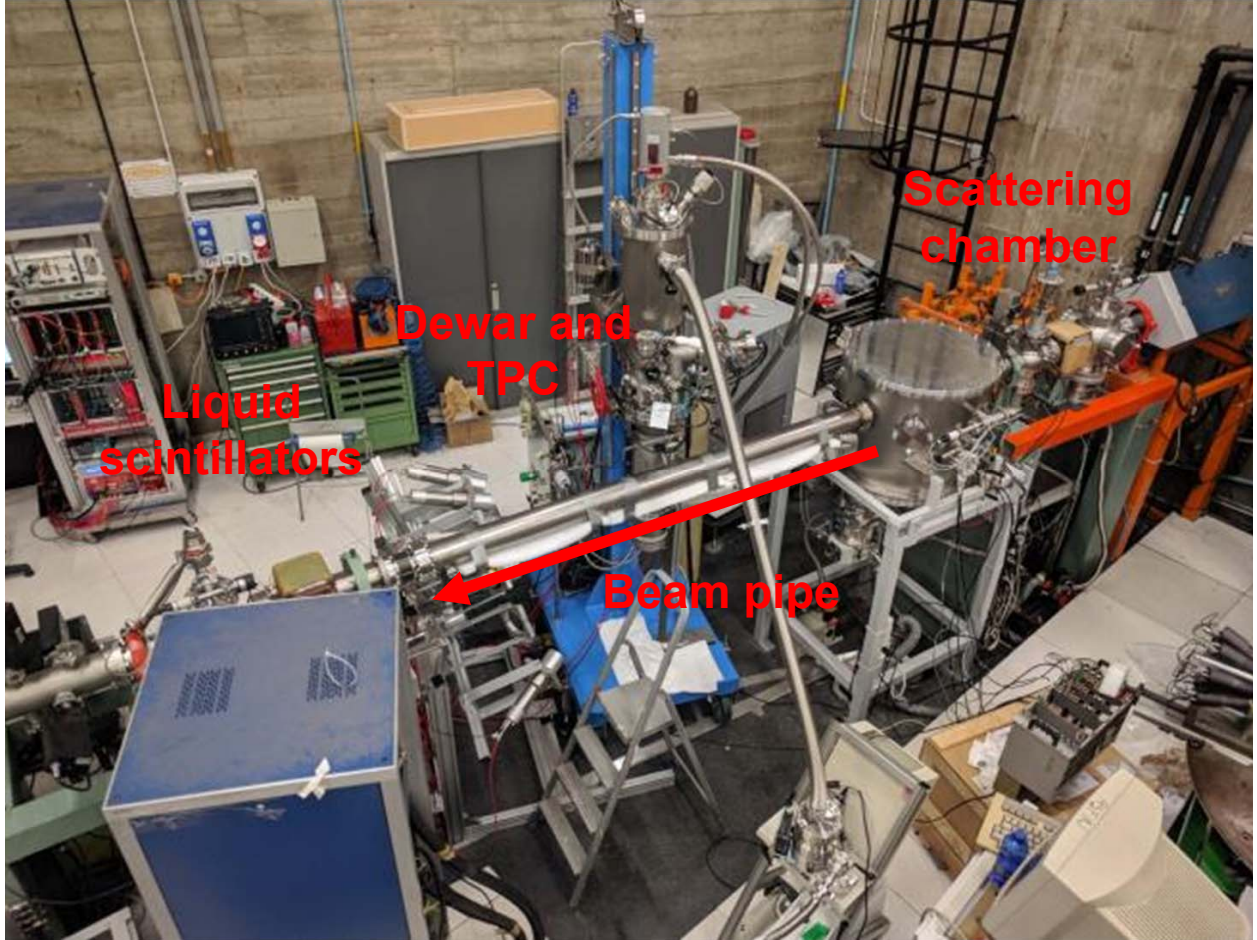


FIG. 25. Photo of the “80 deg” beamline at LNS, after the deployment and alignment of ReD. The targets and the Si telescope are hosted inside the vacuum scattering chamber.

yield of about 10 phe/keV at null field. The new LabVIEW-based slow control developed by INFN-Genova was also integrated and commissioned. The set-up was irradiated in Naples with the DD neutron gun from the Temple University, such to assess the PSD performance of the LAr TPC. The run also included one LSci, allowing for the first test of the DAQ for a system made by two different types of detectors. All nine LSci detectors had been previously tested and characterized at INFN-Roma1.

The commissioning and the characterization of the system in Naples opened the way for the deployment of the system at the beamline of LNS. The entire set-up (TPC with cryogenic system, liquid scintillators with their PMTs and the mechanical support structure) was shipped and re-assembled in Catania in June 2018. Meanwhile, the beamline had been refurbished on the basis of the experimental design, optimized with dedicated Monte Carlo simulations, and the mechanical clearance requirements. The configuration was conceived to allow the tagging of nuclear recoils between 20 and 100 keV traveling in the parallel and orthogonal directions with respect to the TPC drift field, by varying the primary beam energy only. Furthermore, having a dedicated liquid scintillator at small scattering angles opens the possibility to study the response of the TPC to very low-energy nuclear recoils, $O(1)$ keV. A new scattering chamber was installed with a new beam pipe. The $\Delta E/E$ telescope was installed inside the vacuum scattering chamber, commissioned and consists of two Si detector ($20\ \mu m$ and $200\ \mu m$ thickness, respectively) by ORTEC.

Initially, the cryostat and the liquid scintillators had to be mechanically aligned with respect to the target with a precision of the order of a few mm. The alignment was performed by following a detailed procedure worked out in advance. The ReD set up in Catania is displayed in Fig. 25.

1780 After the scientific approval of the project by the Scientific Committee (PAC) of LNS, a test beam
1781 run was scheduled in June-July 2018, meant for technical tests and commissioning. The individual
1782 detectors were first commissioned and tested individually, by using the laser and radioactive sources.
1783 Light yield and timing were checked by using ^{241}Am and ^{22}Na , respectively. A ^{252}Cf fission neutron
1784 source was used to characterize the pulse shape discrimination performance of both the LAr TPC
1785 and the LSci detectors. The light yield of the TPC was measured to be about 8.5 phe/keV, while
1786 the electron drift lifetime about 250 μs , i.e. much longer than the total drift time (about 40 μs at
1787 the operational field of 0.2 V/cm), with no hints of degradation in time. The calibration of the
1788 LSci detectors indicated a 50 % trigger efficiency at 20 keV_{ee} and a time resolution of 1.2 ns (rms),
1789 which is sufficient for the measurement of the time-of-flight.

1790 The integration of the three detector systems was done with the TANDEM beam. Neutrons were
1791 produced by sending a ^7Li 28 MeV beam onto a set of CH₂ targets having thickness between 150
1792 and 250 $\mu\text{g}/\text{cm}^2$. The intensity of the beam impinging on the target after the collimator, measured
1793 by the Faraday Cup installed at the far end of the beam pipe, ranged between 0.5 and 7 nA. The
1794 DAQ software handled 41 readout channels from three FADC boards (CAEN V1730), at 500 MHz
1795 sampling rate. A data-to-disk rate of 40 MB/s has been achieved. The Si telescope was placed at
1796 5 deg with respect to the beam. The scattering kinematics allows for two solutions with ^7Be in this
1797 direction, one having an associated 7.5 MeV neutron at 22.5 deg, the other with a 2 MeV neutron
1798 at 45 deg. The LAr TPC is at 22.5 deg from the target, i.e. it is hit by 7.5 MeV neutrons, produced
1799 in association with the ^7Be detected by the Si telescope. The beam energy and the scattering angles
1800 cause the experiment to select nuclear recoils in the TPC of approximately 70 keV.

1801 About 24 hours of data have been taken in the best operating conditions. Data has been taken in
1802 both single and double phase modes and with two different trigger schemes, i.e. “Si and TPC”, “Si
1803 and any PMT”. The latter scheme yields a large fraction of accidentals, due to the large singles rate
1804 of the PMTs (kHz), but it gives potential access to low-energy recoil in the TPC, which would fail
1805 to trigger the TPC (low S1, or S2 only). Those events can later be searched for offline in the data
1806 analysis. Typical trigger rates were between 0.1 and 0.7 Hz. Events were observed with the proper
1807 signature, i.e. a ^7Be nucleus detected by the telescope, a nuclear recoil in the LAr TPC and a
1808 neutron scattering in the liquid scintillators. Neutron-induced recoils events in the TPC and in the
1809 LSci detectors are clearly separated from γ signals, either physical or accidental, by means of pulse
1810 shape analysis. As expected, the time difference Δt between the pairs of detectors features a peak of
1811 physical coincidences, sitting on a plateau of accidentals. The scatter plot of the amplitudes of the
1812 ΔE and E Si detectors is displayed in the left side of Figure 26. It shows the ability of the telescope
1813 to discriminate the charged products of the beam-target reactions, i.e. the main ^7Li band due to
1814 elastic scattering and the two ^7Be loci corresponding to the two solutions allowed by kinematics.
1815 The right side of Figure 26 shows the same distribution (zoomed), with the black markers referring
1816 to the events having a coincident signals in the TPC. As expected, coincident events between Si
1817 and TPC are mostly associated to ^7Be locus from the “correct” kinematical solution.

1818 After another LNS test beam in September 2018, the ReD TPC has been transported back to
1819 Naples, to complete the characterization and re-commissioning in the lab there. Tests have been
1820 performed to characterize the basic TPC performance in terms of light yield, uniformity, electric
1821 field configuration and S2/S1 ratio in double phase. The system was calibrated with ordinary
1822 γ -sources and with an internal ^{83m}Kr source, which generates a uniform distribution of mono-
1823 energetic events. Activities are still ongoing to characterize the extraction and multiplication fields.
1824 A campaign was also carried out at LNS to measure the neutron detection efficiency of the liquid
1825 scintillators, using a fission ^{252}Cf source. A test beam for the characterization of the neutron beam
1826 is going to be performed at LNS in June 2019 and for this run only the Si detectors and the LSci
1827 detectors will be deployed.

1828 The ReD project has received scientific approval by the Scientific Committee of LNS (PAC) for
1829 a five-week beam allocation that is granted for 2019. Upon completion, the ReD LAr TPC will be
1830 transported back to Catania and a new beam run with the full setup will be scheduled.

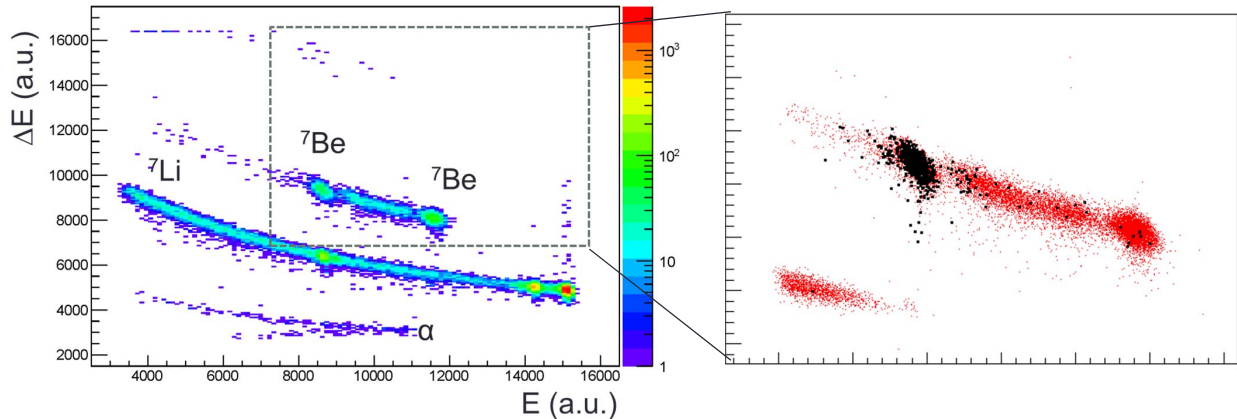


FIG. 26. **Left:** scatter plot of the amplitudes of the ΔE and E Si detectors, placed at 5 deg with respect to the beam axis. **Right:** zoom of the previous scatter plot in the region of the ${}^7\text{Be}$ loci; the black markers are events having a coincident signal in the TPC.

1831

13. DARKSIDE-PROTO

1832

13.1. Prototype Overview and Status

1833 The objective of the DS-Proto experiment is the construction and operation of a prototype de-
 1834 tector of intermediate size ($\sim 1\text{ t}$), to fully validate the new DS-20k technologies for their integrity in
 1835 both the mechanical and functional aspects. The prototype will be constructed using the materials
 1836 planned before screening, in order to speed up the mechanical validation, and will therefore not
 1837 necessarily be a physics-results oriented detector. This may evolve over time to include elements
 1838 of the detectors as materials are screened and made available, and eventually all parts could be
 1839 replaced with radio pure materials to form the basis of another experiment with high-sensitivity to
 1840 low-mass WIMPs. Thus, DS-Proto is not intended to replace validation and tests made in labora-
 1841 tories, but rather complement them with the integration with the rest of the detector. The prompt
 1842 execution of DS-Proto is crucial to fulfill the overall schedule of DS-20k. DS-Proto is on the critical
 1843 path of the project.

1844 The program for DS-Proto is expected to span over three different phases:

- 1845 1. Design, construction and assembly at test site of the LAr TPC, with the size available for two
 1846 motherboards integration;
- 1847 2. Integration of 50 preproduction PDMs to the LAr TPC; assembly, commissioning, and operation
 1848 of full read-out and DAQ for 50 PDMs; The xy resolution and S2 gas pocket optimization will
 1849 be done during this phase.
- 1850 3. Assembly and commissioning of full system, including 370 first production PDMs; full readout
 1851 and DAQ operational; evolution towards final configuration.

1852 The plan for DS-Proto was reviewed, approved, and funded by the CNS2 of INFN. Funding has
 1853 already been secured from the NSF for the development and fabrication of multiple components for
 1854 the TPC, the cryogenics system and resources for kick-starting the UAr extraction site preparations.
 1855 Requests for funding from other participating groups are being evaluated or will be submitted in
 1856 the near future.

1857 In August 2017 the collaboration and LNGS reached and finalized an agreement [60] with the
 1858 Accelerator & Technology Sector of CERN and its Technical Division to construct and commis-
 1859 sion the DS-20k cryogenics at CERN, with support from the Cryogenics Group and the Vacuum,
 1860 Surfaces and Coatings Group (both groups are part of CERN's Technical Division). The extension
 1861 of this program to carry out the first surface operation of DS-Proto at CERN before moving the
 1862 detector to LNGS was agreed by the CERN Accelerator & Technology Sector via an Addendum
 1863 to the above agreement. The necessary space and facilities are the same as for the test on the
 1864 DarkSide-20k cryogenics and are already allocated.



FIG. 27. The DS-Proto cryostat and components delivered at CERN.

1865 A cryostat for DS-Proto has been built by Tecno Alarm, s.r.l., Roma, and delivered to CERN in
 1866 August 2018 (see Figure 27). The 1 mBq/kg U/Th AISI 304 L Stainless Steel was procured from
 1867 NIIRONIT Edelstahlhandel GmbH & Co and it is good enough to be used for a possible physics
 1868 run in LNGS.

1869 Assembly and test of the DS-20k cryogenics will take place at CERN, during the summer and
 1870 last quarter of 2019. Construction of DS-Proto is expected at the end of 2019 or early 2020. The
 1871 first test operation with a reduced number of photosensors is expected by summer 2019, followed
 1872 by a second operation with a full complement of PDMs by early 2020. Full characterization of the
 1873 prototype performance and physics runs will be performed after installation at LNGS. The detailed
 1874 program of the activities to be carried out underground is under study.

1875 We anticipate that, since the DS-Proto will be a stand alone system, sharing the DS-20k cryo-
 1876 genics system at LNGS will not be possible. However over the past few years of R&D for the
 1877 DS-20k cryogenics, we have realized and tested several key components which will be more than
 1878 capable of handling the prototype system. These parts can be used for DS-Proto with minor system
 1879 integration together with most of the DS-50 and existing R&D devices.

1880

13.2. The DS-Proto TPC

1881 The DS-Proto TPC mechanics, including the structural elements, the field cage, the reflector cage,
 1882 the transparent cathode, the transparent anode (also serving as a diving bell for the containment
 1883 of the gaseous phase), the SiPM PDM assemblies, the high-voltage feed through system, will all be

1884 built utilizing, on a scaled down overall dimension, the same design and construction techniques
1885 foreseen for the baseline of DS-20k (see Figure 28).

1886 The photodetector modules will be arranged to cover the top and bottom of the TPC. Both
1887 top and bottom planes consist of 185 photodetector modules assembled into 5 SQBs and 4 TRBs.
1888 As described in section 10, the readout chain will employ commercial components used during the
1889 first phase, allowing for full digitization of the signals. The final electronics components that will
1890 be used in DS-20k will be used as they become available at each stage of the development. It is
1891 also foreseen that the optical signal transmission will be tested on a significant number of channels
1892 with this detector.

1893 The DS-Proto photosensors are contained in 18 Motherboards made of one set of 5 (SQB) and 4
1894 (TRB) PDMs on top, and another identical set on bottom. With both planes, the DS-Proto TPC
1895 requires 370 PDM to be fully covered. Bonding ~9000 SiPMs in a few months is one of the most
1896 critical tasks of this detector, to maintain the overall project schedule. The construction strategy
1897 relies on two bonding facilities, the first one located at Princeton University and the second one
1898 at LNGS. According to the experience gained in the past months, a bonding rate of 3 tiles /d is
1899 feasible. We therefore need 60 d to bond the 370 tiles across the two facilities.

1900 The man power at LNGS can be provided by the NOA contracts, while finding man power at
1901 Princeton University is more challenging. Different options were evaluated, and others are under
1902 consideration. The University of Manchester (UK) has identified a candidate who will spend a
1903 significant amount of time in the course of the next year to be trained, and then do the work. A
1904 tight connection between the two production sites has to be provided, to include the harmonization
1905 of the procedures and quality assurance test. A person to provide this interface is being identified.
1906 LNGS requires a significant increase of man power since after the bonding the tiles will be equipped
1907 with a Front End Board (FEB), and then mounted and tested at LNGS. After the assembly, the
1908 tiles and the FEB will be tested in LN₂. The first Motherboard, made of 25 PDMs, was just
1909 assembled. The Motherboard will be shipped to Napoli, where a comprehensive test at cryogenic
1910 temperature is scheduled.

1911 A powerful test facility has to be prepared at Napoli, requiring extra man power. The procedures
1912 and the tools to ship the Motherboard from Pisa to Napoli and from Napoli to CERN have to be
1913 carefully planned and made available.

1914 13.3. Materials for DarkSide-Proto

1915 Since DS-Proto is a test bench of DS-20k, it won't be used to demonstrate the material radio-
1916 purity requirements of DS-20k, however, it will be built with the goal of achieving the best radio-
1917 purity conceivable at the time of the construction, based on the current results of materials assay
1918 campaign. Additionally, DS-Proto can be used to assess the possible contamination related to the
1919 detector construction procedures (TPC and PE), evidencing material cleaning/handling issues.

1920 The assessment of the DS-Proto radioactive budget will be obtained through the material assay
1921 campaign and the Monte Carlo simulation. The validation of the predictions concerning the neu-
1922 tron/gamma originated by the material contamination will be only possible through data taken
1923 underground with the DS-Proto deployed in a properly shielded environment. A physics run, fo-
1924 cused on the low-mass WIMP search, will be eventually possible with the S2-only analysis in the
1925 keV region. In this context, the minimization of the low-energy gamma background of the prototype
1926 will be extremely important to employ as early as possible.

1927 13.4. Validation tests and operation

1928 Upon successful completion of the test phase of the different parts, we plan to measure the overall
1929 performance of the DS-Proto through some key parameters, such as the S1 light yield, the electron
1930 drift time, electro-luminescence field and gas pocket thickness uniformity for high resolution of S2

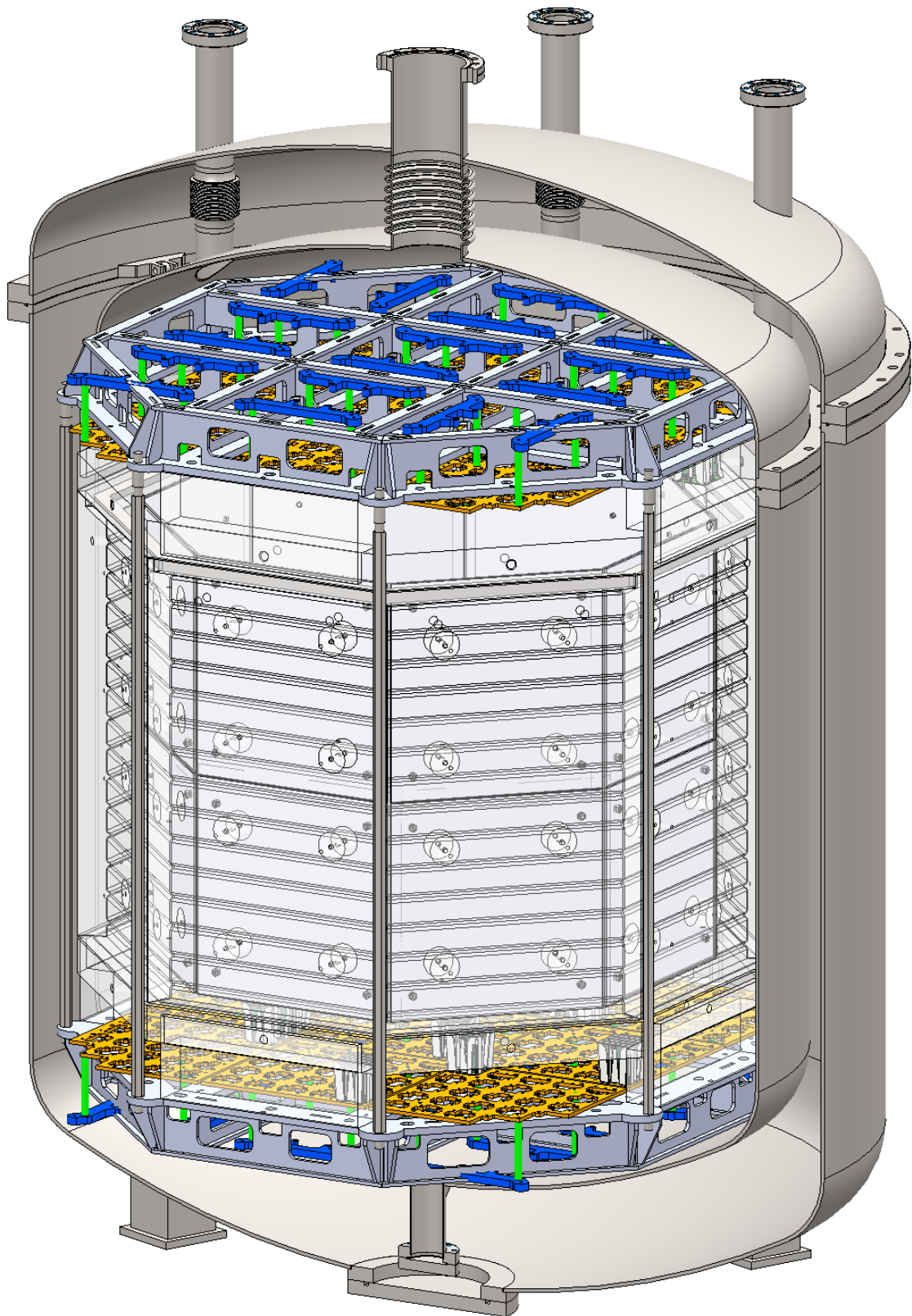


FIG. 28. Conceptual Design of the DS-Proto detector. The cryostat has already been built and delivered at CERN, see Fig. 27.

signals and the xy position reconstruction. For the purpose of optimizing the S2 signals, the first two Motherboards will be assembled into a small TPC with reduced size drift length (12 cm) to avoid pile-up (see Figure 29). Full test of the S1 response and therefore of the SiPM readout chain can be obtained at the surface by switching off the electroluminescence field. The configuration of the gas pocket (geometry and field) can be varied by changing the distance between the anode and the wire grid, the width of the gas pocket, as well as the electro-luminescence field. The S2 pulse shape can be precisely studied along with different gas pocket configurations, aiming to provide us the best solution for the future LAr TPC design. This set-up will also allow for early studies of the S2 formation and readout, to be carried out while the pre-production of the remaining Motherboards of the prototype is ongoing.

1941

14. AAR CRYOSTAT

1942 Figure 1 shows the DarkSide-20k system conceptual sketch, including the copper electromagnetic
1943 and light shield, the Veto detector and the LAr TPC, all contained within the large AAr cryostat.
1944 A ProtoDUNE-like cryostat will be employed to house the LAr bath which the TPC is immersed
1945 in and also acts as the main component of the Veto detector. This allows to minimize the material
1946 of the TPC vessel and therefore to limit the possible radio-contaminations very close to the active
1947 volume.

1948 Figure 30 shows the finished ProtoDUNE cryostat internal view while being cleaned, as well as
1949 the layout of passive thermal insulation materials that were used to construct the cryostat. The
1950 design concept for the DS-20k cryostat is based on the experience matured with the construction
1951 of ProtoDUNE cryostat. The technique is adopted from the LNG (Liquified Natural Gas) carriers
1952 and vessels, which has proven over many years its solidity and reliability.

1953 Two cryostats of the same size as the one proposed here have been constructed at CERN and one
1954 of them has been brought into operation in the second half of 2018. The experience gained there in
1955 the design, construction and operation will be fully translated to the DS-20k project, through the
1956 involvement of the CERN group that was responsible for the construction and operations of the
1957 ProtoDUNE cryostat. For that reason, the same mechanical constraints, dimension and thermal
1958 properties have been kept. The DS-20k cryostat is an improved version based on the experiences
1959 gained during the construction of the two ProtoDUNE cryostats, namely optimized fabrication and
1960 construction and access specific for DS-20k project. A 3D conceptual view of the external part of
1961 the cryostat being planned for DS-20k is shown in Figure 31.

1962 To make it as easy as possible for the access and support of the sub-systems of the TPC and the
1963 Veto detectors, all components will now be inserted from the roof of the cryostat, with a “closing
1964 cap” concept being implemented. This has been previously deployed by the CERN team during
1965 other large-dual phase TPC R&D experiments and tested with the construction and operation of
1966 the first demonstrator for the ProtoDUNE project. A cross-sectional view of the concept is shown
1967 in the right side of Figure 32. The plan is to assemble the bottom and sides of the Veto detector
1968 using a temporary support frame underneath the Veto detector, and then lower the TPC down into
1969 the Veto detector while it is attached to the closing cap, see Figure 24. Once in place, the remaining
1970 parts of the Veto detector could be assembled, the entire detector system support transferred to the
1971 detector support system of the cryostat, and finally the temporary supports of the Veto detector
1972 that we required during construction removed. At this point, the two detector volumes, that of the
1973 TPC and that of the Veto, would be filled simultaneously such that the LAr height in both volumes
1974 is equal at all times in order to reduce the mechanical stress on all of the detector components.

1975 As mentioned in Sec. 6, the AAr cryogenics system will be built based on the combined expe-
1976 riences of the ProtoDUNE cryogenics and the DS-50 cryogenics. The final optimization decision
1977 will be made taking into account that the different requirements of the AAr cryostat for DS-20k
1978 compared to those for ProtoDUNE, and the available space in Hall C of LNGS. Penetrations on the
1979 roof of the cryostat are being finalized such to meet the requirements of the other sub-systems, as
1980 well as to provide the mechanical stability of the cryostat ceiling. The design and development plan

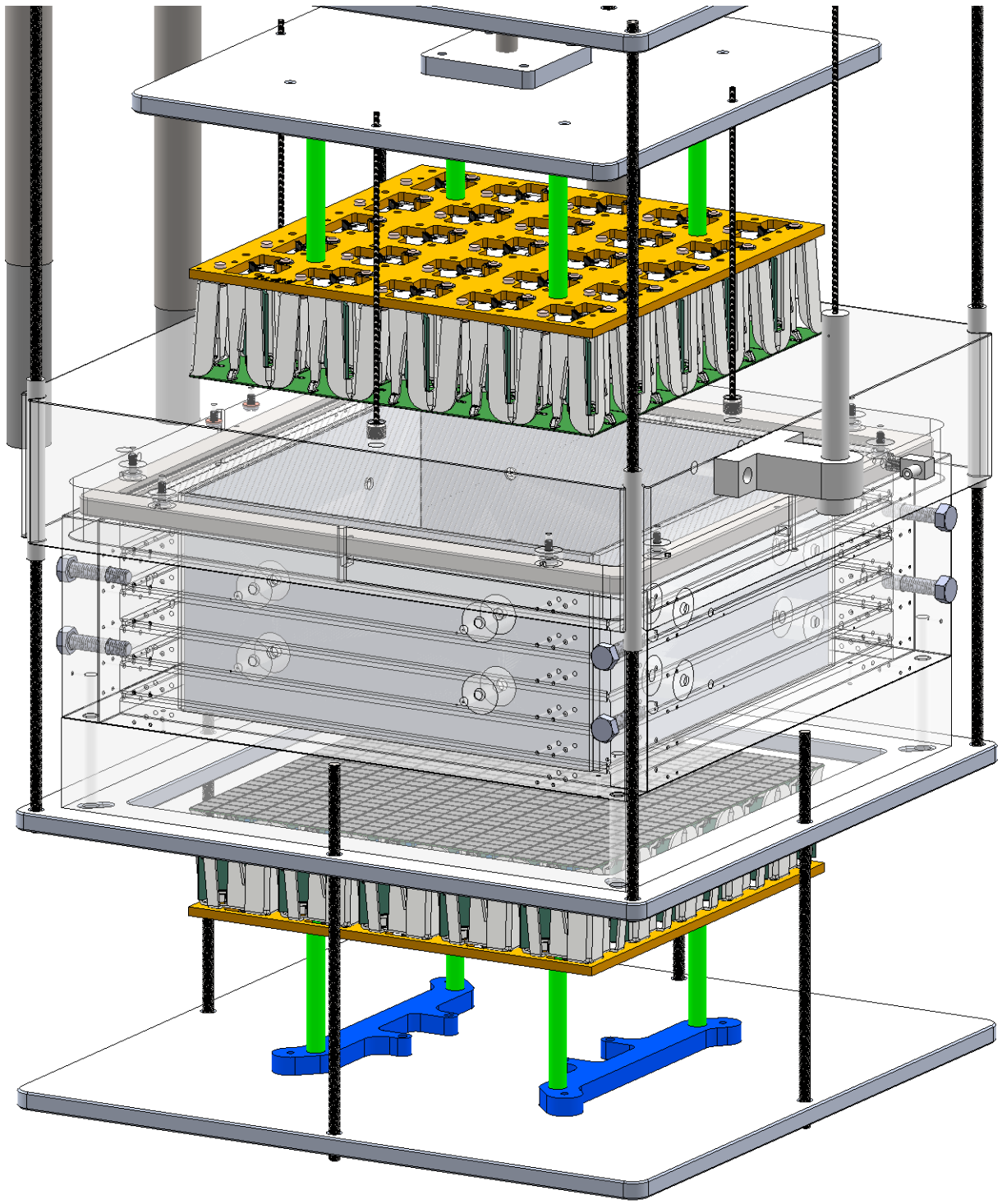


FIG. 29. Schematics of the setup for the optimization of the S2 signals.

¹⁹⁸¹ will follow the successful experience of ProtoDUNE, with expert engineering assistance provided
¹⁹⁸² by the CERN group, while already a firm baseline design is in place and schematically shown in
¹⁹⁸³ the left side of Figure 17, along with the rest of the DS-20k cryogenics system.

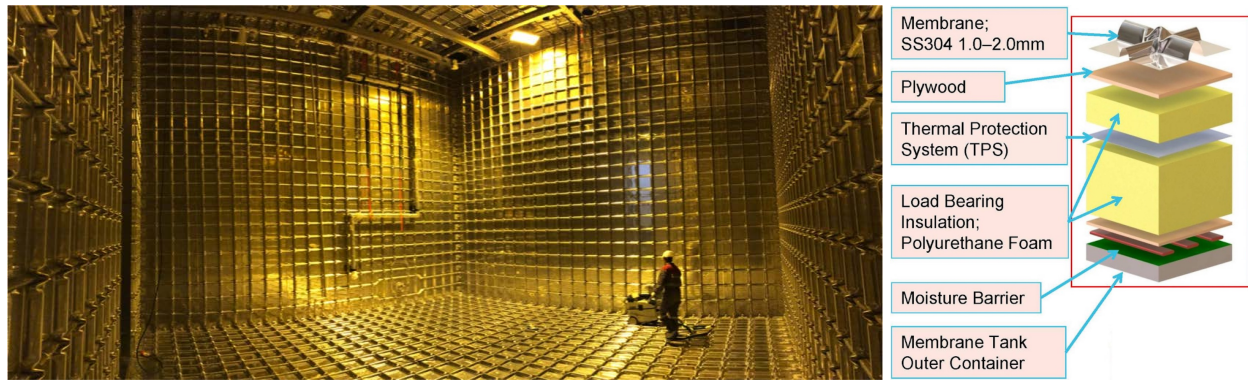


FIG. 30. **Left** Interior view of the ProtoDUNE cryostat used for the single phase LAr TPC test at CERN. **Right** Cryostat insulation construction details from GTT.

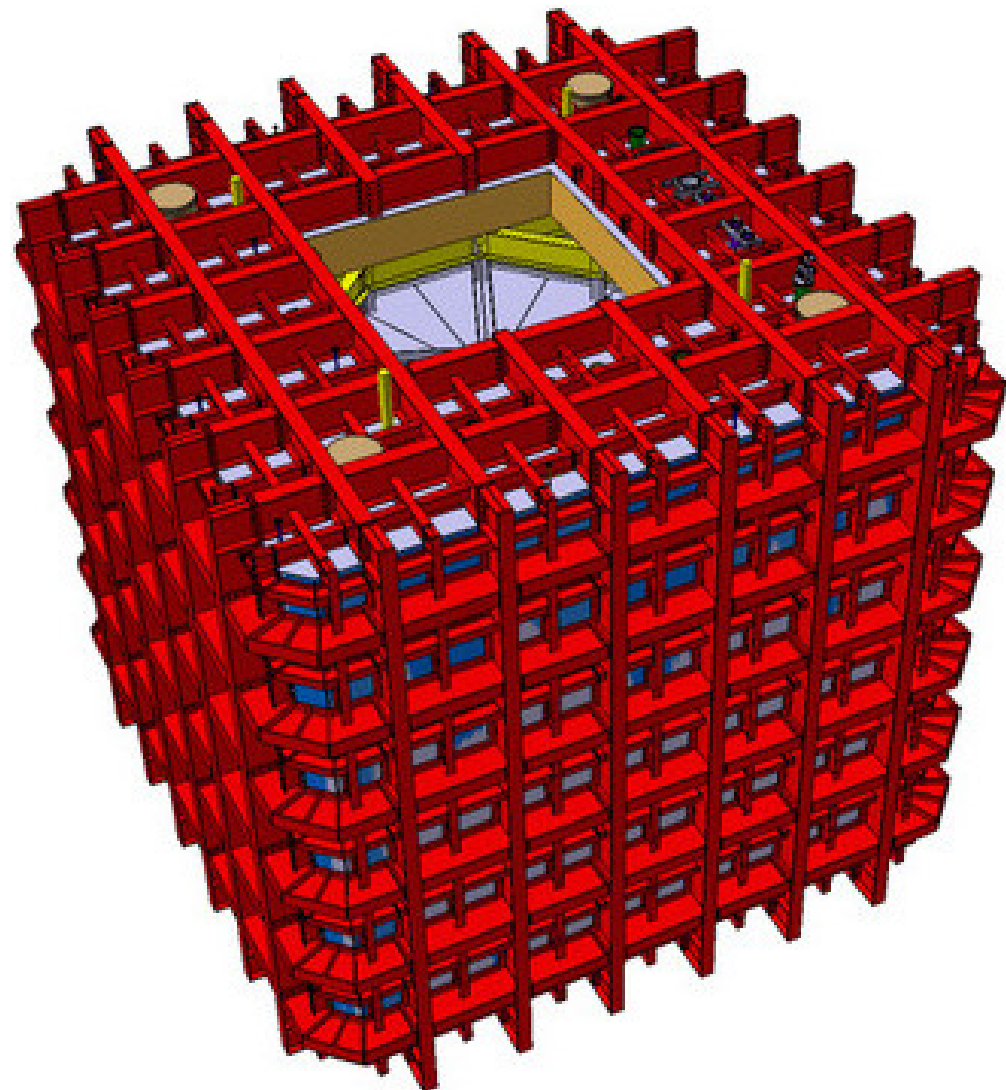


FIG. 31. 3D conceptual external view of the DS-20k AAr cryostat.

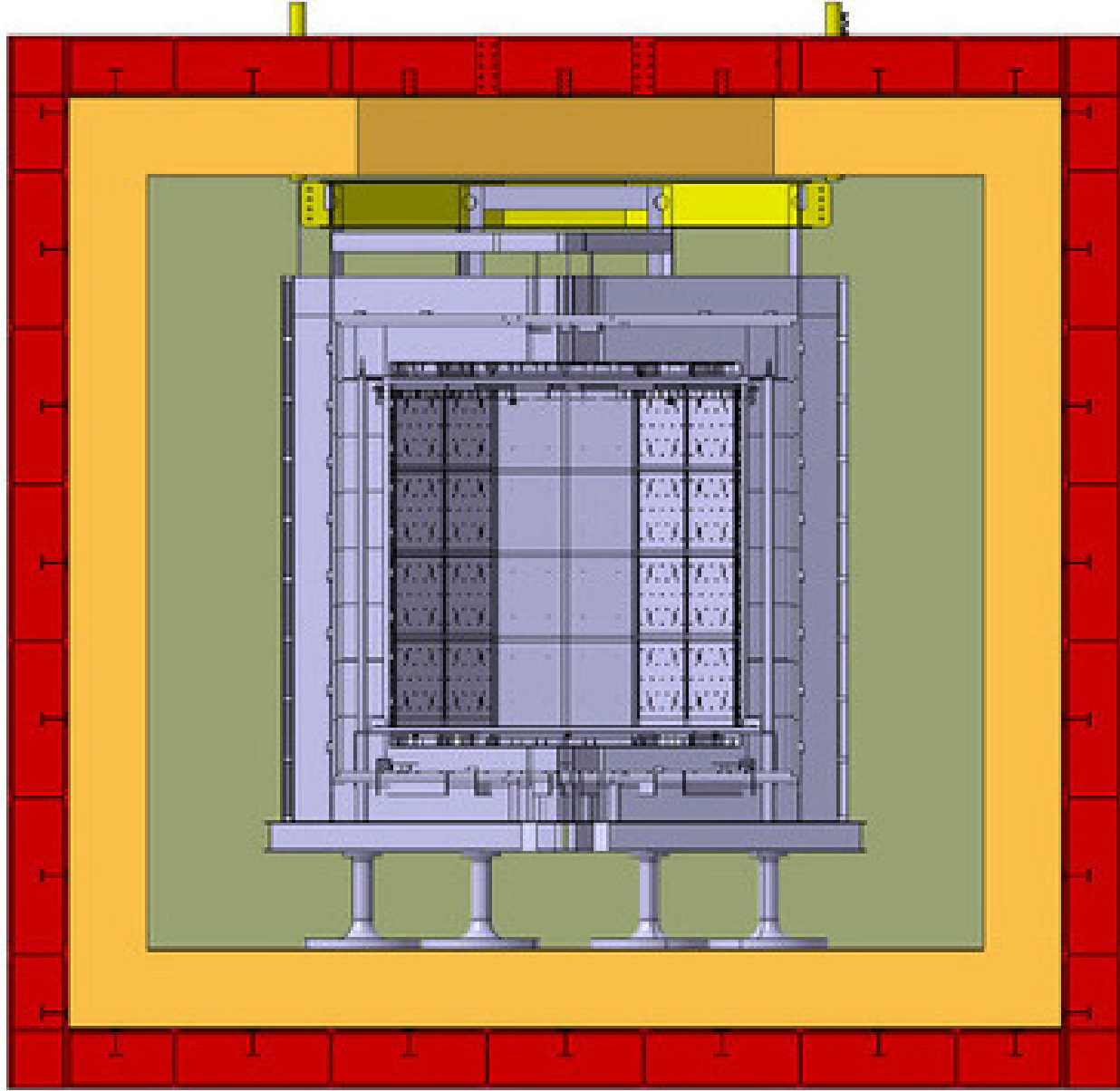


FIG. 32. Cross-sectional view of the large AAr cryostat containing the LAr TPC and Veto detectors and showing the top-cap concept.

1984

15. ARGON PROCUREMENT AND PURIFICATION

1985 A broad strategy has been developed to increase the production of UAr to procure the target
 1986 required for DarkSide-20k. The Urania project will extract and purify the UAr from the CO₂ wells
 1987 at the Kinder Morgan Doe Canyon Facility located in Cortez, CO, at a production rate of 250 kg/d.
 1988 It will be necessary to make a final chemical purification of the UAr before deployment into the
 1989 LAr TPC (driven by the filtration capacity of the getter purification unit), bringing the chemical
 1990 impurity levels to those shown in Table VII. Additionally, it would be beneficial to further deplete
 1991 the UAr of ³⁹Ar, giving extended sensitivity to DarkSide-20k and producing argon with a level of
 1992 ³⁹Ar that is acceptable to be used in an experiment such as Argo. The Aria project will serve to
 1993 chemically purify the UAr to better than the levels shown in Table VII using a cryogenic distillation
 1994 column called Seruci-I. The ultimate goal of the Aria project is to process argon through Seruci-I to
 1995 achieve an additional depletion factor between 10 and 100 (on top of the reduction of ³⁹Ar already

Element	Inlet Purity [ppm]
CH ₄	<0.25
CO	<0.1
CO ₂	<0.1
H ₂	<1
H ₂ O	<1
N ₂	<1
O ₂	<1

TABLE VII. Inlet argon purity required for operation of the DarkSide-20k getter.

1996 seen in the UAr).

1997 The procurement of the UAr for DarkSide-20k is broken into two main operations, extraction of
1998 the UAr by Urania and then chemical purification by Aria using Seruci-I.

1999

15.1. Urania

2000 The Urania project will extract at least 60 t of low-radioactivity UAr, providing the required 51.1 t
2001 of UAr to fill DarkSide-20k. The Urania project will also lay the groundwork for UAr procurement
2002 for future, larger argon-based detectors such as Argo. The goal of the Urania project is to build a
2003 plant capable of extracting and purifying UAr at a rate of 250 kg/d, from the same source of UAr
2004 that was used for the DarkSide-50 detector.

2005 The opportunity to build Urania has grown from the strong relationship between the DarkSide
2006 Collaboration and the Kinder Morgan Corporation. Based on gas analysis of the Cortez stream
2007 provided to Kinder Morgan by the DarkSide Collaboration during the extraction of the DarkSide-50
2008 UAr target, a major industrial partnership between Kinder Morgan and Air Products was estab-
2009 lished in order to extract helium from the CO₂ at Kinder Morgan's Doe Canyon facility. The Air
2010 Products helium plant began operation in July 2015 and presently supplies 15 % of the production
2011 rate to the National Helium Reserve.

2012 The DarkSide Collaboration reached an agreement with Kinder Morgan to feed the Urania plant
2013 with a small fraction (15 %) of the gas stream returned to Kinder Morgan by Air Products after
2014 helium extraction. This gas stream holds two significant advantages over the gas stream used to
2015 extract the UAr for DarkSide-50: it is completely dehydrated, and it contains only trace amounts
2016 of helium. These features greatly simplify the process for UAr extraction by the Urania plant,
2017 while ensuring the same radioactivity levels, or better. Argon from the active CO₂ wells in south-
2018 western Colorado have been found to contain very low levels of the radioactive isotope ³⁹Ar, with
2019 the concentration shown to be a factor of $(1.4 \pm 0.2) \times 10^3$ below that of argon derived from the
2020 atmosphere [5]. In an effort lasting more than 5 years, DarkSide-50 collaborators at Princeton
2021 and Fermi National Accelerator Laboratory (Fermilab) extracted and purified (156 ± 1) kg of UAr,
2022 slightly more than the (153 ± 1) kg needed for the target material in the DarkSide-50 detector.

2023 The Urania feed gas stream is $\sim 95\%$ CO₂, plus a few percent of N₂, one percent CH₄, 430 ppm
2024 of UAr, and traces of higher hydrocarbons. The processing scheme of the UAr extraction plant is
2025 optimized for this feed composition in order to achieve an UAr purity of better than 99.9 %. A
2026 modular plant consisting of skid-mounted units deployable on concrete platforms is being designed
2027 to carry out the processing.

2028 The UAr extraction plant will consist of three gas-processing units, as shown in Fig. 33, followed
2029 by a cryogenic distillation unit. The gas-processing units are two CO₂ liquefier/strippers followed
2030 by a pressure swing adsorption unit (PSA). The first liquefier accepts gas at (49 ± 1) bar, with
2031 a flow rate of 16 250 std m³/h and a temperature of 5 °C. At these conditions, the CO₂ partially
2032 condenses and the stream is separated into 2-phases (gas/liquid) as it goes to the first stripper.
2033 In the column a controlled quantity of heat is given by a hot fluid working between the chiller
2034 condenser and the column reboilers. The light products are vaporized and recovered from the top
2035 of the column in gas phase. The heavy products (mainly CO₂) are collected from the bottom,

2036 compressed to 120 bar and returned to Kinder Morgan as a liquid. The light products coming
2037 from the column head are cooled down in the second step to approximately -50°C and sent to the
2038 second stripper. The first column produces 1300 std m³/h of product flow, a factor of 5 reduction
2039 in the amount of gas to be processed by the more complex downstream units.

2040 The second liquefaction and stripping unit further reduces the CO₂ content, in a similar process
2041 as the first stripping unit. The separated CO₂ is joined with that from the first unit and returned
2042 to Kinder Morgan. The product gas from the second stripper is re-heated in a heat exchanger
2043 and delivered to the PSA unit, which separates the light fractions, including the argon, from the
2044 remaining CO₂. The PSA is composed of four adsorption beds to allow continuous operation with
2045 short time adsorption cycles. The desorption of CO₂ is made by decreasing the pressure on the bed.
2046 To optimize the performances, the operation of the adsorbers are combined by coupling the purge
2047 and pressure swing phases. At the outlet of the PSA adsorption tanks, one buffer tank is provided
2048 in order to dampen process fluctuations and allow for continuous operations of the final distillation
2049 process. The PSA off-gas is delivered to a recycle compressor and sent back to the second CO₂
2050 stripper inlet for reprocessing.

2051 The PSA is the most critical unit of the entire process since the dynamic adsorption conditions
2052 are the most difficult to simulate and predict. Optimization of the sorbent and other operational
2053 parameters is being done via a small scale lab setup in which breakthrough tests are being performed
2054 for a variety of gas species. A picture of the test setup being used is shown in Fig. 34. Sorbent
2055 screening relies on measurements of the breakthrough curves of the different gas species for the
2056 candidate sorbents. A selection of sorbents which could work for the PSA unit have already been
2057 identified, while the final selection of the exact sorbent to be used in the UAr extraction plant will
2058 be determined by the test results and consultation with the contracted company who will build the
2059 plant.

2060 The final unit of the UAr extraction plant consists of three cryogenic distillation columns. The
2061 CO₂-free product coming from the PSA plant is pre-cooled and sent to the first column, which
2062 works at a lower pressure (~ 9 barg) for the removal of CH₄. The second column is used to remove
2063 the remaining light fractions from the resulting N₂-rich stream, and the third to perform the final
2064 purification of the UAr using a batch distillation process. In addition to removing the CH₄ and N₂
2065 at this point, any ⁸⁵Kr present in the stream will also be removed by the series of three cryogenic
2066 distillation columns. The CH₄-rich and N₂-rich distillation wastes are returned to Kinder Morgan
2067 along with the CO₂. The final product, 99.9 % pure UAr, will be taken in liquid form from the
2068 top of the last column and a small portion collected into a tank to check the quality of the argon.
2069 The majority of the liquid UAr will be sent to the appropriate cryogenic vessels for shipment to
2070 Sardinia, where it will undergo final chemical purification by the Seruci-I column.

2071 The Urania project has recently made significant strides, most importantly with the opening
2072 of the tender for the construction and shipment of the argon extraction plant by the INFN. The
2073 opening of the tender has officially marked the start date for the progression of the sub-project
2074 schedule, and the timeline for the extraction of the 60 t of UAr required for the DS-20k experiment
2075 has now been set and has been integrated with the overall project schedule. It is now expected
2076 that the tender process will close at the beginning of the fourth quarter in the 2019 calendar year,
2077 and at that point a contract will be executed for the construction and delivery of the plant to the
2078 extraction site in Colorado, USA.

2079 The tender for the construction of the argon extraction plant has been opened and the winner
2080 will be selected and contract signed by the end of October, 2019. The plant will be delivered to the
2081 Kinder Morgan Doe Canyon Facility by the end of 2020 calendar year. The current plan is to install
2082 and commission the plant in the first three quarters of 2021 calendar year, allowing for extraction
2083 of the 60 t of UAr by the middle of the 2022 calendar year, in order to meet the DarkSide-20k
2084 schedule. The preparation of the extraction site is being planned now and will be managed by the
2085 collaboration with help from the Kinder Morgan CO₂ Company and the contractors hired to carry
2086 out the work. Site preparations for developing the facility before the arrival and installation of the
2087 plant will begin as soon as the necessary land development permits have been secured and the RFQ
2088 process has been completed.

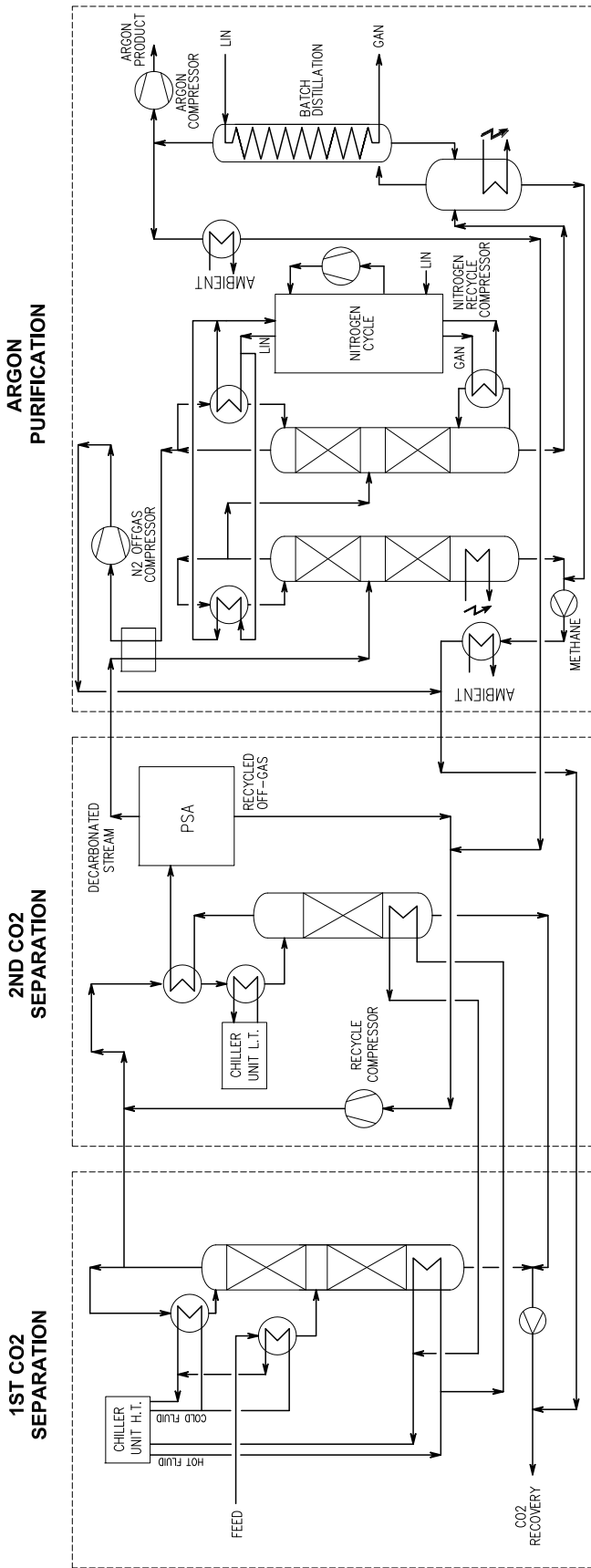


FIG. 33. Process Flow Diagram (PFD) for the Urania UAr extraction plant.



FIG. 34. Test plant in use at Università degli Studi di Napoli “Federico II” for the characterization and selection of sorbents for the PSA unit of Urania.

2089 The shipment from Colorado to Sardinia will be done by boat in order to minimize the cosmic
 2090 activation of the argon. For the shipment of the UAr from Colorado, two options are under
 2091 investigation. The first option, which was determined to be the baseline method, is to ship the
 2092 UAr in liquid phase using custom built cryogenic vessels. This is a more efficient and cost effective
 2093 method, compared to shipping the UAr in gas phase. The custom built cryogenic vessels will have
 2094 a double wall structure, there will be two inner volumes with the larger one containing the UAr and
 2095 the smaller containing LN₂. The outer volume would be at ultra-high vacuum to thermally insulate
 2096 the two inner volumes from the atmosphere at ambient temperature. During the transport, a LN₂
 2097 fed condenser would slowly re-liquify the UAr as it evaporated away, ensuring that none of the UAr
 2098 would be lost during the trip. A schematic view of the cryogenic vessel design is shown in Fig. 35.
 2099 A minimum of five cryogenic vessels is foreseen enabling one for Urania production, one for Aria
 2100 feed, one for Aria production, and two traveling between Sardinia and LNGS for delivery and then
 2101 LNGS and Sardinia for further production of UAr, at all times.

2102 In the case of cryogenic shipping, the extracted UAr will be shipped to Sardinia in batches of
 2103 11 t (roughly every 100 days) in liquid phase, also eliminating the need to liquify the UAr to be
 2104 reprocessed by the Aria column. After chemical purification in Aria, the UAr will then be shipped
 2105 to LNGS, also in batches of 11 t, and stored in the argon recovery system. In order to minimize
 2106 the exposure to cosmic rays, the argon will be stored underground at Seruci and/or LNGS for any
 2107 necessary long durations.

2108 The second option that is now being investigate as an alternative, is to ship the UAr in high-
 2109 pressure gas cylinder placed in trailers which can be hauled by trucks. This option is made possible
 2110 by special cylinders which allow for the storage of argon at pressures up to 400 bar. With pressures
 2111 of this magnitude, and cylinders that are able to be the size of large trailers, the number of trailers
 2112 that would be required for the total DS-20k detector target is something that is manageable, on the
 2113 order of 10 to 20 depending on the storage pressure. The overall benefit of moving to this option,
 2114 instead of going with the cryogenic vessel option, is that the gas can be maintained in the cylinders
 2115 for years without the need of any type of consumable to prevent the loss of the argon. This would

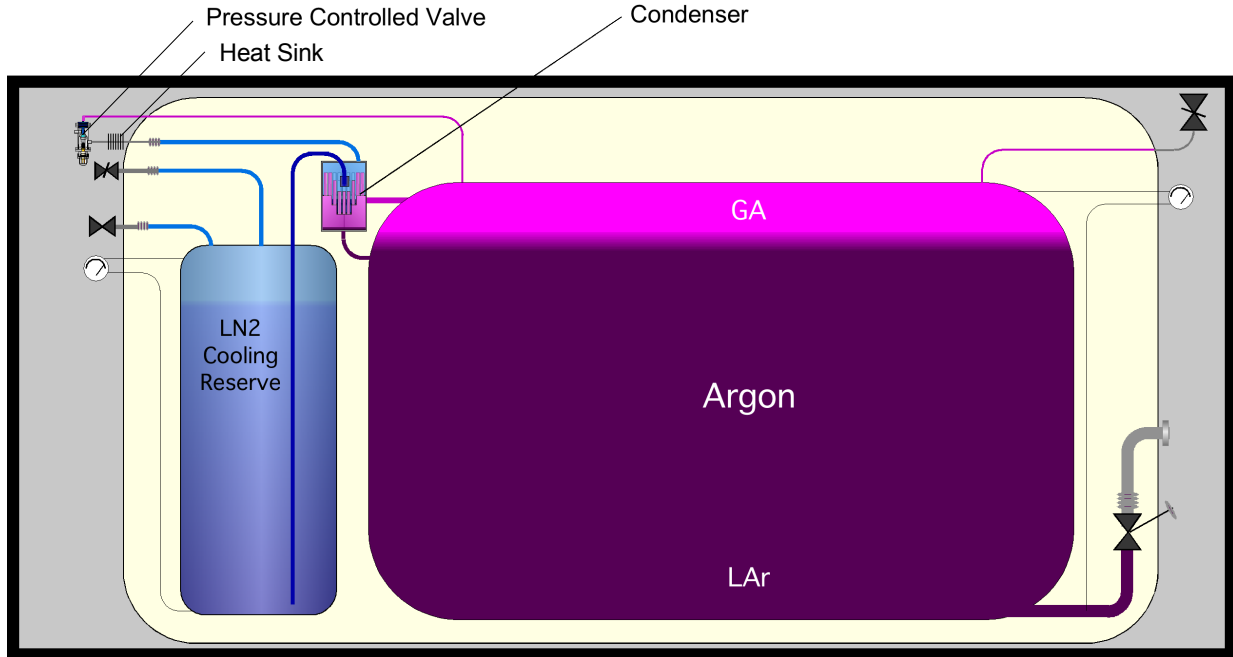


FIG. 35. Schematic view of the cryogenic shipping vessel design, one of the two options for argon shipment from Colorado to Sardinia.

basically eliminate the risk of losing any of the UAr during the transport and storage, other than potential loss of the shipment.

The Urania project team is now collecting all of the information that is required to make the technical and economic assessment of the two options. Based on the technical risks and the economic impact on the project, the option that is best for the overall project will be chosen.

2121

15.2. Aria

2122 The aim of Aria is to perform chemical purification of the UAr extracted by Urania. Aria will also
 2123 be the test bench to develop active depletion of ^{39}Ar from the UAr to possibly provide DAr targets
 2124 for future larger-scale LAr detectors. Aria consists of a 350 m tall distillation column, Seruci-I,
 2125 capable of separating isotopes with cryogenic distillation, a process that exploits the tiny difference
 2126 in volatility due to the difference in isotopic mass [61–66].

2127 The design of the plant started in April 2015 with seed funding from the US NSF through
 2128 PHY-1314507. Aria is to be installed in a underground vertical shaft of 5 m diameter and 350 m
 2129 depth, located at the Seruci mine campus of CarboSulcis, a mining company owned by the Regione
 2130 Autonoma della Sardegna (RAS). In February 2015 a proposal was submitted to the Italian INFN
 2131 and RAS, and the funding for the Seruci-I column was approved on July 24, 2015. Construction
 2132 of Seruci-I modules started in September 2015 in a Italian company.

2133 The measurements of the relative volatility of argon isotopes [67–69] and their theoretical inter-
 2134 pretation [70–72] marked the birth of the Italian school of condensed matter in Genoa and Milan.
 2135 The study of the relative volatility of argon isotopes was recently revisited [73, 74] and shows a
 2136 promising path for the separation of ^{39}Ar from ^{40}Ar . Following these studies, DarkSide collabora-
 2137 tors developed the framework for comparing ^{39}Ar to ^{40}Ar . Algorithms developed to calculate the
 2138 relative volatility of argon isotopes, based on the extensive and detailed models available in the
 2139 literature, predict that the volatility of ^{39}Ar relative to ^{40}Ar is 1.0015 ± 0.0001 , and that it stays
 2140 constant within theoretical uncertainties in the range of temperatures practical for the distillation
 2141 of argon (84 K to 100 K). The small volatility difference can be used to achieve active isotopic
 2142 separation by using a cryogenic distillation system with thousands of equilibrium stages.

2143 Design of the Aria plant was optimized on the basis of high-precision numerical methods for
2144 estimating the isotopic separation of ^{39}Ar from ^{40}Ar . DarkSide Collaborators developed two in-
2145 dependent numerical codes, one based on the McCabe-Thiele method [75], and a second based on
2146 the Fenske-Underwood-Gilliland (FUG) method and its derivative, the Wynn-Underwood-Gilliland
2147 (WUG) method [76–78]. Calculations for the isotopic separation power of ^{39}Ar from ^{40}Ar and of the
2148 processing rate were performed with the custom codes, as well as with software routines supported
2149 by commercial chemical engineering CAD programs, such as Aspen [79].

2150 Fig. 36 illustrates the core of the process for isotopically separating ^{39}Ar from ^{40}Ar . The process
2151 consists mainly of two loops: the process loop where the argon is distilled and the ^{39}Ar is separated
2152 from the ^{40}Ar , and the refrigeration loop where nitrogen gas and liquid is used to evaporate and
2153 to condense the argon. Most of the heat is recovered, thanks to the compressor that pumps the
2154 nitrogen gas evaporated in the condenser to the reboiler and to the pumps that move the liquid
2155 nitrogen produced in the reboiler to the condenser, making the system as efficient as possible. In
2156 Fig. 36 all the sub-parts of the plant are represented:

- Feed station, to filter and regulate the feed to the column;
- Compressor station, to bottle the distillate at the bottom;
- Vacuum system, to keep a good vacuum in the cold-box, in order to minimize the heat losses;
- LN_2 storage;
- Nitrogen condenser system, consisting of 4 Stirling cryo-refrigerators needed to re-condense the
nitrogen, used in a closed loop.

2163 Seruci-I will consist of 28 modules of 12 m height, plus a top module (condenser) and a bottom
2164 module (reboiler).

2165 Calculations indicate that Seruci-I will be able to process UAr at a rate of $O(1 \text{ t/d})$ removing all
2166 chemical impurities (including traces of N_2 , O_2 , and Kr) with a separation power better than 10^3
2167 per pass. Additionally, Seruci-I can be used in a different mode of operations to test the isotopic
2168 separation of the argon, in order to further reduce the ^{39}Ar content in the UAr. The same models
2169 which have been used to calculate the chemical purification rate, have also been used to show that
2170 Seruci-I would be able to isotopically separate the UAr at a rate of 10 kg/d, while obtaining an
2171 ^{39}Ar depletion factor of 10 per pass.

2172 All modules for Seruci-I have already been built and passed a series of quality assurance checks.
2173 During the first check, the process column and all the service pipes were individually checked for
2174 leaks at room temperature. Then, the pipes were wrapped with super-insulation and everything
2175 was assembled into the cold box. The second check was a full module check, with an additional
2176 check done on the bottom reboiler module at 77 K. To date, all modules have passed both checks
2177 at room temperature and the bottom module has passed the final cold temperature check.

2178 Seruci-0 is a test column that is made with the Seruci-I top and bottom modules and a single cen-
2179 tral module. The goal of Seruci-0 is to confirm the proper operation of the three main components
2180 of the Seruci-I column, as well as to gain experience in operating the column on a smaller scale
2181 and to put in place the standard operating procedures. The three modules have been completely
2182 installed in a outdoor assembly hall at Nuraxi Figus, Italy, seen in Figure 37. During the last
2183 months, all the leak-check tests have been performed in order to guarantee the design tightness.
2184 Moreover, most of the plants have been installed and assembled in the area surrounding the column
2185 itself. Moreover, two concrete platforms were built: they currently host the liquid nitrogen dewar
2186 and the accessory plants, the cooling machine (chiller) and a control room to host people on shift
2187 and to organize the slow control. Test operations of Seruci-0 will start in summer of 2019.

2188 Concerning the installation of Seruci-I, all the documents needed for the authorization request
2189 for installation were submitted in May 2018 to the competent authorities. During the first half
2190 of 2019, several meetings have been held, both with the fire brigade and with other local and
2191 county offices, entities and authorities. The authorization were eventually obtained. During 2018 a
2192 complete cleaning and preparation of the well at the Seruci site has been performed. A well-defined
2193 coring procedure was concluded in 2018. After the examination of the rocks samples, the design for
2194 the Seruci-I supporting structure was detailed. The tender was completed in Autumn 2018, and
2195 at the beginning of 2019 a carbon steel sample platform was delivered to the mine and installed in

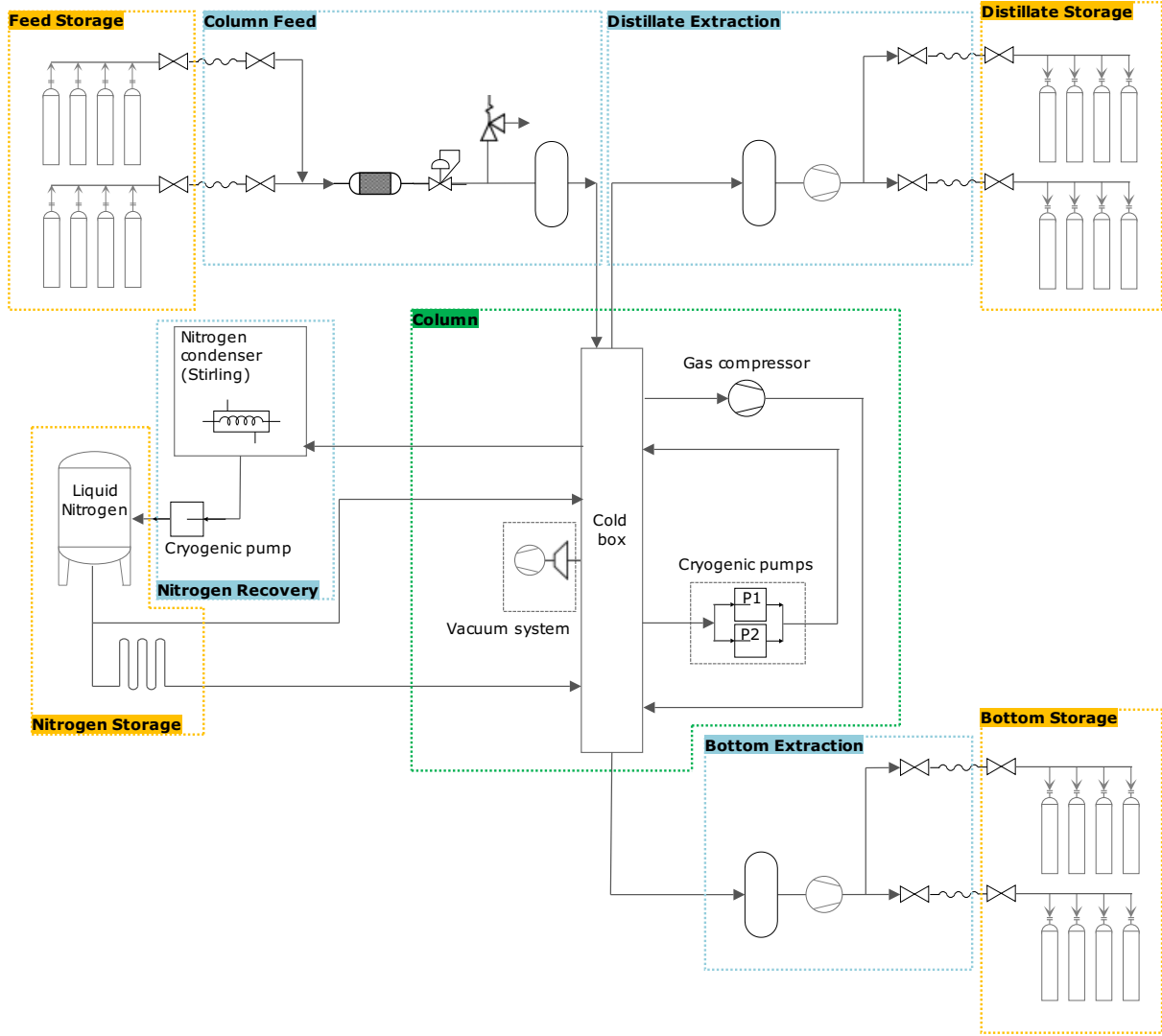


FIG. 36. Block diagram of the cryogenic system of the Aria plant.

2196 the Seruci well. The test was successful and was very useful in order to define all installation steps.
 2197 The goal is to receive all of the platforms by the end of May 2019 and to install them inside the
 2198 well by the end of 2019.

2199

15.3. DArT

2200 The DArT experiment will re-use the ArDM infrastructure with minimal modifications made
 2201 and will consist of a radio-pure single-phase LAr detector with about one liter contained inside of
 2202 its active volume. The DArT detector itself will be placed inside the middle of the ArDM vessel.
 2203 DArT will be filled with argon to be tested in order to measure the content of ^{39}Ar . The detector
 2204 will be readout by two cryogenic SiPMs each with a surface area of 1 cm^2 . The SiPMs and the
 2205 readout electronics will come from the DS-20k production chain.

2206 The ArDM detector will act as an active veto against internal and external radiation. For this
 2207 purpose, we are building a dedicated single phase setup with a new set of low-radioactive photo-
 2208 multipliers (PMT). However, we will also retain the entire present double phase setup for later use,
 2209 e.g. for measurements of large quantities of depleted argon.

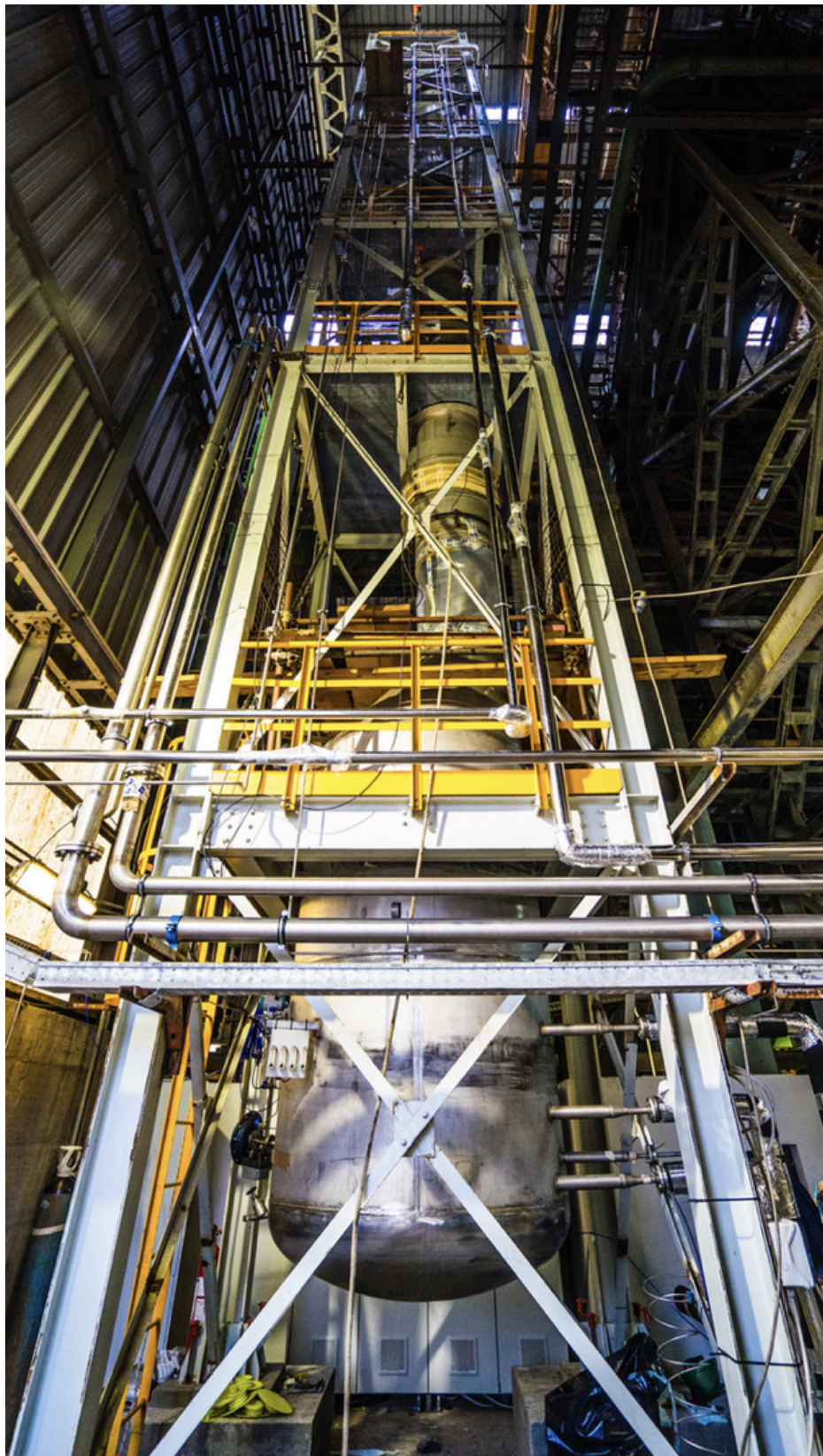


FIG. 37. The Seruci-0 cryogenic distillation column, installed in the *Laveria* building of Carbosulcis in Nuraxi Figus, Sardinia, Italy.

2210 Extensive GEANT4-based simulations were performed using the Monte Carlo simulation package
2211 inherited from the DarkSide-50. These simulations show that DArT will achieve a sub-% measure-
2212 ment when operated inside the ArDM detector, for ^{39}Ar concentrations a factor of ten smaller
2213 than those of AAr, and in about a week of running. A 2% measurement could be made for ^{39}Ar
2214 concentrations as low as two orders of magnitude (statistical uncertainty only) smaller than those
2215 in AAr. This setup will also be useful to characterize the performance of Aria, which is expected
2216 to suppress the ^{39}Ar content by a factor of 10 per pass.

2217 A very important addition to the setup described above will consist of adding a 6 t lead belt
2218 about 140 cm tall around the ArDM vessel, at the mid-height position. This will suppress the
2219 impact of external photons that dominate the background budget and allow for the measurement
2220 of even larger ^{39}Ar depletion factors, corresponding to that of the UAr. If the depletion levels are
2221 those already measured in the past (i.e. of 1400), it will be possible, according to our simulations,
2222 to measure them with a 7% uncertainty in about a week of running. Upper limits can be set on
2223 depletion factors of order 25 200 (statistical uncertainty only), i.e. UAr with one distillation pass
2224 in Aria.

2225 The argon from Urania is expected to be available only after mid-2021. However, it is planned
2226 that after the run of DS-50 at LNGS, presumably at the end of 2019, its argon will be measured with
2227 DArT to cross-check the original measurement taken with DS-50 and to test the new setup. This
2228 DArT experiment is expected to become a useful facility within LSC for the years to come, since
2229 it will be needed to measure samples of the extracted argon from Urania over time. An Expression
2230 of Interest and a TDR were recently submitted to the LSC Directorate. Detector construction in
2231 all collaborating institutions has already started.

2232 16. TECHNICAL DESIGN

2233 **Viene descritto lo spazio richiesto presso le aree dei laboratori di superficie e sotter-
2234 ranei. In questa parte inoltre vengono descritte nel dettaglio tutte le scelte tecniche
2235 fatte, la loro implementazione e conseguentemente i sistemi e sottosistemi. In partico-
2236 lare si richiedono le specifiche funzionali e tecniche dell'infrastruttura, degli impianti
2237 e delle attrezzature in termini di:**

- 2238 • opere civili,
- 2239 • impianti elettrici,
- 2240 • HVAC (riscaldamento, ventilazione e condizionamento dell'aria),
- 2241 • acqua di raffreddamento/ deionizzata,
- 2242 • aria compressa,
- 2243 • attrezzature in pressione,
- 2244 • sistemi da vuoto e criogenici,
- 2245 • sistemi di sollevamento e trasporto,
- 2246 • supervisione e controllo,
- 2247 • sicurezza,
- 2248 • IT,
- 2249 • radioprotezione,
- 2250 • meccanica,
- 2251 • elettronica.

2252 **Si richiede di allegare i documenti tecnici al momento disponibili dalla Collaborazione
2253 (esempio: P&I, schede tecniche, elaborati tecnici, . . .).**

2254

16.1. Installation Space and Services Needed

2255 The complex installation procedures will be described in details in Section 18 18.6, here we give
 2256 the general overall size of the needed spaces and services to be available in Hall C for a smooth,
 2257 fast and successful construction of the DS-20kdetector.

2258 DISCUSSION OF THE SABRE ISSUE

2259 It is to be noted preliminarily that the installation sequence is designed to use all the HALL-C
 2260 floor from the entrance up to the CTF and other Borexino installations. This arrangement which
 2261 anticipate vacating the space allocated, as of this writing, to the SABRE POP is optimal from the
 2262 point of view of simplifying and thus speeding up considerably the installation of the outer cryostat.
 2263 In addition the same space would be used for installation of counting rooms and other vital equip-
 2264 ment for DarkSide-20kthat otherwise would need to be installed on steel structures overhanging
 2265 the SABRE POP space, complicating the design, cost and construction of those structures. (to be
 2266 elaborated further)

2267 The requirements for the installation of the DarkSide-20kdetector are then summarized below:

- 2268 • Total available surface in Hall C: 14m x 26m (or 2 x 14m x 14m). The surface needed for
 2269 cryostat installation is 14m x 14m, and additional 14m x 14m for cryostat parts pre-assembly.
- 2270 • Connections panels for construction phase (“quadri da cantiere”): Four 3-phases panels (32A
 2271 each) for a simultaneous use of welding machines
- 2272 • Mono-phase connection plugs of 230 VAC (16A each)
- 2273 • Panel 24VAC for lighting inside the cryostat.
- 2274 • Pressurized air: oil free, 6.3bar, 300 l/min with 3000 l/min peaks.
- 2275 • Availability of Hall C cranes, in particular:
 - 2276 - Use of the 20+20 tons arch crane for cryostat installation and cryostat roof operations
 - 2277 - Use of the flat cranes for clean room mounting, test cryostat and TPC mounting
 2278 operations.
 - 2279 - Removal of the 5 ton cranes to optimize the operations of the 20+20 tons arch crane.
- 2280 • Unloading Station availability in the TIR gallery.
- 2281 • Gas detection systems (Oxygen detectors) and fire protection systems in Hall C.

2282

16.2. Electrical Power for DS-20kOperation

2283 A total power of 222 kW is needed for DS-20k:

- 2284 • Cryostat (reference as in CERN NP04 cryostat) : 27KW
- 2285 • DAQ (see Air Conditioning System)
- 2286 • Ancillaries (Water Plant, Exhaust, Radon Abatement System, Lighting): 50KW
- 2287 • Nitrogen Recovery System: 100KW (connection already there in Borex electric box)
- 2288 • Air Conditioning System: 45KW

2289 In addition a powerful UPS line is needed with a total capability of delivering 85 kW for the time
 2290 needed to put in safe conditions all the delicate equipment:

- 2291 • Cryostat and external cryogenics: 10KW
- 2292 • DAQ: 45KW
- 2293 • Gas Panel: 25KW
- 2294 • Control System: 5KW

2295 **16.3. Nitrogen Argon and Water Services for DS-20kOperation**

2296 For cooling purposes the following water supply is needed:

- 2297 • Cryo-coolers and external cryogenics: TBD
- 2298 • Detector cryogenics: 1.0 mc/h
- 2299 • Air Conditioning System: 45KW (1.5 mc/h)
- 2300 • Fan-coil building : to be provided from LNGS services.
- 2301 • Radon Abatement System: 0.45 mc/h

2302 For Nitrogen and Argon the following is foreseen:

- 2303 • Use of the 20 m³ Nitrogen LINDE tank placed in the TIR gallery (currently in use by DarkSide-50 and Borexino)
- 2304 • Use of High Purity Nitrogen system
- 2305 • Use of the already existing Nitrogen recovery system. The system is ready to be used. It is instrumented with two Stirling engines, and with a distribution system for the recovered nitrogen in gaseous phase and for the disposal of the recovered liquid nitrogen in the 20 m³ LINDE tank.
- 2306 • Use of a 10 m³ buffer Argon tank for 5.0 Argon to be used for cryostat filling operations and to be located externally to Hall C, along the TIR gallery with a distribution line serving Hall C.

2313 **16.4. Underground Argon Storage and Transport**

- 2314 • The current DS-20k detector and cryogenic services layout implies the use of the TIR gallery for the storage of depleted underground argon (UAr) arriving from the ARIA plant in Sardinia.
- 2315 • The UAr transportation system and containers will also play the role of UAr recovery system, it is therefore foreseen that it is disposed in TIR gallery for the whole experiment lifetime.
- 2316 • The dimensions, volumes and operational working points of UAr shipping and storage system will be specified as soon as they will be defined.

2321 **16.5. IT Infrastructure**

2322 Data connection with external would need 2 fibers with 10 Gbps bandwidth (to be updated)

2323 **17. VALIDATION**

2324 **Sulla base della descrizione tecnica fornire i risultati degli studi, delle simulazioni e delle misure che dimostrano la congruità tecnica e la robustezza dell'implementazione proposta.**

2327 **18. INSTALLATION AND COMMISSIONING**

2328 **Descrizione delle differenti fasi e procedure dell'installazione e del commissioning delle infrastrutture e dell'apparato dettagliando la logistica (trasporti, procedure e stoccaggio) associata e le soluzioni trovate per risolvere le criticità.**

2329 In the following, we describe at first the main technical details of each key element of the entire DS-20k infrastructure in terms of services and detectors. At the end of the section, a step by step 2333 installation sequence proposal is described with the help of sketches of the making process of DS-20k

2334 in LNGS Hall C. The planned activities in Hall C in terms of installation and commissioning are
2335 aimed at the construction of the cryostat and the attached cryogenics system, the construction of
2336 the metal structure supporting the cryogenics, the construction of the detector test radon free clean
2337 room, the assembly of the outer veto detector, and the final assembly and test of the inner TPC. The
2338 Cryostat, and its ancillary structures, is the main and larger element of the DS-20k infrastructure
2339 and will impact significantly Hall C environment in terms of space and needs especially during the
2340 installation and construction phase. As a consequence, particular focus is given to the cryostat
2341 technical description and installation sequence.

2342 18.1. Cryostat Description and Construction

2343 The design concept of this cryostat is based on the experience matured with the construction
2344 of similar vessels for the DUNE long baseline neutrino experiment. The adopted technique is the
2345 one of the LNG (Liquified Natural Gas) carriers and vessels, which has proven over many years
2346 its reliability. Main characteristics are the passive thermal insulation, and the inner wall with a
2347 corrugated layout designed to allow contraction and expansion of the main liquid volume. Two
2348 vessels of the same size as the one proposed here have been constructed at CERN. The experience
2349 gained there in the design, construction and operation will be fully translated to LNGS. The
2350 cryostat itself consists of two main parts: a warm and a cold structure. The main function of the
2351 warm structure is to deal with the hydrostatic pressure coming from the liquid. The internal cold
2352 structures insulate the vessel towards the outside and provide the containment of the liquid argon.
2353 All structural analysis are already available and updated with a new seismic analysis, taking into
2354 account the particular conditions of the Gran Sasso laboratory.

2355 **The warm structure.** The warm structure is the outer vessel, which is kept at room tem-
2356 perature and will grant the structural integrity of the entire setup. It consists of an assembly of
2357 standard steel profiles. The overall outer dimensions are: width 11404 mm, length 11404 mm,
2358 height 10756 mm. The warm cryostat itself will be made of about 250t of hot rolled profiles and
2359 bolts. The steel structure consists of vertical beams alternated with a web of metal frames. Inside
2360 the steel structure, a skin of stainless steel plates is welded, such as to provide a gas barrier to
2361 the outside. This mechanical structure sits on top of the Hall C concrete floor. The top of the
2362 cryostat will be accessible for installation of the active inner detectors (TPC and veto counter), the
2363 electrical signal feedthroughs, the detector supports and other cryogenics services. The structural
2364 beams load-bearing elements consist of IPE V 600 and IPE O 270 standard profiles. Stainless steel
2365 plates, 10 mm thick, are welded to the web interlink structure to create a gas containment barrier
2366 to the inside and ensure even better support for the passive thermal insulation. The cryostat body
2367 will be fully electrically insulated from the building ground.

2368 **Insulation and inner membrane.** The insulation consists of two layers of foam supported
2369 by plywood plates. The inner membrane is made out of stainless steel 1.2 mm thick. The main
2370 characteristic of this primary membrane, in contact with the cryogenic liquid, is to be capable to
2371 expand and shrink as a function of the temperature, thanks to a special corrugation configuration,
2372 which makes it acting like a bi-dimensional spring. The insulation consists of two layers of a
2373 foam especially developed for this purpose supported by plywood plates. The first insulation layer
2374 is attached to the 10 mm-thick outer Stainless Steel (SS) skin. The foam material is expanded
2375 polyurethane with a density of 90 kg/m³. Between the two layers of insulation there is a secondary
2376 containment system made out of a thin layer of a triplex Aluminum based fabric. In contact with
2377 the foam, on the cold side, there is the primary membrane made out of stainless steel (304L) 1.2
2378 mm thick. The overall thickness of the insulation and membranes is 800mm. Thermal fluxes are
2379 to be controlled so that the unitary value calculated in unidirectional model is below 6.3 W/m²
2380 on the wall and floor in contact with the liquid. The tertiary membrane made of SS 10mm plate
2381 of the type 304L will account for 50t of material. The insulation foam will account for 35 t of
2382 polyurethane with an addition of about 20 t of plywood. The inner primary corrugated membrane
2383 will account for 7 t of SS 304L, for which the raw material batch can be selected according to the

2384 required radioactive contamination levels.

2385 **Cryostat construction and installation activities.** To ease the installation, it is proposed
2386 to have a square opening on the roof of the cryostat with dimensions of 4250×4250 mm². A top
2387 cap will close this opening with the inner detectors hanging from it. This top cap will host all the
2388 penetration necessary to support the active detector, all electrical and signal feedthroughs and the
2389 cryogenics services. Four large size penetration will be placed on the four corners of the roof of the
2390 cryostat with the purpose of allowing access to the inside, to bring clean air inside the vessel during
2391 installation and the necessary cryogenics service for the LAr bath. Particular attention will be
2392 given in all steps of the construction work to minimize the radio contamination of the materials, in
2393 particular for the the SS primary membrane closer to the detector. Cryostat installation sequence
2394 steps are described at the end of this section.

2395 **Cryostat construction schedule.** The thermal insulation and inner membrane are based on
2396 the LNG technology developed by the firm GTT (Gaztransport & Technigaz) and today imple-
2397 mented in about 80 % of all LNG transport ships. This is a proprietary technology, well protected
2398 by IP regulations. GTT is not directly constructing LNG carries, but has defined a network of
2399 firms which have the permission to use their technology and IP. In this framework GTT would do
2400 the full engineering of the cold vessel. In 2015 CERN has managed to establish a collaboration
2401 agreement with GTT. The full engineering design is part of the current integration work performed
2402 by the collaboration and driven by CERN. For the in situ assembly of the warm structure, previous
2403 experience shows that, once the modules are available, it takes 16 weeks for the full process. The
2404 assembly of the cold structure will be done in 35 weeks. For the moment we do not add a precise
2405 operation time to each step which are described in the following. This until we understand the
2406 entire logistic and the lab requirements.

2407 18.2. Metallic Structure

2408 The metallic structure proposed here will be used to allocate the Cryogenics System and part
2409 of the electronics for the DS-20k TPC and Veto detectors. The structure will be connected to the
2410 roof of the warm outer cryostat, where equipments for the calibration, the safety devices, and TPC
2411 leveling system will be also located. The construction of the metallic structure will begin once the
2412 warm outer structure of the cryostat will be finalized.

2413 18.3. Cryogenic System

2414 A cryogenic system has to be built in order to serve the DS-20k experiment cryostat filled
2415 with Atmospheric Argon (AAr). This system must be able to efficiently purify, recirculate and
2416 maintain 682 tons of AAr. It will include several subsystems: the liquid argon handling system, the
2417 liquid nitrogen reserve system, the purification system, the calibration source handling system, the
2418 condenser box, the gas circulation pump, and the near detector heat exchange system. The liquid
2419 nitrogen reverse system is basically a liquid nitrogen tank, which is connected to AAr cryogenic
2420 system, to provide its cooling source.

2421 The atmospheric argon cryogenic system serving the cryostat will be installed in LNGS Hall- C
2422 once the cryostat and the DS-20k metallic structure construction will be finalized. A second and
2423 separate cryogenic system to purify and recirculate the depleted Argon filling the TPC detector
2424 inner volume will also be installed on the roof of the warm structure.

2425 18.4. The Radon Free Clean Room

2426 A large radon free clean room close to the main cryostat is needed in order to perform final
2427 assembly and test of the acrylic TPC sealed vessel in a radon free environment. These operations

2428 includes TPC top and bottom acrylic panels bonding with lateral TPC panels, acrylic annealing,
2429 final TPC supporting structure assembly with PDM plates (instrumented with SiPMs) positioned
2430 and fixed on acrylic vessel top and bottom, and cryogenic test of the full inner TPC detector
2431 before insertion in its final position inside the outer veto in the cryostat. In order to perform this
2432 operations, a large test cryostat sufficient to host the full TPC, will be placed in the radon free clean
2433 room. The radon free clean room dimensions are designed to allow the handling and movement of
2434 the TPC vessel parts. Inside the clean room, a crane is foreseen. It will be possible to open the
2435 roof of the clean room for hanging to main Hall C crane the TPC and put it in its final position in
2436 the cryostat. The radon free clean room construction can start once the cryostat warm structure
2437 is completed.

2438 18.5. TPC and Veto Detector Assembly and Installation

2439 Once the radon free clean room will be built and ready to use, TPC final assembly and cryogenic
2440 test in the test cryostat can start. In parallel, once the cryostat inner membrane deposition,
2441 welding and testing is completed, the veto detector acrylic panel assembly and positioning inside
2442 the cryostat will start. A temporary floor inside the cryostat will be put in place to support veto
2443 assembly operations. When the veto detector bottom and lateral walls will be ready to host the
2444 inner detector, the TPC will be put in its final position through the top roof cryostat opening before
2445 the completion and closing of the veto detector top part. Once this is achieved the full veto and
2446 TPC detectors system will be hanged to the cryostat top cap and the false floor and veto supports
2447 removed. Veto and TPC detectors assembly and integration operations inside the cryostat will
2448 require the use of a temporary cleanroom structure on the cryostat roof opening, to allow working
2449 in a radon-free environment.

2450 18.6. DS-20k Proposed Installation Sequence

2451 We provide here below a set of pictures which explain the sequence of main operation steps in the
2452 LNGS Hall C. For each step we describe the key operations impacting Hall C environment during
2453 the DS-20k installation phase.

- 2454 1. Floor preparation: install the survey network, survey the floor planarity, mark the floor for
2455 the imprint of the cryostat, position the shims and the rubber pads.
- 2456 2. Floor structure integration (I): 3 pre-assembled modules will be positioned on dedicated
2457 support structure.
- 2458 3. Floor structure integration (II): additional 5 pre-assembled elements will be positioned and
2459 interconnected. The metal plates will then be welded together, for gas tightness and a He
2460 leak test will be done to qualify the welds.
- 2461 4. Position the floor element: The entire floor quadrant will then be positioned on the prepared
2462 shims, after adding a layer of G10 electrical isolation. At this point a survey of the flatness
2463 will be done and if needed the process will be iterated.
- 2464 5. Second quadrant preparation: Similar activity as in item 2 and 3. This element is the first
2465 wall.
- 2466 6. First wall installation (I) : first the wall structure will be rotated upside down. Stabilizers
2467 will be installed on the cavern wall.
- 2468 7. First wall installation (II) : With main crane the wall will be positioned vertically, bolted to
2469 the floor and bolted to the temporary wall stabilizers. Each of these steps requires detailed
2470 survey work to ensure perpendicularity.
- 2471 8. Second wall integration: same activity as in item 2 and 3.
- 2472 9. Second wall installation: Ration and vertical installation. Stabilizers will be used to secure
2473 the vertical stability after bolting to the floor structure.

- 2474 10. Positioning of the stabilizers on the corners: this is to allow wall 3 and 4 to be positioned
2475 vertically.
- 2476 11. Third wall preparation: Same activity as in item 2 and 3. This time the work is done on the
2477 left to ease the manipulations necessary for the vertical installation.
- 2478 12. Third wall installation: vertical positioning and bolting connection to the floor and to the
2479 stabilizers. Survey activity will follow and correct the process.
- 2480 13. Last wall installation: same process as in item 11 and 12. This time done on the right side.
- 2481 14. Corner elements installation: one by one the four corners pre-assembled will be installed in
2482 place. At this point geometrical corrections will be done with shims, if needed. Once done,
2483 all stabilizers will be removed.
- 2484 15. Preparation of the roof structure: Several preassembled components of the roof will be inter-
2485 connected by bolts and He tested after welding.
- 2486 16. Roof positioning : Then the roof is positioned. The critical step is the rotation upside down
2487 of the roof before positioning it.
- 2488 17. Metallic structure and Cold structure assembly : the metallic structure which will hold the
2489 cryogenics will be installed, with all stairs and egresses. The necessary pipes, which will bring
2490 air for the future radon-free clean room, will be installed on the wall of the cavern. The roof
2491 will be secured with a floor and hand rails to ease access, and a stair system will allow to
2492 enter the interior of the cryostat. The cold insulation and membrane from GTT can start to
2493 be installed. This will be a several months process.
- 2494 18. Detector clean room assembly : on the right side, starting with metallic structures and later
2495 the walls and the doors. This includes the material and personnel SAS.
- 2496 19. Test cryostat : Once the clean room is operational, the test cryostat is positioned and ready
2497 to receive the DS-20k detector parts: the inner TPC and the outer neutron veto acrylic
2498 structures.
- 2499 20. The acrylic TPC vessel arrives to the clean room : ready to be inserted in the test cryostat
2500 once the active TPC elements are inserted. In the mean time on top of the main cryostat a
2501 temporary cleanroom structure is mounted, to allow working in a radon-free environment.
- 2502 21. Ready TPC inserted in the test cryostat : once this is done, the TPC can be tested and
2503 qualified at cold, before insertion in the main cryostat.
- 2504 22. The TPC tested is inserted inside the main cryostat : after the veto counter bottom and
2505 lateral walls are in position and ready to accomodate TPC inside.
- 2506 23. All detector components are inserted and positioned : in particular the veto counter top and
2507 all active probes. All services and cables are routed and the front-end electronics is first
2508 tested in situ
- 2509 24. The cryostat top cap is inserted and the detector is closed, ready for cryogenic commissioning.
- 2510 25. DS-20k is ready for commissioning.

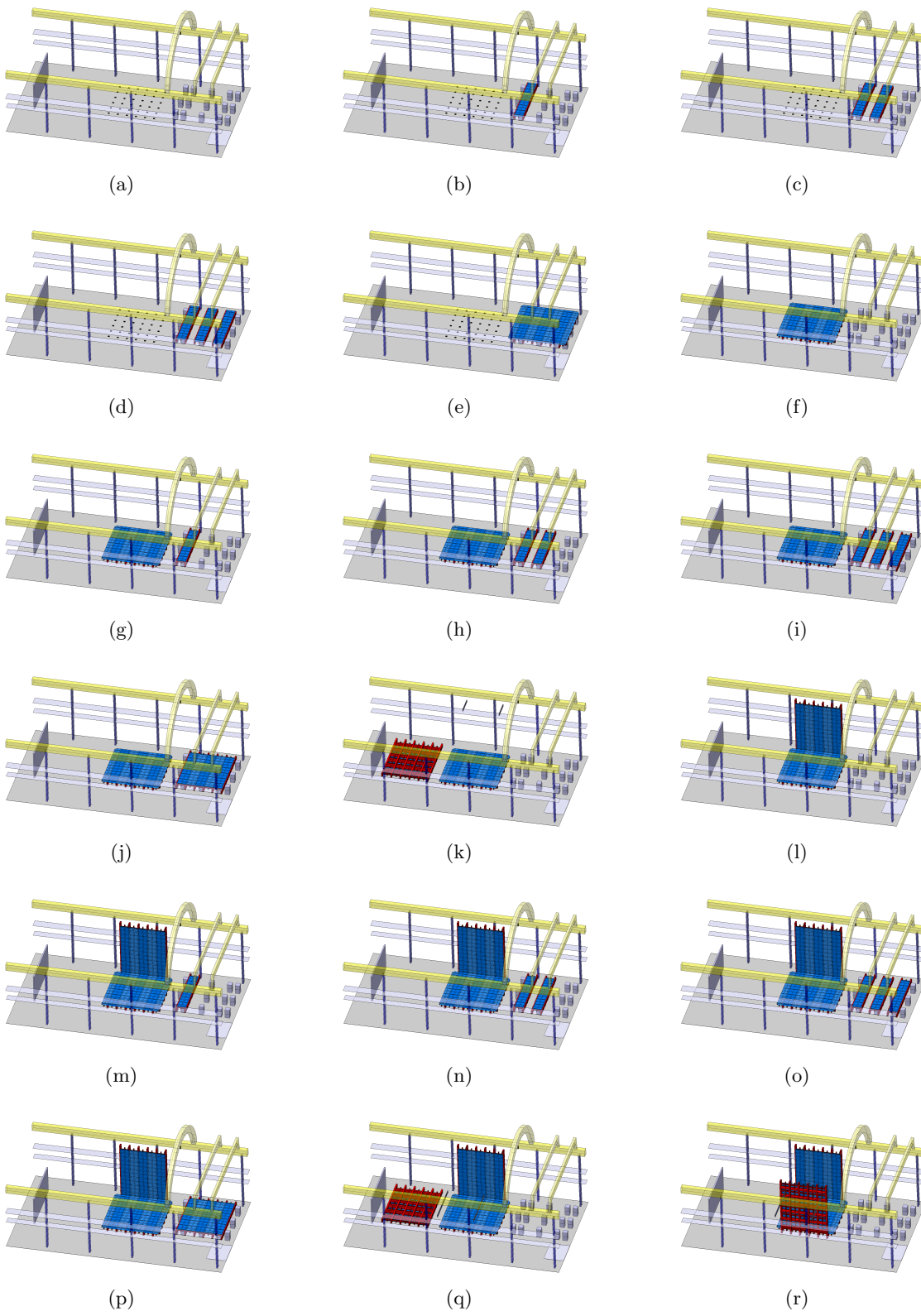


FIG. 38. Details of the installation sequence (I)

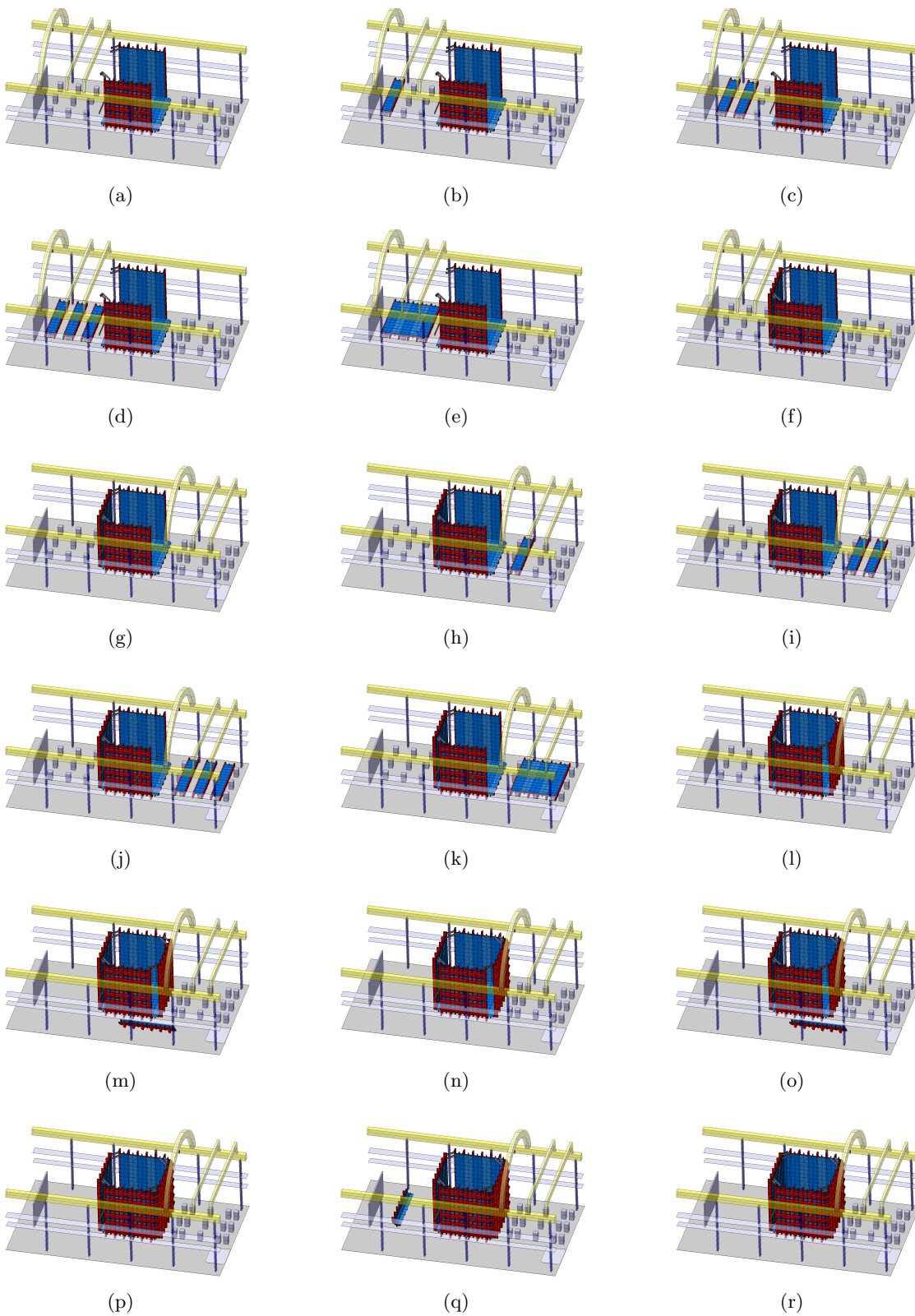


FIG. 39. Details of the installation sequence (II)

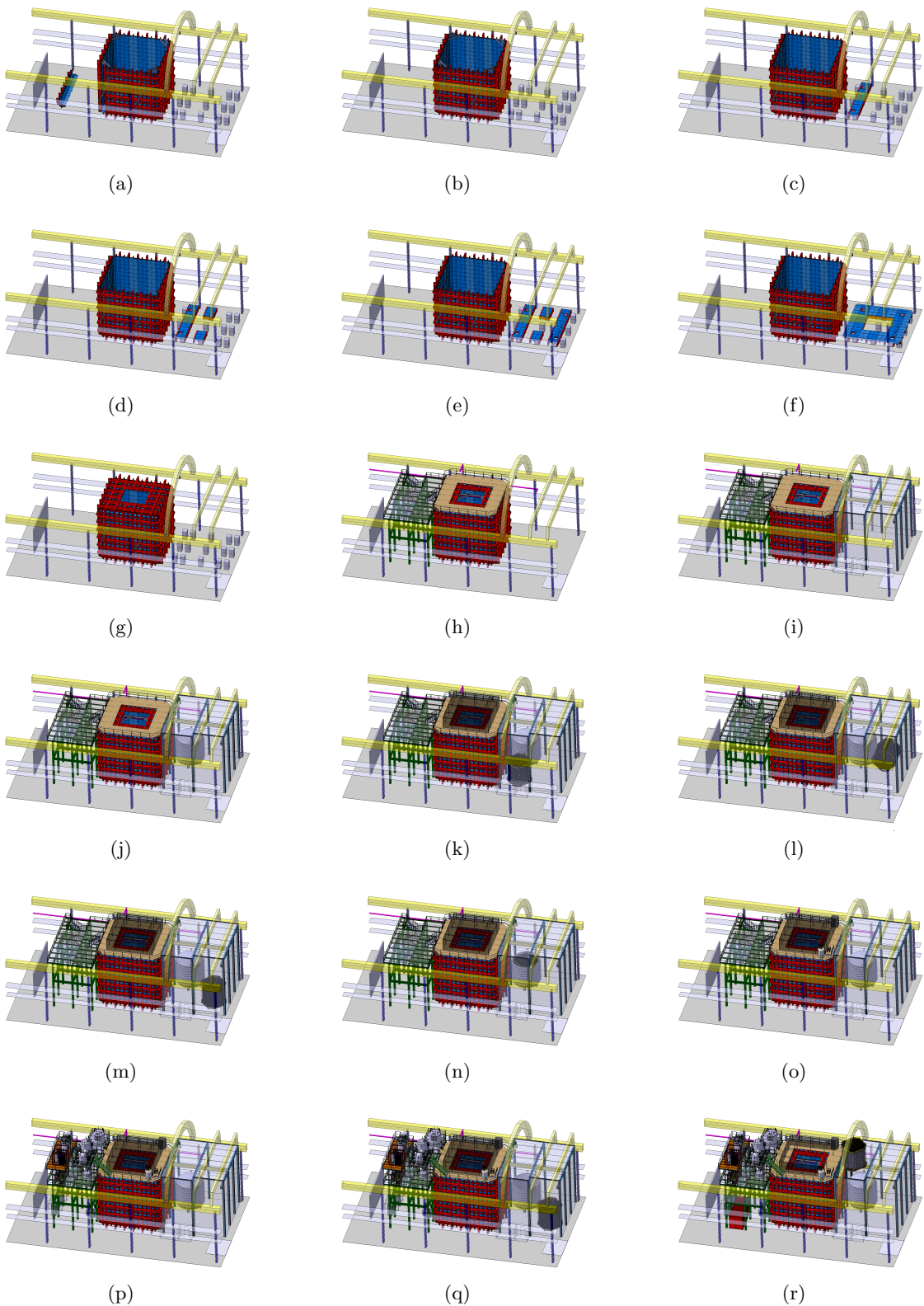


FIG. 40. Details of the installation sequence (III)

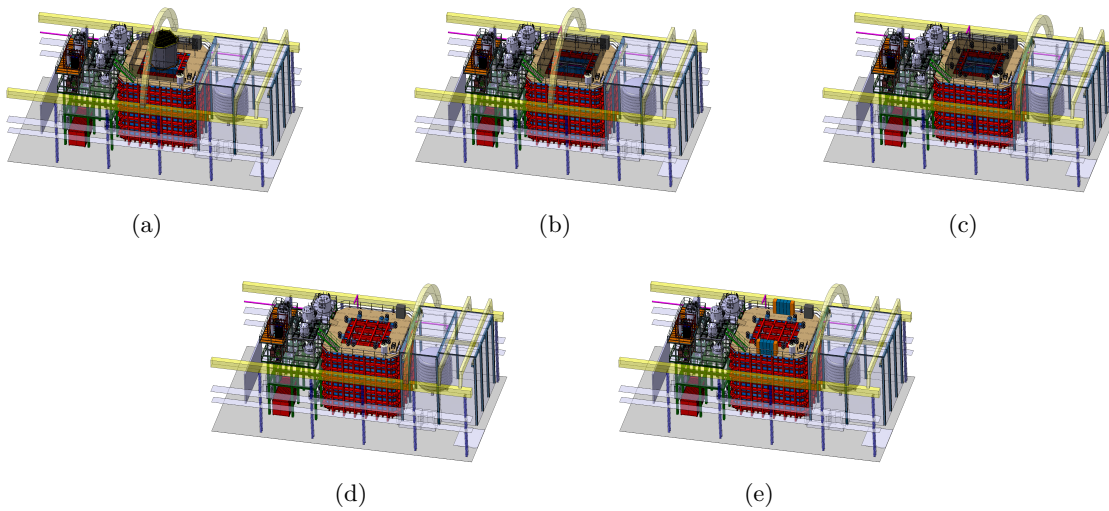


FIG. 41. Details of the installation sequence (IV)

2511 19. HEALTH, SAFETY AND ENVIRONMENTAL ISSUES

2512 **Vengono presentati e discussi i punti specifici riguardanti la salute, sicurezza e am-**
 2513 **biente nella PRA (Quantity Risk Assessment) che include ERA (Environmental Risk**
 2514 **Assessment) e il OHRA (Occupational Health Risk Assessment). Descrivere inoltre:**

- 2515 • **la tipologia e la quantità delle sostanze chimiche che saranno utilizzate nel corso**
 2516 **delle fasi dell'esperimento includendo le modalità' di utilizzo, le schede tecniche**
 2517 **e di sicurezza,**
- 2518 • **la tipologia, la quantità e le modalità di utilizzo dei materiali**
- 2519 • **tipologia e quantità di rifiuti che saranno prodotti nel corso delle fasi dell'esperimento,**
 2520 **al fine di verificare se soddisfano i requisiti di sicurezza e antincendio**

2521 A full PRA analysis is in preparation with the help and support of an external company, and
 2522 will be attached to the TDR when ready.

2523 20. RADIATION PROTECTION ISSUES

2524 **Vengono presentati e discussi i punti specifici che riguardano la radioprotezione**
 2525 **presentando i risultati delle eventuali simulazioni delle radiazioni e la descrizione dei**
 2526 **sistemi di rivelazione e delle schermature. Si richiede di integrare queste considerazioni**
 2527 **con le valutazioni ambientali, operative e di sicurezza già validate e da personale**
 2528 **esperto.**

2529 Detailed simulation results on the shieldings and on the active devices of the DarkSide-20k
 2530 detector and infrastructure layout including calibration system and source storing, will be added
 2531 as soon as they will be available.

2532 Detailed reports and operative procedures will be developed in accordance with the European
 2533 and Italian regulation and LNGS rules in matter of radio protection (D.Lgs. 230/95 and further
 2534 modifications).

2535 21. PROJECT MANAGEMENT

2536 Si richiede di descrivere la strategia di progetto attraverso gli strumenti di Project
2537 Management come per esempio il Project Management Plan e si richiede inoltre di
2538 presentare uno schema riassuntivo sulle tipologie delle gare d'appalto necessarie per
2539 la realizzazione dell'Esperimento (LNGS tender, INFN tender, European tender) in-
2540 cludendo tempi e risorse stimate per il suo espletamento.

2541 In particolare si chiede di esplicitare i seguenti strumenti:

- 2542 • **Fasi del Progetto, Individuazione e descrizione delle principali fasi di un esperimento:**
2543 e.g. APPROVAL – DESIGN - BUILDING – COMMISSIONING – OPERATION & MAINTENANCE
2544 – UPGRADE - DECOMMISSIONING
- 2545 • **Work Breakdown Structure:** Redazione dello schema della WBS e descrizione dei
2546 Work Packages.
- 2547 • **Schedule:**
- 2548 • **Budget:** Elaborazione della tabella dei costi di progettazione, costruzione, instal-
2549 lazione, operazione e smantellamento individuando anche il budget di contingency
2550 e specificando i costi relativi per l'adeguamento impiantistico e strutturale dei
2551 LNGS. Elaborazione di un Cost Breakdown Structure secondo lo schema allegato.
- 2552 • **Risks:** Compilazione della Matrice e del registro dei rischi, secondo lo schema
2553 allegato.
- 2554 • **Organizational Breakdown Structure** Elaborazione dell'Organizzazione del pro-
2555 getto includendo i ruoli e le responsabilità (OBS).

2556 A detailed Project Execution Plan (PEP), prepared for the NSF Mid Scale funding Request
2557 in May 2019 is attached to this document. In that document all the project organization and
2558 management tools are described as well as the current Work Breakdown Structure and gantt chart.
2559 Details on the funding scheme and institution responsibility and cost sharing is also reported there.
2560 We refer to the attached document for all aspect mentioned before. In the following only relevant
2561 additions are reported.

2562 21.1. Update with respect to the attached PEP

- 2563 1. Updated general Gantt chart and relevant discussions.
2564 2. Compilation of the risk register (example below from LNGS template).
2565 3. Costs including operations and dismantling and costs relative to LNGS infrastructure upgrade
2566 and their sources.

-
- 2567 [1] CERN, CERN Yell. Rep. Mon. (2017).
2568 [2] P. A. Amaudruz et al. (The DEAP-3600 Collaboration), Phys. Rev. Lett. **121**, 071801 (2018).
2569 [3] R. Ajaj et al., arXiv:1902.04048v1 (2019).
2570 [4] P. Agnes et al. (The DarkSide Collaboration), Phys. Lett. B **743**, 456 (2015).
2571 [5] P. Agnes et al. (The DarkSide Collaboration), Phys. Rev. D **93**, 081101 (2016).
2572 [6] P. Agnes et al. (The DarkSide Collaboration), Phys. Rev. D **98**, 102006 (2018).
2573 [7] P. Agnes et al. (The DarkSide Collaboration), Phys. Rev. Lett. **121**, 081307 (2018).
2574 [8] P. Agnes et al. (The DarkSide Collaboration), Phys. Rev. Lett. **121**, 111303 (2018).
2575 [9] B. Abi et al. (The DUNE Collaboration), arXiv:1706.07081v2 (2017).
2576 [10] R. Acciarri et al. (The DUNE Collaboration), arXiv:1601.05471v1 (2016).
2577 [11] Heraeus Deutschland GmbH & CO. Kg, *CLEVIOS™ PEDOT* (2019).
2578 [12] G. Angloher et al. (The CRESST Collaboration), Eur. Phys. J. C **72**, 1971 (2012).
2579 [13] D. S. Akerib et al. (The LUX Collaboration), Phys. Rev. Lett. **118**, 021303 (2017).
2580 [14] X. Cui et al. (The PandaX-II Collaboration), Phys. Rev. Lett. **119**, 181302 (2017).
2581 [15] E. Aprile et al. (The XENON Collaboration), Phys. Rev. Lett. **121**, 111302 (2018).

Risk Register

Project name: Common project risks

ID	Date raised	Risk description	Likelihood of the risk occurring	Impact if the risk occurs	Severity Rating based on impact & likelihood.	Owner Person who will manage the risk.	Mitigating action Actions to mitigate the risk e.g. reduce the likelihood.
1	[enter date]	Project purpose and need is not well-defined.	Medium	High	High	Project Sponsor	Complete a business case if not already provided and ensure purpose is well defined on Project Charter and PID.
2	[enter date]	Project design and deliverable definition is incomplete.	Low	High	High	Project Sponsor	Define the scope in detail via design workshops with input from subject matter experts.
3	[enter date]	Project schedule is not clearly defined or understood	Low	Medium	Medium	Project Manager	Hold scheduling workshops with the project team so they understand the plan and likelihood fo missed tasks is reduced.

FIG. 42. Preliminary Risk Registry Table for DarkSide-20kproject(from LNGS teamplate

CBS EXAMPLE

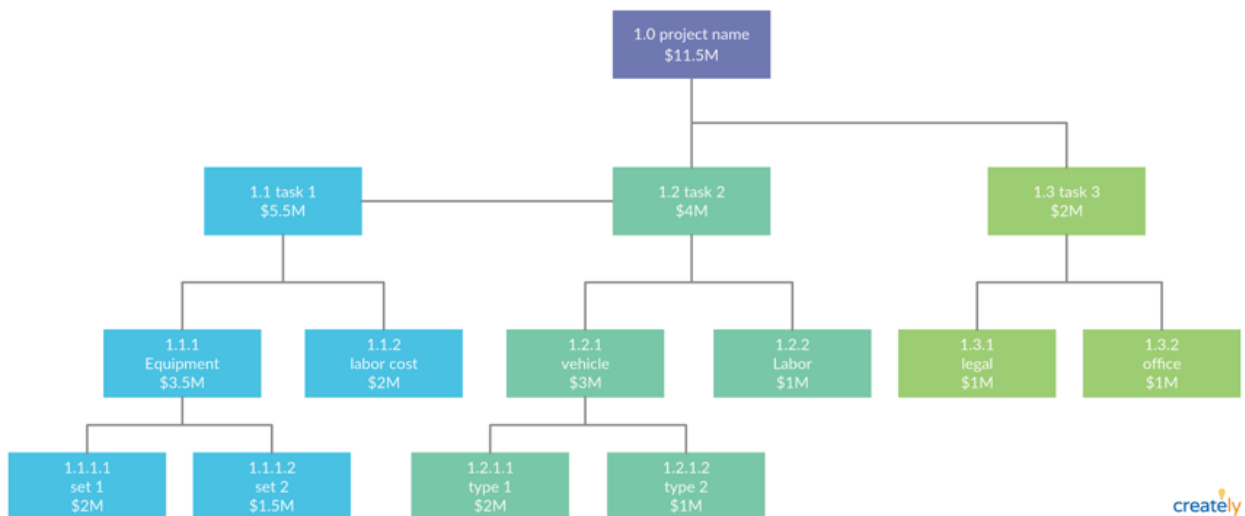


FIG. 43. Cost Breakdown Structure for DarkSide-20kproject (from LNGS teamplate

- 2582 [16] T. A. Collaboration, [CERN Doc. Serv. \(2018\)](#).
 2583 [17] H. Nelson (For The LZ Collaboration), Presentation at DM 2014 (2014).
 2584 [18] V. A. Kudryavtsev (The LZ Collaboration), [AIP Conf. Proc. 1672, 060003 \(2015\)](#).
 2585 [19] E. Aprile (For The XENON Collaboration), Presentation at LNGS Sci. Comm. Apr. 2015 (2015).
 2586 [20] M. G. Boulay (For the DarkSide Collaboration), Presentation at New Ideas DM 2017 (2017).
 2587 [21] R. Agnese et al. (The SuperCDMS Collaboration), [Phys. Rev. D 95, 215 \(2017\)](#).
 2588 [22] J. Billard, E. Figueroa-Feliciano, and L. Strigari, [Phys. Rev. D 89, 023524 \(2014\)](#).
 2589 [23] D. Abercrombie et al., [arXiv:1507.00966v1 \(2015\)](#).

- 2590 [24] C. E. Aalseth et al. (The DarkSide Collaboration), *Eur. Phys. J. Plus* **133**, 131 (2018).
- 2591 [25] M. D'Incecco et al., *IEEE Trans. Nucl. Sci.* **65**, 1005 (2018).
- 2592 [26] M. D'Incecco et al., *IEEE Trans. Nucl. Sci.* **65**, 591 (2018).
- 2593 [27] D. Franco et al., *JCAP* **2016**, 017 (2016).
- 2594 [28] J. Evans et al., *Phys. Rev. D* **95**, 1180 (2017).
- 2595 [29] M. Honda, T. Kajita, K. Kasahara, and S. Midorikawa, *Phys. Rev. D* **83**, 123001 (2011).
- 2596 [30] G. D. Barr, S. Robbins, T. K. Gaisser, and T. Stanev, *Phys. Rev. D* **74**, 323 (2006).
- 2597 [31] R. Tayloe, *JINST* **13**, C04005 (2018).
- 2598 [32] D. Akimov et al. (The COHERENT Collaboration), *Science* **357**, 1123 (2017).
- 2599 [33] H. Cao et al. (The SCENE Collaboration), *Phys. Rev. D* **91**, 092007 (2015).
- 2600 [34] T. Alexander et al. (The SCENE Collaboration), *Phys. Rev. D* **88**, 092006 (2013).
- 2601 [35] P. Agnes et al. (The ARIS Collaboration), *Phys. Rev. D* **97**, 10 (2018).
- 2602 [36] J. Dobson (For the LZ Collaboration), Presentation at DM 2018 (2018).
- 2603 [37] I. Ostrovskiy et al., *IEEE Trans. Nucl. Sci.* **62**, 1825 (2015).
- 2604 [38] S. Cebrián et al. (The NEXT Collaboration), *JINST* **12**, T08003 (2017).
- 2605 [39] J. J. Gómez Cadena, J. M. Benlloch-Rodriguez, and P. Ferrario, *Spectrochim. Acta B* **118**, 6 (2016).
- 2606 [40] S. Cebrián et al., *JINST* **10**, P05006 (2015).
- 2607 [41] M. G. Boulay (For The DEAP Collaboration), *J. Phys. Conf. Ser.* **375**, 012027 (2012).
- 2608 [42] C. M. Nantais, B. T. Cleveland, and M. G. Boulay, *AIP Conf. Proc.* pp. 185–188 (2013).
- 2609 [43] P. Agnes et al. (The DarkSide Collaboration), *JINST* **11**, P12007 (2016).
- 2610 [44] P. Agnes et al. (The DarkSide collaboration), *JINST* **11**, P03016 (2016).
- 2611 [45] P. Agnes (Université Paris Diderot), Ph.D. thesis, Université Paris Diderot (2016), URL <https://tel.archives-ouvertes.fr/tel-01497505v1>.
- 2612 [46] P. Agnes et al. (The DarkSide Collaboration), *JINST* **12**, P12011 (2017).
- 2613 [47] P. Agnes et al. (The DarkSide Collaboration), *JINST* **12**, P01021 (2017).
- 2614 [48] P. Agnes et al. (The DarkSide Collaboration), *JINST* **12**, P10015 (2017).
- 2615 [49] P. Agnes et al. (The DarkSide Collaboration), *JINST* **12**, T12004 (2017).
- 2616 [50] P. Agnes et al. (The DarkSide Collaboration), *Nucl. Inst. Meth. A* **904**, 23 (2018).
- 2617 [51] W. J. Willis and V. Radeka, *Nucl. Inst. Meth.* **120**, 221 (1974).
- 2618 [52] V. Radeka, *IEEE Trans. Nucl. Sci.* **21**, 51 (1974).
- 2619 [53] V. Radeka and S. Rescia, *Nucl. Inst. Meth. A* **265**, 228 (1988).
- 2620 [54] R. L. Chase, C. de La Taille, S. Rescia, and N. Seguin, *Nucl. Inst. Meth. A* **330**, 228 (1993).
- 2621 [55] R. L. Chase and S. Rescia, *IEEE Trans. Nucl. Sci.* **44**, 1028 (1997).
- 2622 [56] W. Ootani, *Nucl. Inst. Meth. A* **732**, 146 (2013).
- 2623 [57] P. W. Cattaneo et al., *Nucl. Inst. Meth. A* **828**, 191 (2016).
- 2624 [58] I. Ostrovskiy (The University of Alabama), (2012).
- 2625 [59] A. S. Barabash et al., *Nucl. Inst. Meth. A* **868**, 98 (2017).
- 2626 [60] L. Mapelli et al., *CERN EDMS* **1837551** (2017).
- 2627 [61] F. A. Lindemann, *Phil. Mag.* **38**, 173 (1919).
- 2628 [62] H. C. Urey, F. G. Brickwedde, and G. M. Murphy, *Phys. Rev.* **40**, 1 (1932).
- 2629 [63] J. de Boer and R. J. Lunbeck, *Physica* **14**, 520 (1948).
- 2630 [64] J. de Boer, *Physica* **14**, 139 (1948).
- 2631 [65] J. de Boer and A. Michels, *Physica* **6**, 97 (1939).
- 2632 [66] J. Bigeleisen, *J. Chem. Phys.* **34**, 1485 (1961).
- 2633 [67] G. Boato, G. Scoles, and M. E. Vallauri, *Nuovo Cim.* **23**, 1041 (1962).
- 2634 [68] G. Boato, G. Casanova, G. Scoles, and M. E. Vallauri, *Nuovo Cim.* **20**, 87 (1961).
- 2635 [69] G. Boato, G. Scoles, and M. E. Vallauri, *Nuovo Cim.* **14**, 735 (1959).
- 2636 [70] G. Casanova, A. Levi, and N. Terzi, *Physica* **30**, 937 (1964).
- 2637 [71] C. Casanova, R. Fieschi, and N. Terzi, *Nuovo Cim.* **18**, 837 (1960).
- 2638 [72] R. Fieschi and N. Terzi, *Physica* **27**, 453 (1961).
- 2639 [73] J. N. Canongia Lopes, A. A. H. Pádua, L. P. N. Rebelo, and J. Bigeleisen, *J. Chem. Phys.* **118**, 5028 (2003).
- 2640 [74] J. C. G. Calado, F. A. Dias, J. N. C. Lopes, and L. P. N. Rebelo, *J. Phys. Chem. B* **104**, 8735 (2000).
- 2641 [75] W. L. McCabe and E. W. Thiele, *Ind. Eng. Chem.* **17**, 605 (1925).
- 2642 [76] A. J. V. Underwood, *Ind. Eng. Chem.* **41**, 2844 (1949).
- 2643 [77] E. R. Gilliland, *Ind. Eng. Chem.* **32**, 1220 (1940).
- 2644 [78] M. R. Fenske, *Ind. Eng. Chem.* **24**, 482 (1932).
- 2645 [79] Aspen Technology, Inc., *Aspen Plus®* (2015).